

Dynamic Surface Tension as a Probe of Irreversible Adsorption of Nanoparticles at Fluid-Fluid Interfaces

by

Navid Bizmark

A thesis
presented to the University of Waterloo
in fulfillment of the
thesis requirement for the degree of
Master of Applied Science
in
Chemical Engineering

Waterloo, Ontario, Canada, 2013

© Navid Bizmark 2013

I hereby declare that I am the sole author of this thesis. This is a true copy of the thesis, including any required final revisions, as accepted by my examiners.

I understand that my thesis may be made electronically available to the public.

Abstract

Adsorption-mediated self-assembly of nanoparticles at fluid interfaces, driven by reduction in interfacial energy, leads to stabilization of emulsions and foams and can be used for the bottom-up fabrication of functional nanostructured materials. Improved understanding of the parameters that control the self-assembly, the structure of nanoparticles at the interface, the barrier properties of the assembly and the rate of particle attachment and exchange is needed if such nanoparticle assemblies are to be employed for the design and fabrication of novel materials and devices. Here, I report on the use of dynamic surface tension (DST) measurements to probe the kinetics of irreversible adsorption and self-assembly of hydrophobic ethyl-cellulose (EC) nanoparticles at the air-water interface. Using thermodynamic arguments, I make a direct connection between the DST and the time-dependent surface coverage. I show that adsorption models appropriate for surfactants (e.g., Ward and Tordai model) break down for irreversible adsorption of nanoparticles, when the adsorption energy far exceeds the mean energy of thermal fluctuations ($k_B T$) and surface blocking effects give rise to a steric barrier to adsorption. I show instead that irreversible adsorption kinetics are unequivocally characterized in terms of the adsorption rate constant and the maximum (jamming) coverage, both of which are determined on the basis of DST data using the generalized random sequential adsorption theory (RSA) for the first time. Novel accurate estimates of the adsorption energy of 42 nm and 89 nm EC nanoparticles are also provided. Coverage of the interface to the jamming limit of 91%, corresponding to a triangular lattice in 2D, is experimentally demonstrated. Colloidal solutions of EC nanoparticles are stabilized at neutral pH by electrostatic repulsive forces. Strong adsorption of these particles at an interface of like charge suggests the parallel action of attractive hydrophobic forces.

Acknowledgements

I would like to express my gratitude to my supervisors professor Marios Ioannidis and professor Dale Henneke for first of all supporting me in all situations and giving me the confidence to deal with the problems and second of all impacting my view to life.

I would also like to thank Dr. Robert Donkers for his help with using the dynamic light scattering instrument, and Dr. Carmen Andrei at the Canadian Centre for Electron Microscopy at McMaster University for providing the required facilities for transmission electron microscopy. The Natural Sciences and Engineering Research Council of Canada (NSERC) is also acknowledged for financial support of this project. I want to thank all of my dear friends at the department of chemical engineering of University of Waterloo, especially Iman and Kaveh, for all their help, support, and valuable hints.

In the end, my special thanks go to my lovely parents and kind sister who always have supported me in ups and downs of this path.

Dedication

To my parents and lovely sister

Table of Contents

List of Tables	viii
List of Figures	ix
1 Introduction	1
1.1 Colloidal Solutions	1
1.1.1 Overview	1
1.1.2 Stability	2
1.1.3 DLVO Theory	3
1.2 Colloidal Particles at Interfaces	6
1.2.1 Adsorption at the Interface	6
1.2.2 Emulsions and Foams	6
1.3 Objectives	10
2 Background	13
2.1 Surface-Active Agents	13
2.1.1 Surfactants and block copolymers	13
2.1.2 Solid particles	16
2.2 Stokes-Einstein Theory of Diffusion	18
2.3 Adsorption Modeling Approaches	20
2.3.1 Reversible adsorption models	21
2.3.2 Irreversible adsorption	34

3	Theoretical Investigations	39
3.1	Adsorption Energy and Surface Tension	39
3.2	Irreversible Adsorption Analysis	42
4	Experimental Methods and Materials	44
4.1	Nanoparticle Synthesis and Characterization	44
4.2	Measurement of Surface Tension	46
5	Results	50
5.1	EC Nanoparticle Characterization	50
5.2	Dynamic Surface Tension (DST) Results	53
6	Discussion	60
6.1	Failure of Reversible Adsorption Model	60
6.2	Adsorption Energy Calculation	65
6.3	Dynamics of Surface Coverage	66
6.4	Adsorption Kinetics	68
7	Conclusions and Recommendations	74
7.1	Conclusions	74
7.2	Recommendations	75
	APPENDICES	77
A	Batch Distillation Calculations	78
B	Late Time and Early Time DST Data Analysis	82
C	Calculating θ_{\max} and K_l	87
D	The Minimum Concentration for Full Coverage	91
	References	93

List of Tables

1.1	Pickering emulsions with various oils stabilized by different solid particles [11].	8
2.1	Different types of adsorption isotherms [17].	25
2.2	Values of parameters in Eq. (2.27) depending on the chosen thermodynamic adsorption isotherm [46].	26
5.1	Fitting parameters of Hua and Rosen’s empirical equation (Eq. (5.1)) at different concentrations of 89.1 nm EC nanoparticle colloidal solutions. . .	58
6.1	Estimates of the diffusion coefficient obtained from early- and long-time DST data via Eq. (2.40) and Eq. (2.37), respectively, for large (89.1 nm) and small (42 nm) EC nanoparticles. Values in brackets are estimates from Eq. (2.7).	62
6.2	Adsorption energy of 89.1 nm EC nanoparticles at the air-water interface. .	66
6.3	Adsorption energy of 42 nm EC nanoparticles at the air-water interface. . .	66
6.4	Calculated dimensionless adsorption constant, \bar{k}_a , and adsorption constant, k_a from Eq. (2.53) and Eq. (2.54), respectively.	70
C.1	The values of the intercept (θ_{\max}) and the slope (K_l) of fitted lines shown in Figure C.1 and Figure C.2 for large and small EC nanoparticles, respectively.	90

List of Figures

1.1	Repulsive forces between two particles (a) electrostatic (b) steric.	3
1.2	Typical trend of interaction potential between two colloidal particles [40]. .	5
1.3	Pickering emulsions (a) schematic [19] (b) conofocal microscope image of water/oil Pickering emulsion, the scale bar is 20 μm [48].	7
1.4	The effect of pH and salinity on foam stabilization [15].	9
1.5	Stabilized foam by 70nm silica nanoparticles [35].	9
1.6	A “foam man” stabilized by ethyl cellulose nanoparticles [41].	10
2.1	Typical shape of amphiphilic molecules: (a) surfactant, (b) block copolymer.	14
2.2	Interfacial activity of amphiphilic molecules below and above the critical micelle concentration (CMC).	14
2.3	The range of surface packing factor and the corresponding self-assembled structure [75].	15
2.4	The variation of different physical properties as a function of surfactant bulk concentration [63].	16
2.5	The arrangement of particles at the oil (or air)-water interface. The top image shows the contact angle of a single solid particle at the interface under different wettability conditions and the bottom image shows how the assembly of particles with different wettability results in O/W or W/O emulsions [14].	17
2.6	The changes in desorption energy of a 20nm fumed silica nanoparticle at different wettabilities [16].	19
2.7	Diffusion of surface-active agents from the bulk and through a subsurface layer to adsorb at the interface.	21

2.8	Schematic energy diagram of CdSe nanoparticle adsorption at the oil-water interface [44]. In this figure, γ is the interfacial tension, d is the particle diameter E is Gibbs free energy, and the subscripts W , O , and P denote <i>water</i> , <i>oil</i> , and <i>particle</i> , respectively. ΔE_1 represents the adsorption energy and ΔE_p is the potential barrier for adsorption.	31
2.9	The adsorption energy of Au-cit nanoparticles with different sizes at OFPA-water interface [26].	32
2.10	The effect of diluting the solution of nanoparticles on the interfacial tension of OFPA-water. Increasing in interfacial tension corresponds to the desorption of the nanoparticles from the interface [26].	33
2.11	The maximum surface coverage for particles with different adsorption energy [38]. Φ represents surface coverage equivalent to θ in this study.	33
2.12	The energy profile (ϕ) of likely charged particle and the interface [7]. ϕ_b and ϕ_m represent the energy barrier (at the distance of δ_b from the interface) and the adsorption energy (at the distance of δ_m from the interface), respectively. n and n_b denote the particle number concentration near the interface and in the bulk, and h_m is the minimum separation distance.	36
3.1	Geometrical patterns for nanoparticles in covering the interface (a) hexagonal close packed (b) square pattern.	41
4.1	Steps of EC nanoparticle synthesis.	44
4.2	The pendant drop tensiometer setup: (1) syringe controller, (2) micro syringe containing the colloidal solution, (3) light source, (4) high-speed CCD camera, and (5) PC.	47
4.3	Fitting Laplace equation on the entire profile of an aqueous droplet containing EC nanoparticles.	48
5.1	EC colloidal solution of ~ 15 g/L (1.5 wt.%) more than 9 months after the synthesis.	50
5.2	(a) DLS and (b) TEM results of large (89.1 nm) EC nanoparticles synthesis. The scale bar is 200 nm.	51
5.3	(a) DLS and (b) TEM results of small (42 nm) EC nanoparticles synthesis. The scale bar is 100 nm.	52

5.4	Dynamic surface tension (DST) of solutions containing (1) no nanoparticle and (2) 89.1 nm EC nanoparticles with concentration of (a) 0.05 g/L, (b) 0.075 g/L, (c) 0.1 g/L, (d) 0.2 g/L, (e) 0.4 g/L, (f) 0.6 g/L, (g) 0.8 g/L, and (h) 1.0 g/L.	54
5.5	Dynamic surface tension (DST) measurements of 89.1 nm EC nanoparticles solutions on a log scale plot at concentrations (1) 0.05 g/L, (2) 0.075 g/L, (3) 0.1 g/L, (4) 0.2 g/L, (5) 0.4 g/L, (6) 0.6 g/L, (7) 0.8 g/L, and (8) 1.0 g/L.	56
5.6	Fitting Hua and Rosen's empirical equation (Eq. (5.1)) on the DST data of colloidal solution of 89.1 nm EC nanoparticles at different concentrations. .	57
5.7	Dynamic surface tension (DST) measurements of 42 nm EC nanoparticles solutions on a (a) linear (b) log scale plot at concentrations (1) 0.1 g/L, (2) 0.2 g/L, (3) 0.4 g/L, (4) 0.6 g/L, (5) 0.8 g/L, and (6) 1.0 g/L.	59
6.1	The effect of steric barrier on a schematic energy profile (ϕ) in the subsurface (along direction h) [1]. ϕ_b and ϕ_s represent the energy barrier (at the distance of δ_b from the interface) and the steric energy barrier, respectively. Also, δ_m and δ denote the primary minimum distance from the interface and the adsorption layer thickness, respectively.	64
6.2	Equilibrium surface tension as a function of the bulk concentration of colloidal solutions of (a) 89.1 nm and (b) 42 nm EC nanoparticles.	67
6.3	Maximum air-water interface coverage by EC nanoparticles at different bulk concentrations: (a) 89.1 nm EC nanoparticles (lines indicate $\theta_{\max} = 0.92 \pm 0.02$) and (b) 42 nm EC nanoparticles (lines indicate $\theta_{\max} = 0.91 \pm 0.003$). The average values for θ_{\max} are obtained from the most concentrated solutions (i.e, the last four concentrations for the large and the last three concentrations for the small EC nanoparticles.	69
6.4	Surface coverage over entire time obtained from numerical modelling characterizing irreversible adsorption with $\theta_{\max} = 0.547$, corresponding to the maximum coverage for solid-fluid interfaces at (1) $\bar{k} = \infty$, (2) $\bar{k} = 1000$, (3) $\bar{k} = 100$, (4) $\bar{k} = 10$, and (5) $\bar{k} = 1$. The dashed lines represent the results of applying Eq. (2.52) and $\tau \equiv t/t_c$ [1].	71
6.5	Surface coverage dynamics (a) $\bar{k}_a \cong 200$ (the case of 89.1 nm EC nanoparticles) (b) $\bar{k}_a \cong 10$ (the case of 42 nm EC nanoparticles). Markers are experimental data for large (a) and small (b) EC nanoparticles, respectively, and lines correspond to Eq. (6.4)	72

A.1	A trial-and-error procedure for calculating the amount of alcohol remaining the final solution.	79
A.2	The vapour-liquid equilibria for a binary mixture of isopropyl alcohol-water plotted in terms of $1/(y-x)$ against the mole fraction of alcohol in the liquid phase.	81
B.1	Fitting Eq. (3.8) on the long time DST data of 89.1 nm EC nanoparticles at (a) 0.05 g/L, (b) 0.075 g/L, (c) 0.1 g/L, (d) 0.2 g/L, (e) 0.4 g/L, (f) 0.6 g/L, (g) 0.8 g/L, and (h) 1.0 g/L bulk concentrations of EC nanoparticles.	83
B.2	Fitting Eq. (3.10) on the early time DST data of 89.1 nm EC nanoparticles at (a) 0.05 g/L, (b) 0.075 g/L, (c) 0.1 g/L, (d) 0.2 g/L, (e) 0.4 g/L, (f) 0.6 g/L, (g) 0.8 g/L, and (h) 1.0 g/L bulk concentrations of EC nanoparticles.	84
B.3	Fitting Eq. (3.8) on the long time DST data of 42 nm EC nanoparticles at (a) 0.1 g/L, (b) 0.2 g/L, (c) 0.4 g/L, (d) 0.6 g/L, (e) 0.8 g/L, and (f) 1.0 g/L bulk concentrations of EC nanoparticles.	85
B.4	Fitting Eq. (3.10) on the early time DST data of 42 nm EC nanoparticles at (a) 0.1 g/L, (b) 0.2 g/L, (c) 0.4 g/L, (d) 0.6 g/L, (e) 0.8 g/L, and (f) 1.0 g/L bulk concentrations of EC nanoparticles.	86
C.1	Fitting Eq. (C.1) to the experimental data of 89.1 nm EC nanoparticle surface coverage at different bulk concentrations: (a) 0.1 g/L, (b) 0.2 g/L, (c) 0.4 g/L, (d) 0.6 g/L, (e) 0.8 g/L, and (f) 1.0 g/L.	88
C.2	Fitting Eq. (C.1) to the experimental data of 42 nm EC nanoparticle surface coverage at different bulk concentrations: (a) 0.1 g/L, (b) 0.2 g/L, (c) 0.4 g/L, (d) 0.6 g/L, (e) 0.8 g/L, and (f) 1.0 g/L.	89

Chapter 1

Introduction

1.1 Colloidal Solutions

1.1.1 Overview

Over 150 years have passed from the date the famous Italian chemist, Francesco Selmi, used the term “pseudosolutions” to introduce the solutions we know today as “colloidal solutions”. Since that date, many efforts have been made to explore different aspects of these solutions in order to provide a better prediction of their behavior. Colloidal solutions refer to liquid solutions containing solid particles and are more common than one may think. Looking at blood, for instance, there are many substances suspended in the liquid making blood a colloidal solution. A great variety of foodstuffs such as milk and sauces, as well as cosmetics, toothpaste, and many drugs are also colloidal solutions. Thomas Graham, who devised the term “colloid” for these types of solutions, defines the solid particle size as being in the range between 1nm to $1\mu\text{m}$. The upper limit comes from the limitation that gravity should have no significant effect on the movement of colloidal particles (i.e., limited sedimentation), whereas the lower limit originates from the concept that colloidal particles must have low diffusion rates [29]. During the past century, colloidal solutions have been widely used in different industries such as pigment and paint, polymer, textile [50], and recently in sol-gel processing [29]. Besides the size, the shape of solid particles is another important parameter controlling the properties of a colloidal solution. These solutions may contain solid particles in spherical, elliptical, planar, rod-shaped or any other shape. Therefore, measuring their size and detecting their shape are essential steps in the characterization of colloidal particles. For micron-sized particles, optical microscopy can

be reliably applied to examine the shape of the particles, whereas transmission electron microscopy (TEM), scanning electron microscopy (SEM), and atomic force microscopy (AFM) are high-tech microscopy methods able to detect the morphology of nanoparticles.

1.1.2 Stability

As a result of attractive forces, particles coagulate (or *flocculate*). Many flocculated bodies combine with each other to form agglomerates. This process reduces an apparently homogeneous solution to a two-phase system containing a settled solid phase and a liquid phase [63]. Thus, the stability of colloidal solutions, controlled by interparticle forces, is of significant concern. The origin of the interparticle forces among colloidal particles is still not completely understood [29]. Molecular- and atomic-level forces, known as strong and weak interactions [40], are common among elementary particles. These forces have a very short range of action ($< 10^{-5}\text{nm}$) – much smaller than the size of nanoparticles. For this reason, they are unlikely to control the interaction among nanoparticles. Long-range forces, on the other hand, are electromagnetic and gravitational forces. As discussed earlier, gravitational forces are not significant for particles with sizes in the colloidal domain. This leaves only forces of electromagnetic nature as the origin of colloidal particle interactions.

All interparticle forces in a colloidal solution can be categorized into two general groups: attractive and repulsive forces. The attractive force is caused van der Waals forces. The van der Waals interaction potentials are proportional to r^{-6} (where r denotes the particle radial distance) [63]. Hence, as the particles move apart from each other, the effect of van der Waals attractive forces rapidly diminishes. The repulsive force, on the contrary, is the result of two fundamentally different types of forces. As shown in Figure 1.1(a), the first type of repulsive force is due to the particle-surface charge. This well-known electrostatic repulsion is investigated in many systems dealing with charged particles or ions. Particularly in colloidal solutions, the charged particles induce a double layer. As the result of the interactions of these double layers around each particle, the colloidal solutions are stabilized. It is shown that the potential energy between two charged particles is in form of a decaying exponential with respect to particle separation distance (see [63]). The other type of repulsive force, which is unique in colloidal solutions, is steric repulsion. This is the case for colloidal particles coated by polymer molecules or surfactants. In a good solvent, the polymer chains expand to reach the maximum of entropy. When two particles, coated by polymer molecules, approach one another, the polymer chains contract (see Figure 1.1 (b)). Owing to compaction of the polymer chains, the entropy is reduced, resulting in a repulsive force called steric repulsion. The polymer chain length for stabilization of the colloidal particles is in the range of 10-1000nm. Therefore, this type of repulsive force is

the dominant interaction in comparison to van der Waals attraction and/or electrostatic repulsion forces [63]. The total interaction potential which is the summation of all the

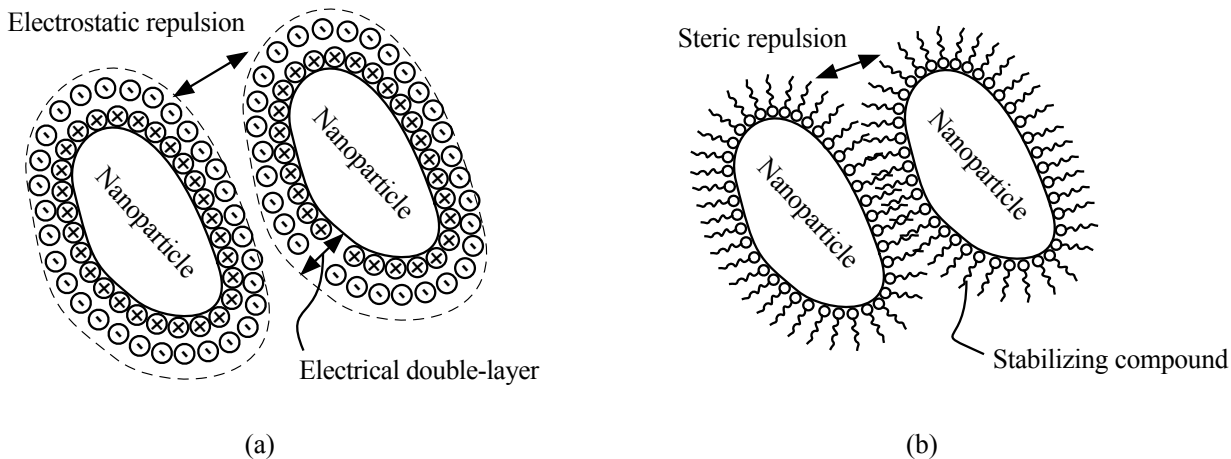


Figure 1.1: Repulsive forces between two particles (a) electrostatic (b) steric.

attractive and repulsive forces dictates the stability of a colloidal solution. One of the most reliable and well-developed theories addressing quantitatively colloidal solution stability is the DLVO theory reviewed in the next section.

1.1.3 DLVO Theory

In order to quantitatively explore the stability of colloidal solutions, two research groups, B.V. Derjaguin and L. Landau in the Soviet Union and E.J.W. Verwey and J.Th.G. Overbeek in the Netherlands, individually developed a theoretical approach. This theory, which is denoted as DLVO theory in honor of the aforementioned scientists, is based on summation of attractive and repulsive forces among the particles, expressed as follows:

$$W_T = W_{att} + W_{rep} \quad (1.1)$$

In solutions that contain similar particles, a common condition for colloidal solutions, the van der Waals forces always operate as attractive forces. The van der Waals attractive energy between two spherical particles of radius r is approximated as [63]:

$$W_{att} = -\frac{H_{121} r}{12 h} \quad (1.2)$$

where h is the separation distance between two colloidal particles, and H_{121} is the Hamaker constant for two particles (noted as phase 1) in the liquid phase (noted as phase 2). The repulsive force in the DLVO theory is caused by the electrostatic interactions resulting in a charged-double layer interactions. Electrostatic repulsion can be caused either by ions sticking onto to the particle surface or by activation of surface charge groups. The DLVO theory was initially developed for charged colloidal particles and was then later extended to the polymer stabilized colloidal solutions [59]. This extension was necessary because for charged particles only the electrostatic forces are dominant, whereas as discussed earlier, for polymer-stabilized particles the steric force is the most significant one. The electrostatic (double layer) repulsion energy is found to be in the general functional form given below [63].

$$W_{rep} = f(\sigma_0, \exp(-C^{0.5}h)) \quad (1.3)$$

where σ_0 denotes the charge per unit area of the particle (surface charge density), and C indicates the electrolyte (salt) concentration in the solution [63]. More details about deriving the repulsive energy are presented in [40, 63]. The most significant parameter in this theory is the separation distance, h . For a colloidal solution, a particular range of separation distance controls the stability of the solution. On one hand, as expressed in Eq. (1.2), the attractive energy varies with the inverse of particle distance. On the other hand, the repulsive energy changes corresponding to an exponential function of separation distance (see Eq. (1.3)). Accordingly, as the particles approach each other, both attractive and repulsive energies increase but at different rates. This implies that the total interaction energy, which is the summation of attractive and repulsive energies, may have local minimum/maximum points. Figure 1.2 plots the total energy (Eq.(1.1)) as well as the attractive (Eq.(1.2)) and repulsive (Eq.(1.3)) energies against the particle separation distance. The primary minimum in this figure represents the “thermodynamic equilibrium state”. In order to reach this condition, particles must overcome the energy barrier. This barrier dictates the stability of a colloidal solution. When this energy barrier is much larger than thermal fluctuations (i.e., $O(k_B T)$), then particles will not flocculate but remain dispersed in the solution resulting in a stable state representing “kinetic stability” [40, 63].

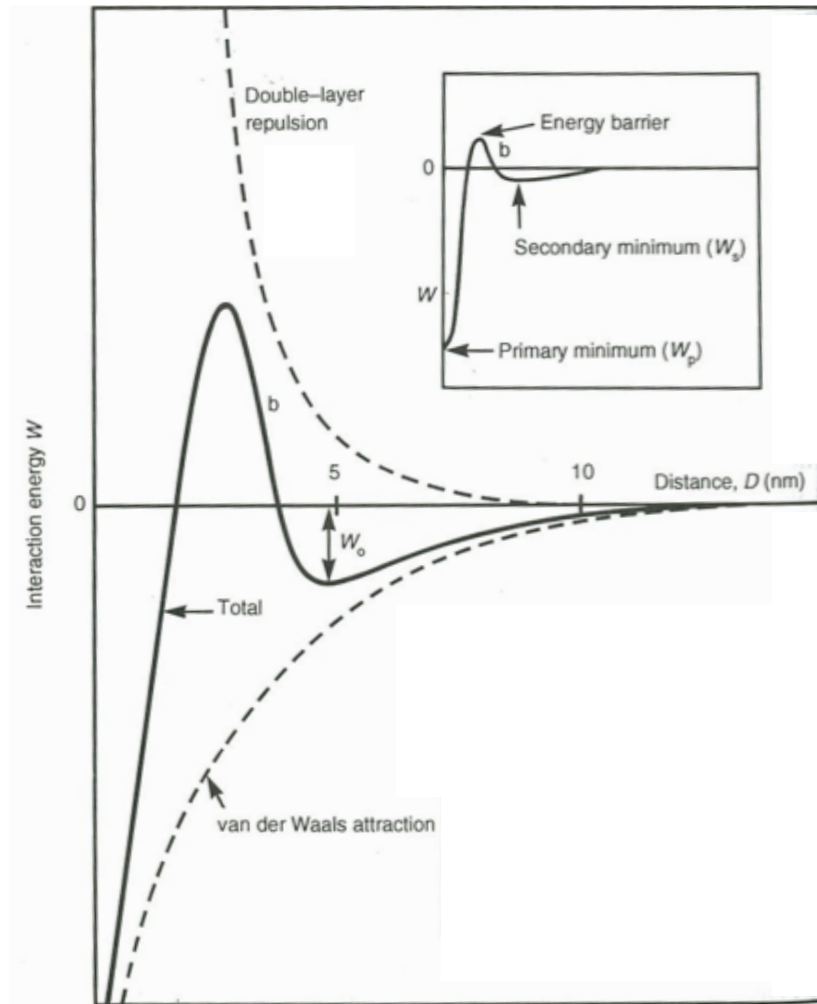


Figure 1.2: Typical trend of interaction potential between two colloidal particles [40].

1.2 Colloidal Particles at Interfaces

1.2.1 Adsorption at the Interface

As discussed earlier, in order to reduce the rate of flocculation, particles are usually stabilized by “dispersants”, which are typically surfactants or block copolymers. Surfactants and most block copolymers are amphiphilic molecules. Thus, regardless of the hydrophobicity/hydrophilicity of the original particles, surfactant-stabilized particles adsorb at the interfaces in order to reach a stable condition. This phenomenon is of great importance in many novel applications. The idea of so-called “bottom-up” fabrication and some enhancements of drug delivery techniques, for example, are based on to the adsorption of nanoparticles at the interfaces. Moreover, this process, which is sometimes referred to as the self-assembly of particles at the interfaces, results in the creation of functional structures [76].

The adsorption of solid particles at interfaces is a dynamic process during which the interfacial properties (i.e., surface or interfacial tension, wettability, and interfacial energy) change significantly. By changing these parameters, the properties of a system can be modified in a desirable way. For instance, due to the reduction in oil reservoir pressure with time, the rate of oil production is reduced. Theoretically, if the interfacial tension of oil-water decreases, capillary forces restraining the movement of oil-water interfaces are overcome and more oil is produced. To reduce the oil-water interfacial tension employing different types of surfactants has been one of the common techniques for many years [10, 33, 37, 61]. Recently, nanoparticles have also been applied. It has been shown that by employing nanoparticles, oil recovery has been increased by $\sim 50\%$ in comparison to the application of surfactants only [64]. The interfacial activity of nanoparticles has made them an alternative to surfactants, particularly in stabilizing emulsions and foams.

1.2.2 Emulsions and Foams

The surface activity of colloidal particles was observed a century ago, when Pickering made stable emulsions using solid particles [53]. The stabilization mechanism is based on the formation of a thin film between two immiscible liquid phases by colloidal particles, preventing the emulsified blobs from coalescence [19]. A schematic and a confocal microscope image of a Pickering emulsion is shown in Figure 1.3 (a) and (b), respectively. The most significant difference between the colloidal-particle and surfactant-stabilized emulsions is the strength of stabilization (i.e., how long the emulsions are stable), which is greater for

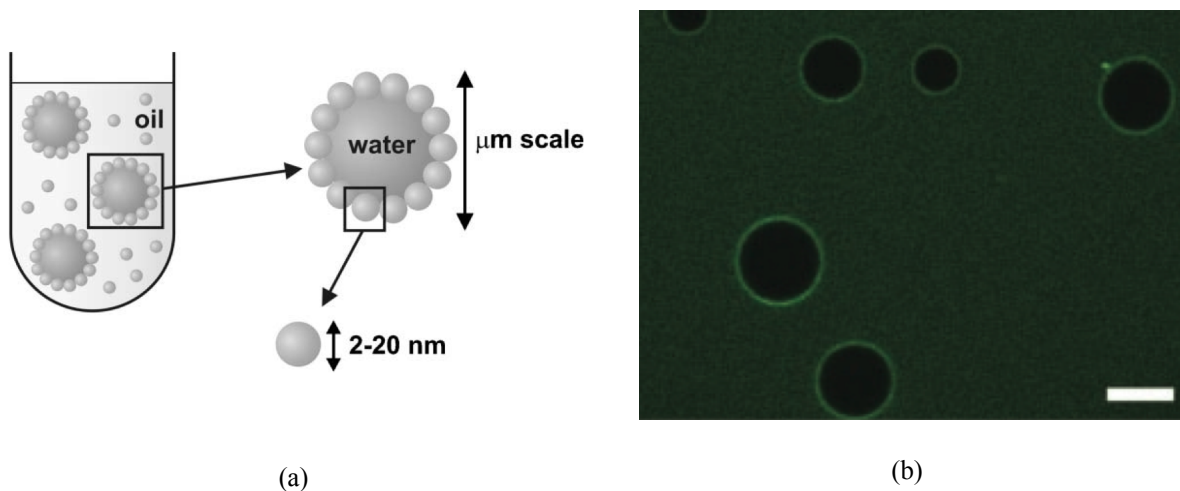


Figure 1.3: Pickering emulsions (a) schematic [19] (b) confocal microscope image of water/oil Pickering emulsion, the scale bar is $20 \mu\text{m}$ [48].

particles. The stability of particle-stabilized emulsions depends on the particle size, with larger colloidal particles producing more stable emulsions [19]. Solid-stabilized emulsions can be formed either in oil/water (O/W) or in water/oil (W/O) depending on the wettability of the particles. If the particles are water-wet, such as silica, then they can stabilize O/W emulsions, and on the contrary, if the particles are oil-wet, such as carbon black, W/O emulsions are stabilized [11]. In Table 1.1, a list of different colloidal particles and their capability in making emulsions with different oils is presented.

Aside from the applications of solid particles for emulsion stabilization, nanoparticle colloidal solutions have been recently employed to make stable foams [35, 41, 22, 62]. Aqueous foams are commonly used in various industries: food, cosmetics, enhanced oil recovery industries, and even in fire extinguishers [35]. There are two main mechanisms causing instability in foams; bubble coalescence and coarsening [22, 62]. Due to gravity and capillarity, the liquid in the film between bubbles drains out resulting in film rupture and eventually bubble coalescence. In the coarsening phenomenon, gas diffuses from small bubbles to large bubbles due to gas pressure difference (Laplace effect), itself due to a difference in the curvature of bubble surfaces [22]. As a result of both mechanisms, bubble size increases with time leading to foam collapse. Studies have confirmed that when solid particles are present at the gas-liquid interface, both bubble coalescence and coarsening are greatly suppressed resulting in stable foam. Highly stable foams have been generated using nanoparticles by paying due consideration to key parameters affecting foam stabil-

Table 1.1: Pickering emulsions with various oils stabilized by different solid particles [11].

Particle type	Oil type	Emulsion type
Barium sulfate	Dodecane	O/W
	Isopropyl myristate	O/W
Calcium carbonate	Dodecane	O/W
	Isopropyl myristate	O/W
Hydrophilic silica	Dodecane	O/W
	Cyclohexane	O/W
	PDMS 50 cS	O/W
	Isopropyl myristate	O/W
Partially hydrophobic silica	Undecanol	O/W
	Dodecane	O/W
	Cyclohexane	O/W
	Isopropyl myristate	W/O
	Undecanol	W/O
Hydrophobic silica	Dodecane	W/O
	Cyclohexane	W/O
	PDMS 50 cS	W/O
	Isopropyl myristate	W/O
	Undecanol	W/O
Polystyrene	Dodecane	W/O
	PDMS 50 cS	W/O
	Isopropyl myristate	W/O
Polytetrafluoroethylene (PTFE)	Dodecane	W/O
	Isopropyl myristate	W/O
	Undecanol	W/O

ity. Salinity, pH, and temperature are the most significant factors. The effects of these parameters are shown in Figure 1.4. For example, increasing the pH can change the hy-

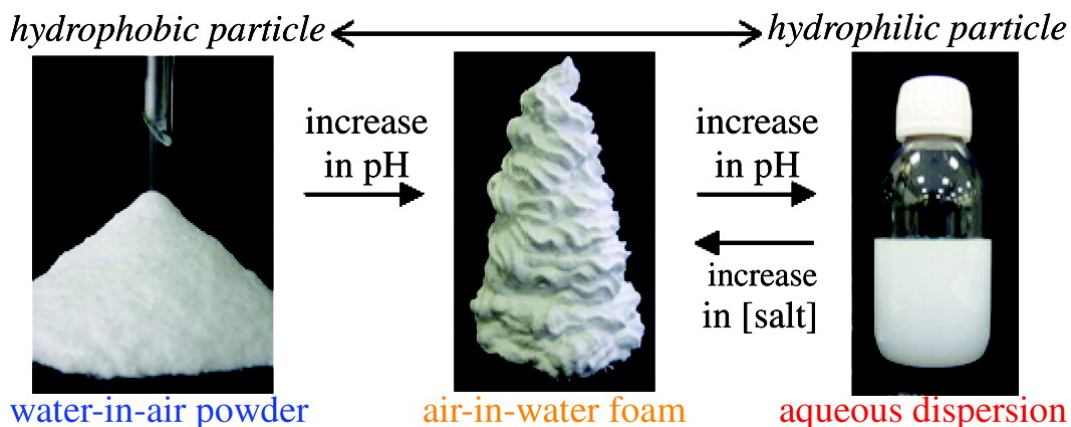


Figure 1.4: The effect of pH and salinity on foam stabilization [15].

drophobicity of a particular material (silica in this case) rendering it more hydrophilic. On the other hand, increasing the salinity of a colloidal solution containing hydrophilic nanoparticles can lead to the production of a particle-stabilized foam. Similar to emulsions, the wettability of the solid particles is the most important parameter controlling this transitional behavior. Accordingly, many concepts developed for Pickering emulsions can be applied to solid-stabilized foams as well.

Figure 1.5 and 1.6 show two types of nanoparticle-stabilized foams. In Figure 1.5, hierarchical features of 70 nm silica nanoparticle stabilized foam are shown. This type

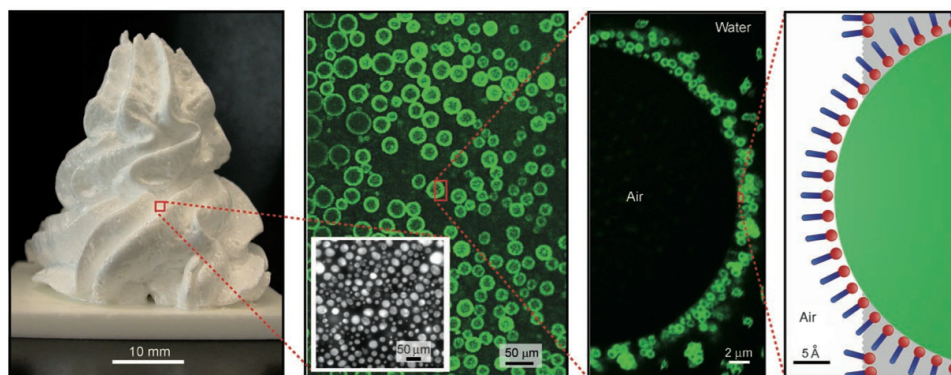


Figure 1.5: Stabilized foam by 70nm silica nanoparticles [35].

of foam was stable for four days with no sign of liquid drainage, creaming, or bubble disproportionation [35]. As reported in that study, such super-stable foams containing bubbles in a range of 10-100 μm in diameter, could find application in cosmetic and food processing. The fabrication of porous materials is also possible employing these particle-stabilized foams.

In another research study [41], a 10cm tall "never-melting" snowman shown in Figure 1.6 is made by creamed foam stabilized by ethyl cellulose (EC) nanoparticles. EC is a



Figure 1.6: A "foam man" stabilized by ethyl cellulose nanoparticles [41].

highly hydrophobic material that is completely insoluble in water. The EC nanoparticles can make a super stable frame structure to be templated for many purposes. In this particular case, the EC foam was stable for three days and after the drainage of the film the dry foam was used to make the snowman.

1.3 Objectives

Ethyl cellulose (EC) nanoparticles are a very interesting material for their remarkable ability to stabilize aqueous foams [41]. They are easy to synthesize and do not require the

addition of the capping agents in order to form a stable colloidal solution. This research interrogates the dynamics of EC nanoparticle adsorption at the gas-liquid interface using a surface tension probe. In doing so, this research calls into question the appropriateness of adsorption models previously used with success to describe the dynamic surface tension (DST) data of aqueous surfactant solutions. Such models were recently extended to colloidal solutions of small (< 10 nm) nanoparticles despite some key differences between surfactants and nanoparticle solutions:

- Surfactant molecules dissolve into the solvent, whereas nanoparticles are suspended in the solvent (making a colloidal solution).
- Surfactant molecules are amphiphilic. Amphiphilic molecules make particular structures such as micelle, vesicle, etc., depending on their molecular configuration, whereas surface-active nanoparticles cannot do so.
- Finally, phenomena such as flocculation or aggregation, which affect the interfacial activity of nanoparticles, are not present in surfactant solutions.

A key hypothesis in this research is that the extension of surfactant adsorption models to nanoparticles is valid only when the process is reversible, that is when the energy of adsorption is of the order of thermal fluctuations ($\sim k_B T$). According to this hypothesis, reversible adsorption models should break down for larger nanoparticle adsorption at fluid-fluid interfaces, which is associated with a large energy release and is thus irreversible.

In this context, this project aims to develop a practical methodology for quantifying the interfacial behavior of nanoparticles at fluid-fluid interfaces. The expected outcome is an experimentally validated model of irreversible adsorption of nanoparticles at fluid-fluid interfaces. Key research milestones are listed below:

- Synthesis of EC nanoparticles with different sizes employing an anti-solvent synthesis method. Investigating the adsorption of nanoparticles with different sizes is essential in validating the developed model.
- Assessment of nanoparticle adsorption at the gas-liquid interface via measurement of dynamic surface tension using an axisymmetric pendant drop method: establishing the connection between DST and adsorption of nanoparticles at the interface.
- Developing a dynamic model for exploring the irreversible adsorption of nanoparticles at fluid-fluid interfaces.

- Analyzing the DST data of EC nanoparticles of different size using the developed model and comparing its performance to existing models.

Chapter 2

Background

2.1 Surface-Active Agents

2.1.1 Surfactants and block copolymers

The term amphiphilicity refers to the tendency of one part of a molecule to associate with an aqueous phase when another part prefers a non-aqueous phase. Surfactants are well known amphiphilic molecules with a structure schematically shown in Figure 2.1 (a). Another type of amphiphilic materials that has attracted much attention are block copolymers. As can be inferred from the name, block copolymers contain different polymeric chains in their molecular structure. Alternating hydrophilic and hydrophobic chains impart an amphiphilic nature to the molecule. Di-block copolymers are the most common type of these materials, as shown in Figure 2.1 (b). From another point of view, block copolymers are a kind of “macromolecular surfactants” [75]. Consequently, discussion regarding surfactants is applicable to block copolymers as well.

In an aqueous phase, the hydrophobic section of the amphiphilic molecule is unstable causing unfavorable interactions. To reduce these interactions, surfactant molecules tend to “self-assemble” at an air-water or oil-water interface, resulting in a monolayer of adsorbed surfactant molecules at the interface, as shown in Figure 2.2. By increasing the concentration of surfactant molecules in the solution, the fluid-fluid interface becomes increasingly covered by the surfactant molecules. If the bulk concentration is further increased, a second type of interactions take place: surfactant molecules organize themselves into micelles, vesicles, and other forms depending on their geometrical shape. In order to

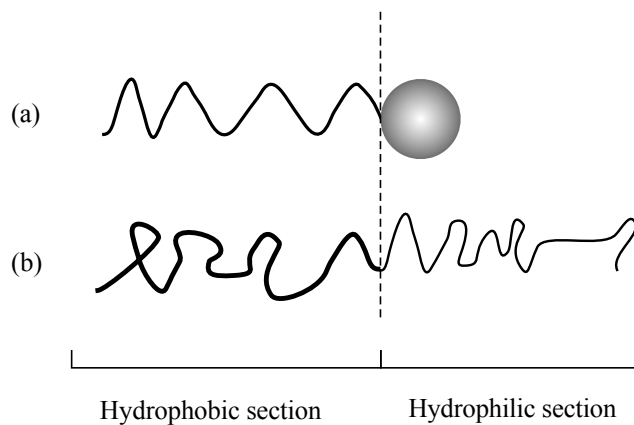


Figure 2.1: Typical shape of amphiphilic molecules: (a) surfactant, (b) block copolymer.

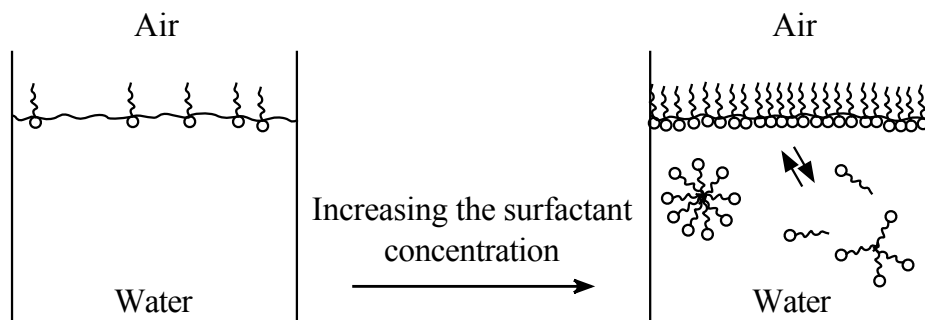


Figure 2.2: Interfacial activity of amphiphilic molecules below and above the critical micelle concentration (CMC).

predict the self-assembled shapes, a unitless parameter, known as the surfactant packing factor, is defined [75].

$$P = \frac{v}{a_0 l} \quad (2.1)$$

where v and l are the volume and the length of hydrophobic section, respectively, and a_0 is the optimal surface area occupied by one surfactant molecule at the interface. The relationship between the surfactant packing factor, P , and the corresponding self-assembled structure is shown in Figure 2.3.

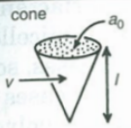
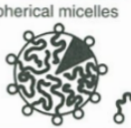




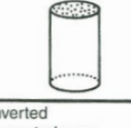
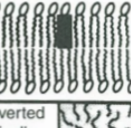


P	Surfactant Shape	Self-Assembly Shape
$<1/3$	cone 	Spherical micelles 
$1/3-1/2$	Truncated cone 	Cylindrical micelles 
$1/2-1$	Truncated cone 	Flexible bilayers, vesicles 
-1	Cylinder 	Planar bilayers 
>1	Inverted truncated cone or wedge 	Inverted micelles 

Figure 2.3: The range of surface packing factor and the corresponding self-assembled structure [75].

The bulk concentration at which the self-assembled structures begin to predominate is known as the *critical micelle concentration* (CMC). The formation of self-assembled structures causes a significant change in many of the physical properties of the solution. Figure 2.4 shows a typical surfactant solution (sodium dodecyl sulfate or SDS). Turbidity, for instance, is constant below the CMC because the dissolved surfactant monomers are too small to scatter visible light. Beyond the CMC, however, the equilibrium between surfactant monomers and micelles is shifted heavily towards the much larger micelles. As a result, turbidity increases with increasing surfactant bulk concentration. Increasing adsorption (self-assembly) of surfactant monomers at a fluid-fluid interface with increasing surfactant bulk concentration results in reduction of the surface/interfacial tension. Increasing the surfactant concentration beyond the CMC does not lead to further reduction, as the additional surfactant monomers organize themselves in the form of micelles rather than adsorbed monomers. The vertical dashed line, in Figure 2.4, represents the CMC.

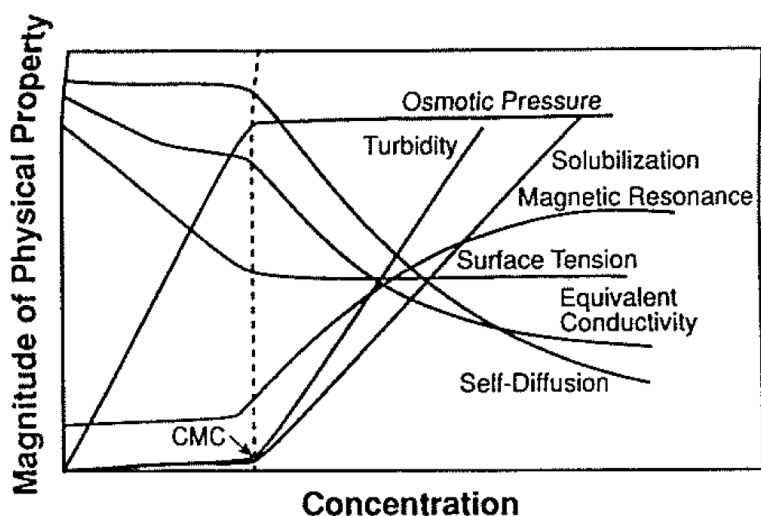


Figure 2.4: The variation of different physical properties as a function of surfactant bulk concentration [63].

2.1.2 Solid particles

Micron-sized solid particles were introduced as a surface-active agent in the last century when so-called Pickering emulsions were successfully stabilized by iron oxide, silicon diox-

ide, kaolin, and barium sulfate colloidal particles [19]. Nanoparticles have also been employed recently to stabilize foams [41, 62, 35]. The interfacial activity of nanoparticles is significant not only in the field of foam and emulsion stabilization, but also because it opens novel routes for the fabrication of nanoporous membranes, functional nanomaterials, capsules, and other “smart” materials [32, 38].

As discussed in section 1.2.2, depending on the wettability of solid particles, O/W or W/O emulsions can be stabilized by solid particles. The wettability of solid particles can be deduced from the value of the contact angle of a single particle at the interface, as shown in Figure 2.5. According to this figure, if the contact angle is below 90° , the

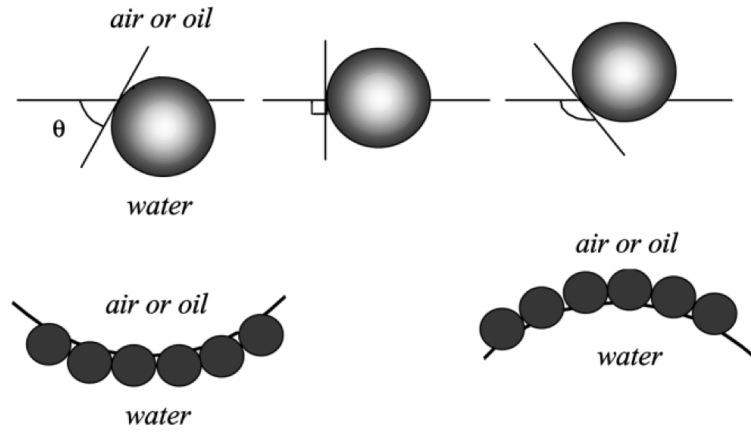


Figure 2.5: The arrangement of particles at the oil (or air)-water interface. The top image shows the contact angle of a single solid particle at the interface under different wettability conditions and the bottom image shows how the assembly of particles with different wettability results in O/W or W/O emulsions [14].

particle is considered to be water-wet, whereas it is oil-wet if the contact angle is larger than 90° . In order to quantitatively explore the presence of solid particles at the interface, Pieranski [54] conducted a fundamental investigation of the adsorption of 245 nm spherical polystyrene particles at the air-water interface. In a two-dimensional geometry, three interfacial energies are defined: energy of particle-air (P-A), particle-water (P-W), and water-air (W-A) interfaces. The adsorption energy is found to be [19, 54]:

$$\Delta E = -\frac{\pi r^2}{\gamma_{W/A}} [\gamma_{W/A} - (\gamma_{P/W} - \gamma_{P/A})]^2 \quad (2.2)$$

where r denotes the particle radius. Applying Young’s equation ($\gamma_{P-A} = \gamma_{P-W} + \gamma_{W-A} \cos\theta$),

the adsorption energy (Eq. (2.2)) can be expressed as [71]

$$\Delta E = -\gamma_{W-A}\pi r^2(1 \pm \cos\theta)^2 \quad (2.3)$$

where γ_{W-A} denotes the water-air interfacial tension. In Eq. (2.3), the positive or negative sign of the term within parentheses applies depending on whether $\theta > 90^\circ$ or $\theta < 90^\circ$, respectively, where θ is measured through the aqueous phase. Adsorption of particles always results in reduction of interfacial energy, hence $\Delta E < 0$.

Eq. (2.3) shows that the adsorption energy is proportional to the square of the particle radius. Consequently, the adsorption energy of micro particles (particles with a diameter of $>1\mu m$) is of the order of thousands of $k_B T$, whereas small nanoparticles ($<5nm$) have adsorption energy of just a few $k_B T$, which is comparable to the adsorption energy of surfactant molecules and to thermal fluctuations [54, 26, 14]. As the size of adsorbed particles increases, particle-stabilized emulsions or foams become more stable [14]. The effect of contact angle (wettability) on the assembly of nanoparticles was considered by Binks and Lumsdon [16]. For the desorption of a 20nm fumed silica nanoparticle from the water-toluene interface at $22^\circ C$ when the interfacial tension of water-toluene is 36 mN/m [16], they obtained the results depicted in Figure 2.6. As expected, the maximum desorption energy (i.e., $\sim 2700k_B T$), corresponds to $\theta = 90^\circ$ indicating the most stable condition. If the fumed silica nanoparticle considered in that study had been 100 nm in diameter, then the maximum desorption energy (i.e., at $\theta = 90^\circ$) would be 25 times larger than that of for a 20 nm particle. Similarly, for a particle with diameter of 5 nm, the adsorption energy would be one sixteenth of the energy for a 20 nm particle.

2.2 Stokes-Einstein Theory of Diffusion

Adsorption of any dissolved species (surfactant or block copolymer molecules) or suspended species (micro or nanoparticles) at a fluid-fluid interface is preceded by transport of that species from the bulk phase to the interface. In the simplest scenario, applicable to tensiometry, convection is negligible and transport is by diffusion of the adsorbing species within a liquid phase. Starting from the Nernst-Einstein equation, the diffusivity of a single particle (A) in the liquid (B) can be expressed as follows [18]

$$D_{AB} = k_B T \frac{u_A}{F_A} \quad (2.4)$$

where D_{AB} denotes the diffusion coefficient, k_B is the Boltzmann constant, and T is the temperature. u_A/F_A represents the mobility of particle A in the liquid B. This mobility

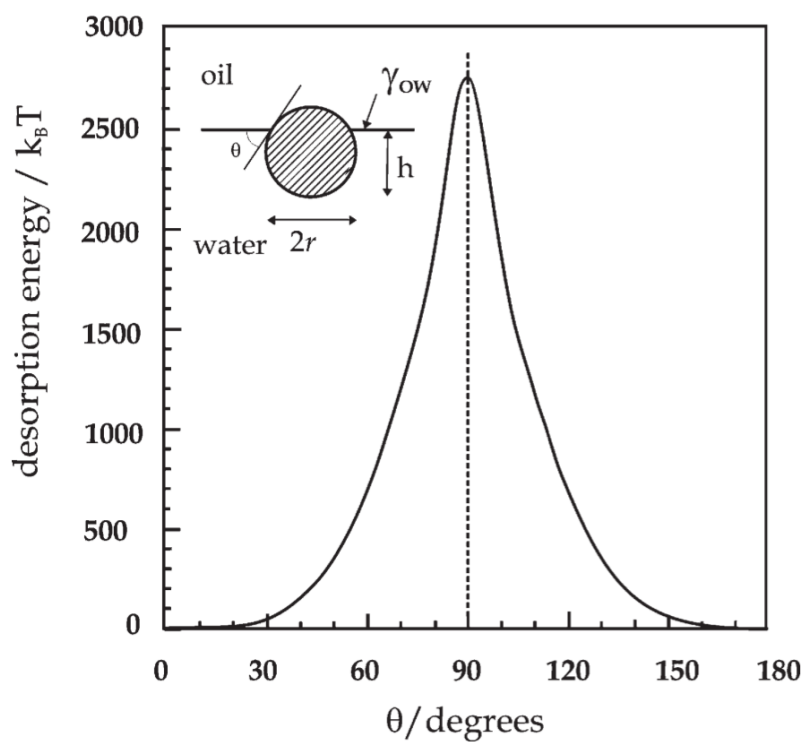


Figure 2.6: The changes in desorption energy of a 20nm fumed silica nanoparticle at different wettabilities [16].

is attained at steady-state conditions, where the particle A executes Brownian motion as the result of force F_A . In the context of continuum hydrodynamics, the Brownian force is equal to the total drag force on the particle:

$$F_A = 6\pi\mu_B u_A R_A \left(\frac{2\mu_B + R_A\beta_{AB}}{3\mu_B + R_A\beta_{AB}} \right) \quad (2.5)$$

where μ_B and R_A are the fluid viscosity and particle radius, respectively, and β_{AB} represents the coefficient of sliding friction [18]. In one extreme, the no-slip condition is valid (i.e., $\beta_{AB} \rightarrow \infty$) and Eq. (2.5) reduces to Stokes' law:

$$F_A = 6\pi\mu_B u_A R_A \quad (2.6)$$

Substituting the above equation into the Nernst-Einstein equation (Eq. (2.4) results in

$$D_{AB} = \frac{k_B T}{6\pi\mu_B R_A} \quad (2.7)$$

Eq. (2.7) is known as the Stokes-Einstein equation and gives a good description of the diffusivity of large (relative to the size of solvent molecules) spherical particles or molecules through a liquid phase continuum. The other extreme is when the fluid does not tend to stick on the solid surface (complete slip condition), corresponding to a zero value for the coefficient of sliding friction ($\beta_{AB} = 0$). In this case, the diffusion coefficient can be obtained from Eq. (2.4) as

$$D_{AB} = \frac{k_B T}{4\pi\mu_B R_A} \quad (2.8)$$

Eq. (2.7) or Eq. (2.8) can be used to estimate the diffusion coefficient of dilute solutions of nanoparticles with good accuracy from knowledge of particle radius and solvent viscosity.

2.3 Adsorption Modeling Approaches

The energy associated with the attachment of a single particle is key to the description of the adsorption process, in the sense that the reversibility or irreversibility of the process depends on the magnitude of the adsorption energy. A small adsorption energy, on the order of a few $k_B T$, results in a reversible process, since it can be supplied by thermal fluctuation. On the other hand, the process is effectively irreversible if desorption is extremely unlikely, which is the case if the adsorption energy greatly exceeds the energy that can be supplied by thermal fluctuations. As discussed earlier, the magnitude of the adsorption energy depends

on the type and size of surface-active agents. For surfactants and block copolymers, it is on the order of thermal fluctuations ($\sim k_B T$). However, as shown in Eq. (2.2), the adsorption energy for solid particles varies with the square of particle radius. Thus, we should expect a transition from a reversible adsorption process for very small particles ($< 5\text{nm}$) to an irreversible one for larger particles ($> 20\text{nm}$). This is a key hypothesis of this study. In what follows, the theories and models addressing reversible and irreversible adsorption are reviewed.

2.3.1 Reversible adsorption models

Mixed diffusion-kinetic control model

The dynamics of the adsorption of surface-active agents at a fluid-fluid interface is thought to be controlled by two processes in series. Consider a thin layer of thickness d (the so-called “subsurface”) just below the interface, as shown in Figure 2.7. The two processes of interest are:

1. Ordinary (Fickian) diffusion of the species from the bulk of the solution to the subsurface
2. Transport of the surface-active species from the subsurface to the fluid-fluid interface (adsorption)

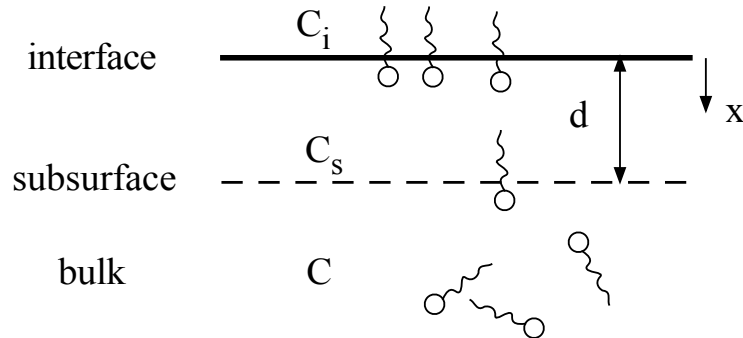


Figure 2.7: Diffusion of surface-active agents from the bulk and through a subsurface layer to adsorb at the interface.

The thickness (d) of the subsurface layer is of the order of a few mean free paths of the adsorbing species [46].

Assuming one-dimensional transport, the ordinary diffusion of a surface active species in the domain $d < x < \infty$ is described by:

$$\frac{\partial C}{\partial t} = D \frac{\partial^2 C}{\partial x^2} \quad (2.9)$$

where D denotes the diffusion coefficient, which is assumed to be constant (see Eq. (2.7)) an assumption that is fully justified for dilute systems. Eq. (2.9) is subject to the following boundary and initial conditions

$$C(d, t) = C_s(t) \quad (2.10)$$

$$C(\infty, t) = C_0 \quad (2.11)$$

$$C(x, 0) = C_0 \quad (2.12)$$

The dynamics of transfer of surface-active species from the subsurface to the interface is described by the following *kinetic* equation [46]:

$$\frac{d\Gamma}{dt} = k_a g(\Gamma) C_s - k_d f(\Gamma) \quad (2.13)$$

which expresses the fact that the rate of accumulation of species at the interface is equal to the difference between the rates of adsorption and desorption. Γ is the surface concentration of the adsorbed species and k_a and k_d are the adsorption and desorption rate constants, respectively. In writing Eq. (2.13), one assumes that the rate of adsorption depends on both surface (Γ) and subsurface (C_s) concentrations, whereas the rate of desorption depends only on the surface concentration (Γ). The adsorption rate is assumed to depend linearly on bulk concentration (C_s), whereas Γ is thought to affect both adsorption and desorption rates in a possibly more complex fashion, accounted for via the functions $g(\Gamma)$ and $f(\Gamma)$ for the adsorption and desorption rates, respectively.

Rearranging Eq. (2.13) we obtain

$$\frac{d\Gamma}{dt} = k_a g(\Gamma) \left(C_s - \frac{k_d f(\Gamma)}{k_a g(\Gamma)} \right) \quad (2.14)$$

The ratio obtained in the right-hand side of Eq. (2.14) has units of concentration and is defined as C_i [46]:

$$C_i \equiv \frac{k_d f(\Gamma)}{k_a g(\Gamma)} \quad (2.15)$$

C_i allows Eq. (2.13) to be expressed as[46]:

$$\frac{d\Gamma}{dt} = k_a g(\Gamma)(C_s - C_i) \quad (2.16)$$

The advantage of rewriting Eq. (2.13) as Eq. (2.16) is that the species conservation statement for the interface is now given in terms of an apparent concentration difference (see Figure 2.7).

The adsorption rate constant may be expressed in the form of an Arrhenius-type relation as follows [46]:

$$k_a = \frac{\bar{v}}{4} \exp\left(-\frac{\Delta E}{k_B T}\right) \quad (2.17)$$

in which, \bar{v} is the mean velocity of the adsorbing species, k_B is the Boltzmann constant and T is the temperature. ΔE is the adsorption energy barrier (or in some references [46] *activation energy*). Considering that $D = \bar{v}d/4$ [46] and substituting Eq. (2.17) into Eq. (2.16) one obtains:

$$\frac{d\Gamma}{dt} = D \exp\left(-\frac{\Delta E}{k_B T}\right) g(\Gamma) \left(\frac{C_s - C_i}{d}\right) \quad (2.18)$$

It is convenient to define D^* [46]:

$$D^* \equiv D \exp\left(-\frac{\Delta E}{k_B T}\right) \quad (2.19)$$

such that Eq. (2.18) may be written as:

$$\frac{d\Gamma}{dt} = D^* g(\Gamma) \left(\frac{C_s - C_i}{d}\right) \quad (2.20)$$

Taking the limit of Eq. (2.20) as $d \rightarrow 0$ results in the following general equation for describing the dynamics of surface-active species transferring from the subsurface to the interface [46].

$$\frac{\partial \Gamma}{\partial t} = g(\Gamma) D^* \frac{\partial C}{\partial x} \Big|_{x \rightarrow 0^+} \quad (2.21)$$

One can identify the right-hand side of Eq. (2.21) with a diffusion flux driven by the concentration gradient $(\partial C / \partial x)|_{x \rightarrow 0^+}$ and proportional to a diffusion coefficient equal to $g(\Gamma) D^*$. For $g(\Gamma) \neq 1$ and $\Delta E \neq 0$, this is akin to a discontinuity in the diffusion coefficient, which is equal to D in $d < x < \infty$ and equal to $g(\Gamma) D^*$ in $0 < x < d$ (the subsurface).

In other words, the adsorption of surfactant molecules is mathematically described as two diffusion steps: ordinary diffusion from the bulk phase to the subsurface and “diffusion” through the subsurface to the interface with a different (lower) diffusion coefficient. Liggieri *et al.* [46] therein have shown that the domain of diffusion can be extended from $d < x < \infty$ to $0 < x < \infty$ and Eq. (2.9) written as:

$$\frac{\partial C}{\partial t} = D_a \frac{\partial^2 C}{\partial x^2} \quad (2.22)$$

with the following boundary and initial conditions:

$$C(0, t) = C_i(t) \quad (2.23)$$

$$C(\infty, t) = C_0 \quad (2.24)$$

$$C(x, 0) = C_0 \quad (2.25)$$

provided that the “apparent” diffusion coefficient, D_a , is defined as:

$$D_a \equiv \frac{D^{*2}}{D} = D \exp\left(-2 \frac{\Delta E}{k_B T}\right) \quad (2.26)$$

Employing the concentration profile from Eq. (2.22), the rate of accumulation of species at the interface is obtained from Eq. (2.21) as follows [46]:

$$\int_0^\Gamma \frac{1}{g(\lambda)} d\lambda = \left(\frac{D_a}{\pi}\right)^{0.5} \left[2C_0\sqrt{t} - \int_0^t \frac{C_i(\tau)}{\sqrt{t-\tau}} d\tau\right] \quad (2.27)$$

In general, a numerical solution of Eq. (2.27) is necessary [45, 74] and knowledge of the relationship between C_i and Γ is always needed. The latter is provided by thermodynamic adsorption isotherms which are briefly reviewed below.

Thermodynamic isotherms

In a reversible adsorption process, the adsorbed species can desorb from the interface and re-adsorb at the interface later. This behavior ultimately results in the attainment of an equilibrium state between the bulk and the interface and a quantitative relationship between surface concentration (Γ) of the adsorbing species and its concentration in the bulk (C), known as the adsorption isotherm. Several such relationships have been developed assuming monolayer adsorption at the interface and the fundamental thermodynamic consideration of equality of the chemical potentials of the adsorbing species in the bulk and at the interface. A list of the most significant isotherms are presented in Table 2.1 [17].

Table 2.1: Different types of adsorption isotherms [17].

Type	Adsorption isotherm
Henry	$KC = \frac{\Gamma_{eq}}{\Gamma_{max}}$
Freundlich	$KC = \left(\frac{\Gamma_{eq}}{\Gamma_{max}} \right)^{(1/m)}$
Langmuir	$KC = \frac{\Gamma_{eq}}{\Gamma_{max} - \Gamma_{eq}}$
Frumkin	$KC = \frac{\Gamma_{eq}}{\Gamma_{max} - \Gamma_{eq}} \exp\left(-\frac{2\beta\Gamma_{eq}}{k_B T} \right)$
van der Waals	$KC = \frac{\Gamma_{eq}}{\Gamma_{max} - \Gamma_{eq}} \exp\left(\frac{\Gamma_{eq}}{\Gamma_{max} - \Gamma_{eq}} - \frac{2\beta\Gamma_{eq}}{k_B T} \right)$

In this table, K is the adsorption parameter reflecting the surface activity of the adsorbing species. This adsorption parameter is an equilibrium constant defined as the ratio of adsorption rate constant (k_a) to the desorption one (k_d). Large values of K correspond to greater activity of a molecule at the interface. In adsorption isotherms, C denotes the bulk concentration of the adsorbing species and Γ_{eq} and Γ_{max} represent the equilibrium surface concentration and the maximum possible surface concentration, respectively. Each of these isotherms is valid under specific conditions. Henry's isotherm, for instance, assumes that there is no interaction among the adsorbed molecules [28] and, for this reason, is valid only at low concentrations of the adsorbing species. Appropriately, as $\Gamma \rightarrow 0$, all adsorption isotherms (except Freundlich's isotherm which is obtained empirically) reduce to Henry's isotherm [28].

The Langmuir isotherm is most commonly employed for analyzing the adsorption process. In developing this non-linear isotherm, it is assumed that all the interactions and intermolecular forces are negligible. It is also assumed that the adsorbed species do not affect the probability of adsorption of new ones. Moreover, the probability of all adsorption sites at the interface to be occupied by the adsorbing species is identical [28].

Table 2.2: Values of parameters in Eq. (2.27) depending on the chosen thermodynamic adsorption isotherm [46].

Type	C_i	$\int_0^\Gamma \frac{1}{g(\lambda)} d\lambda$
Henry	$\frac{1}{K} \frac{\Gamma_{eq}}{\Gamma_{max}}$	Γ
Freundlich	$\frac{1}{K} \left(\frac{\Gamma_{eq}}{\Gamma_{max}} \right)^{(1/m)}$	Γ
Langmuir	$\frac{1}{K} \frac{\Gamma_{eq}}{\Gamma_{max} - \Gamma_{eq}}$	$\Gamma_{max} \ln \left(\frac{\Gamma_{max}}{\Gamma_{max} - \Gamma} \right)$
Frumkin	$\frac{1}{K} \frac{\Gamma_{eq}}{\Gamma_{max} - \Gamma_{eq}} \exp \left(- \frac{2\beta\Gamma_{eq}}{k_B T} \right)$	$\Gamma_{max} \ln \left(\frac{\Gamma_{max}}{\Gamma_{max} - \Gamma} \right)$
van der Waals	$\frac{1}{K} \frac{\Gamma_{eq}}{\Gamma_{max} - \Gamma_{eq}} \exp \left(\frac{\Gamma_{eq}}{\Gamma_{max} - \Gamma_{eq}} - \frac{2\beta\Gamma_{eq}}{k_B T} \right)$	Γ

At equilibrium conditions, the concentration of the species is uniform in the solution (i.e., $C = C_i = C_s = C_0$). Thus, based on the thermodynamic adsorption isotherms presented in Table 2.1, C_i is directly calculated from different adsorption isotherms and is listed in Table 2.2.

Two arguments have been made for specifying the function $g(\lambda)$ in Eq. (2.27) [13, 46]:

- (i) The adsorption flux does not depend on surface coverage, namely $g(\Gamma) = 1$ (known as linear adsorption).
- (ii) The adsorption flux is proportional to the fraction of non-occupied adsorption sites, measured by $1 - \Gamma/\Gamma_{max}$, such that $g(\Gamma) = 1 - \Gamma/\Gamma_{max}$.

The choice between these two arguments must be consistent with the assumptions underpinning the selected adsorption isotherm. Thus, for Henry, Freundlich, and van der Waals isotherms it is assumed that the adsorption rate is independent of the surface

coverage, whereas for Langmuir and Frumkin isotherms the adsorption rate is assumed to be influenced by the surface coverage [46]. For the case of Henry's isotherm, Eq. (2.27) can be solved analytically [46] as follows:

$$\Gamma(t) = \frac{C_0}{K} \left[1 - \exp(K^2 D_a t) \operatorname{erfc} \left(\sqrt{K^2 D_a t} \right) \right] \quad (2.28)$$

The adsorption model (Eq. (2.27)) is considerably simplified if it can be assumed that equilibrium between the interface and the subsurface is instantaneous (local equilibrium assumption). This assumption was first made in the pioneering work of Ward and Tordai [70], who also assumed that $g(\Gamma) = 1$. Under the assumption of local equilibrium, $C_i = C_s$ and the dynamics of the process are completely controlled by the diffusion of the adsorbing species from the bulk of the solution to the subsurface. No energy barrier hinders the adsorption process.

The diffusion-controlled model

Under the assumption of local equilibrium, the equation of continuity (Eq. (2.9)) is valid in the domain $0 < x < \infty$. Eq. (2.9) is subject to boundary and initial conditions as expressed in Eq. (2.23) to Eq. (2.25) and the rate of change of adsorbed species per unit area of interface (Γ) is equal to the diffusion flux [46]:

$$\frac{\partial \Gamma}{\partial t} = D \left. \frac{\partial C}{\partial x} \right|_{x \rightarrow 0^+} \quad (2.29)$$

Similar to the mixed diffusion-kinetic controlled model, $C(x, t)$ obtained from the solution of Fick's second law of diffusion can be directly employed in Eq. (2.29) to find Γ [46, 70]

$$\Gamma(t) = \left(\frac{D}{\pi} \right)^{0.5} \left[2C_0 \sqrt{t} - \int_0^t \frac{C_i(\tau)}{\sqrt{t-\tau}} d\tau \right] \quad (2.30)$$

where C_0 represents the constant bulk concentration [46]. This model, which was first developed by Ward and Tordai [70], is a special case of the mixed kinetic-diffusion control model [46]. Indeed, when the adsorption flux is independent of surface coverage (i.e., $g(\Gamma) = 1$) and in the absence of an energy barrier ($\Delta E = 0$) (instantaneous adsorption from the subsurface to the interface), D^* reduces to D and (Eq.(2.30)) is recovered from Eq. (2.27) [46]. Fainerman *et al.* [30] have developed asymptotic solutions of Eq. (2.30) which have great utility in the analysis of dynamic surface/interfacial tension data at two extremes: early stages of adsorption and late stages of adsorption.

- **long-time asymptotic result** ($t \rightarrow \infty$)

During the later stages of adsorption, $\Gamma \rightarrow \Gamma_{eq}$ and $C_i \rightarrow C_0$, such that $C_i(\tau)$ may be factored out of the integral in Eq. (2.30). The following asymptotic approximation is thus obtained

$$\Gamma_{eq} \cong \left(\frac{D}{\pi}\right)^{0.5} \left[2C_0\sqrt{t} + 2C(t-\tau)^{0.5} \right]_0^t \quad (2.31)$$

Rearranging Eq. (2.31) results in

$$\Delta C = C_0 - C = \Gamma_{eq} \left(\frac{\pi}{4Dt}\right)^{0.5} \quad (2.32)$$

Assuming an ideal solution, the Gibbs equation for adsorption can be employed to express the activity of a surface-active agent as follows [25]:

$$\left(\frac{\partial\gamma}{\partial\ln C}\right)_{T,P} = -nRT\Gamma_{eq} \quad (2.33)$$

where γ presents the surface (or interfacial) tension, and R is the gas constant. The value for n depends on the type of surfactant. If the surfactant is non-ionic, neutral, or ionic but in large amount of electrolyte, $n = 1$, otherwise $n = 2$ [28, 30]. In Gibbs equation (Eq. (2.33)) it is assumed that the activity is equal to the concentration – an assumption that is valid for dilute solutions [28]. Eq. (2.33) can be written as

$$\frac{d\gamma}{dC} = -\frac{nRT\Gamma_{eq}}{C_0} \quad (2.34)$$

For very small changes in surface tension and concentration, as expected for $t \rightarrow \infty$,

$$\frac{d\gamma}{dC} \cong \frac{\Delta\gamma}{\Delta C} = -\frac{nRT\Gamma_{eq}}{C_0} \quad (2.35)$$

where $\Delta\gamma = \gamma_{eq} - \gamma$ and ΔC is given by Eq. (2.32). Accordingly,

$$\gamma_{eq} - \gamma = -\frac{nRT\Gamma_{eq}^2}{C_0} \left(\frac{\pi}{4Dt}\right)^{0.5} \quad (2.36)$$

$$\Rightarrow \gamma = \gamma_{eq} + \frac{nRT\Gamma_{eq}^2}{C_0} \left(\frac{\pi}{4Dt}\right)^{0.5} \quad (2.37)$$

Using Eq. (2.37), one can obtain the equilibrium surface (or interfacial) tension, γ_{eq} , as the intercept of a plot of long-time DST data against $t^{-0.5}$. Additionally, given an estimate of Γ_{eq} , the diffusion coefficient D may be obtained from the slope of such plot.

- **early-time asymptotic result** ($t \rightarrow 0$)

In the other extreme, when $t \rightarrow 0$, the integral in Eq. (2.30) vanishes and one obtains:

$$\Gamma = 2C_0 \left(\frac{Dt}{\pi} \right)^{0.5} \quad (2.38)$$

During the early stages of adsorption, coverage of the interface is low and Henry's adsorption isotherm (see Table 2.1) applies. This, in combination with Gibbs adsorption equation (Eq. (2.33)), allows one to define Π as [25, 30]:

$$\Pi \equiv \gamma - \gamma_0 = -nRT\Gamma \quad (2.39)$$

in which γ_0 denotes the surface tension of the solvent in the absence of surfactant. In Eq. (2.39), Π is known as the surface pressure, analogous to the bulk pressure. Substituting Eq. (2.39) into Eq. (2.38) results in

$$\gamma = \gamma_0 - 2nRTC_0 \left(\frac{Dt}{\pi} \right)^{0.5} \quad (2.40)$$

Eq. (2.40) shows that the surface tension varies linearly with $t^{0.5}$ during the early stages of adsorption (i.e., as $t \rightarrow 0$). Thus, a plot of early-time DST data against $t^{0.5}$ is expected to give γ_0 as the intercept and a slope from which the diffusion coefficient, D , may be readily estimated. Recall that the diffusion coefficient of the surface-active species may also be estimated from late-time DST data using Eq. (2.37). In fact, the two estimates are expected to agree with each other and also with the estimate obtained from the Stokes-Einstein equation if the assumptions underpinning the analysis of Ward and Tordai hold.

The asymptotic results, Eq. (2.37) and Eq. (2.40), have been applied extensively in investigations of the dynamic surface/interfacial tension of different types of surfactant solutions [12, 21, 23, 24, 34, 42, 52, 56, 58, 60, 66, 69, 72, 73]. Recently, the suitability of these equations to describe the adsorption dynamics of small nanoparticles ($< 6\text{nm}$) was also examined [31, 44]. Kutuzov *et al.* [44] studied the adsorption of 2.3- and 6-nm cadmium selenide (CdSe) nanoparticles stabilized by trioctylphosphine oxide (TOPO) at the toluene-water interface. They found that, as the bulk concentration of nanoparticles increased, the diffusion coefficient, D , estimated from Eq. (2.37) diminished in magnitude from the value predicted by the Stokes-Einstein theory of diffusion. This apparent reduction of the diffusion coefficient was thought to originate from the presence of an energy

barrier to adsorption. An Arrhenius-type equation, see Eq. (2.19), was used to relate the real diffusion coefficient, obtained from Stokes-Einstein theory of diffusion, and a so-called “effective diffusion coefficient”, calculated from analysis of DST data using the long-time asymptotic result [44]:

$$D_{eff} = D \exp\left(-\frac{\Delta E_p}{k_B T}\right) \quad (2.41)$$

Using Eq. (2.41), the adsorption energy barrier was estimated and found to be of the same order of magnitude as ΔE estimated from Eq. (2.2) (i.e., of the order of a few $k_B T$) and independent of the particle size. Kutuzov *et al.* [44] speculated on the physical origin of such an adsorption barrier in terms illustrated schematically in Figure 2.8. They argued that, as the number of adsorbed particles at the interface increases, the number of collisions of nanoparticles approaching the interface with those already adsorbed at the interface and with those desorbing from the interface due to thermal fluctuations, increases. These collisions hinder the adsorption of new particles, a hindrance manifested as an energy barrier (ΔE_p) within the subsurface layer. The thickness of the region below the interface where this energy barrier is effective depends on the magnitude of particle-to-particle and particle-interface interactions [44]. This adsorption energy barrier vanishes during the early stages of the adsorption, when the interface is relatively clean and thus, the only resistance to adsorption is due to diffusion of nanoparticles from the bulk to the subsurface [44].

In a similar study, Ferdous *et al.* [31] investigated the adsorption of gold nanoparticles capped by either dodecanethiol or hexanethiol at hexane-water interface. The diffusion coefficient of 2.8 nm n-dodecane-1-thiol-capped gold nanoparticles was calculated from DST data using both Eq. (2.37) and Eq. (2.40)). Estimates of the diffusion coefficient based on early-time DST data were in line with the prediction of the Stokes-Einstein equation for the most dilute solutions, but the results generally showed (i) a decrease of both estimates with increasing concentration of nanoparticles in the bulk solution and (ii) smaller estimates from Eq. (2.37) than Eq. (2.40)) for solutions of all nanoparticle bulk concentrations. These observations corroborated the observations of Kutuzov *et al.* [44] and Eq. (2.41) was employed to estimate the adsorption energy barrier. It was found that the magnitude of this barrier was $\sim 10k_B T$ for both types of capping agents. Using this value for the adsorption energy in Eq. (2.3), the contact angle was found to be 157° (measured from the aqueous phase) and independent of the type of nanoparticles.

In order to measure the adsorption energy of nanoparticles, Du *et al.* [26] have recently proposed a method based on thermodynamic relations. They have shown that the adsorption energy can be calculated as:

$$\Delta E = \frac{\gamma_{eq} - \gamma_0}{\theta_{\max}} \pi r^2 \quad (2.42)$$

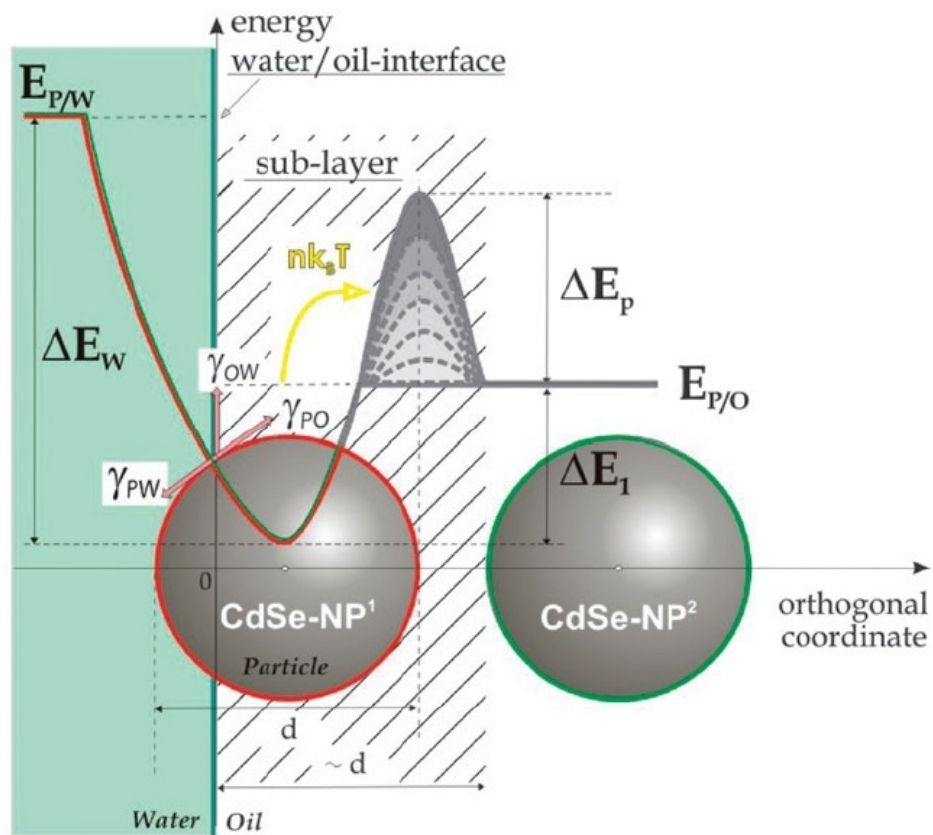


Figure 2.8: Schematic energy diagram of CdSe nanoparticle adsorption at the oil-water interface [44]. In this figure, γ is the interfacial tension, d is the particle diameter E is Gibbs free energy, and the subscripts W , O , and P denote *water*, *oil*, and *particle*, respectively. ΔE_1 represents the adsorption energy and ΔE_p is the potential barrier for adsorption.

where θ_{\max} represents the maximum coverage of the interface by nanoparticles, which was assumed by these authors to be equal to 0.91 – the value corresponding to hexagonal close packing [26]. The adsorption energy of citrate-stabilized gold (Au-cit) nanoparticles at 2,2,3,3,4,4,5,5-octafluoropentyl acrylate (OFPA)-water interface has been calculated using Eq. (2.42) and plotted in Figure 2.9 as a function of particle size. As shown in this figure,

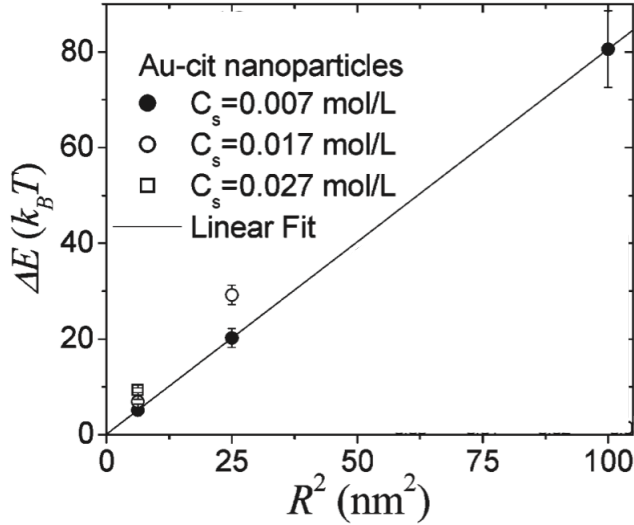


Figure 2.9: The adsorption energy of Au-cit nanoparticles with different sizes at OFPA-water interface [26].

the adsorption energy is found to be -5.1 ± 0.5 , -20 ± 2 , and $-80 \pm 8 k_B T$ for the particles with radius of 2.5, 5, and 10 nm, respectively, which shows that $\Delta E \propto r^2$. Moreover, it was found in that study that for the smallest nanoparticle (i.e., 2.5 nm), which had an adsorption energy of $\sim -5k_B T$ and thus comparable to energy of thermal fluctuations, the adsorption process is reversible. Evidence for this was provided by diluting the solution of nanoparticles after its equilibrium had been reached. As a result of the dilution, the interfacial tension increased as shown in Figure 2.10.

However, for the larger particles (i.e., 5 nm and 10 nm in radius), the interfacial tension did not increase after dilution signifying irreversible adsorption of these particles at the interface [26]. These observations are in a reasonable agreement with simulation investigations of the adsorption of solid particles at oil-water interface with different adsorption energy [38]. As shown in Figure 2.11, for particles with adsorption energy larger than $50 k_B T$, the interface can be fully covered (91% coverage) and the adsorption process becomes

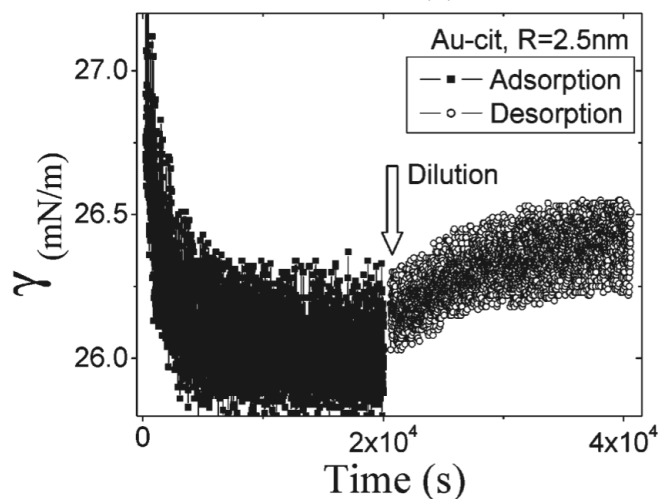


Figure 2.10: The effect of diluting the solution of nanoparticles on the interfacial tension of OFPA-water. Increasing in interfacial tension corresponds to the desorption of the nanoparticles from the interface [26].

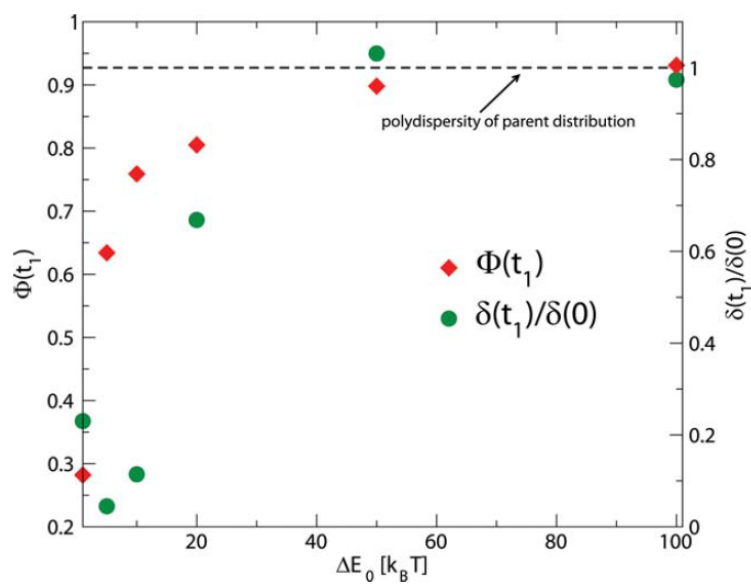


Figure 2.11: The maximum surface coverage for particles with different adsorption energy [38]. Φ represents surface coverage equivalent to θ in this study.

irreversible. The magnitude of the adsorption energy depends not only on the particle size, but also on the type of the interface. Hence, combinations of particle sizes and the fluid-fluid interfaces may result in different adsorption energy and eventually either a reversible or an irreversible adsorption process.

2.3.2 Irreversible adsorption

A large adsorption energy implies that the adsorption takes place irreversibly [8]. In this case, the adsorption isotherm is of little use in the modeling of the adsorption process. Instead, modeling the irreversible adsorption of colloidal particles has been pursued on the basis of generalized random sequential adsorption (RSA) theory. In the past decade, Adamczyk and coworkers have enriched this theory to explore the adsorption of different types of micron-size colloidal particles at different solid-liquid interfaces [4, 1, 2, 3, 5, 6, 8, 67]. To the best of our knowledge, application of this theory to the adsorption of nanoparticles on fluid-fluid interfaces has never been attempted before.

Modeling the transfer of particles in terms of the continuity equation under isobaric-isothermal conditions results in a phenomenological transport model (i.e., Fick’s second law of diffusion) showing a “linear adsorption regime” [67]. Unfortunately, this model cannot explain the adsorption process over the entire range of surface coverage. The incapability of the linear model to explain the adsorption of colloidal particles is due to a phenomenon known as the “blocking effect”. This effect is originated from the influence of adsorbed particles on adsorbing ones, where adsorbed particles hinder the adsorption process [67]. Note that a similar effect was thought to give rise to the mixed-kinetic-diffusion control discussed in a previous section. The RSA theory seeks to directly quantify this phenomenon and its consequences for the adsorption process.

To develop the RSA model it is assumed that [5, 67]:

- Particles adsorb randomly at adsorption sites, which are accessible with equal probability.
- Particles adsorb permanently. In other words, if a particle adsorbs, its position cannot be changed (“localized adsorption postulation”).
- The adsorption process continues until full (“jamming”) coverage of the interface is obtained.

Under conditions of constant temperature and pressure, the adsorption flux at the interface reads [67]

$$\frac{\partial C}{\partial t} + \nabla \cdot \vec{j} = 0 \quad (2.43)$$

where \vec{j} is the particle flux vector, written as [67]:

$$\vec{j} = -\hat{D} \cdot \left(\frac{\nabla \mu}{k_B T} + \frac{\nabla \phi}{k_B T} \right) C + \vec{U}_p C \quad (2.44)$$

where C is the particle number concentration, \hat{D} and \vec{U}_p are the diffusion tensor and the particle velocity vector, respectively. In Eq. (2.44) μ denotes the chemical potential and ϕ represents the specific interaction energy of particles [1, 67]. It is shown in [7] that by solving the DLVO equations for similarly charged particles and interfaces, the energy profile shown in Figure 2.12 appears. In this figure, ϕ_b represents a maximum energy barrier at the distance δ_b . The magnitude of this energy barrier is affected by the electrolyte concentration and composition, the Hamaker constant, and the particle size, shape, and orientation [67]. This energy barrier hinders the adsorption of particles and makes δ_b an unstable position for particles, with the result that the particle concentration (denoted by n in Figure 2.12) becomes zero at δ_b . The minimum energy value ϕ_m (referred as the primary minimum) shown at δ_m corresponds to the most stable condition in terms of interaction energy [7, 67]. The magnitude of ϕ_m dictates the reversibility of colloidal particle adsorption under static and no-flow conditions [67]. Assuming negligible flow contributions in the subsurface layer, one-dimensional diffusion (x direction), and activity equal to concentration (i.e., quasidilute limit), Eq. (2.43) can be written as [1, 67]:

$$\frac{\partial C}{\partial t} = \frac{\partial}{\partial x} \left[D(x) \exp\left(-\frac{\Phi}{k_B T}\right) \frac{\partial}{\partial x} \left[C \exp\left(\frac{\Phi}{k_B T}\right) \right] \right] \quad (2.45)$$

where Φ denotes the net interaction energy of particles (overall potential). A key objective of the RSA model is to determine the function Φ . In the generalized RSA model, which considers three-dimensional motion of the particles within the adsorption layer, Φ is assumed to be a function of the position-dependent blocking function $B(\theta, x)$ as [67]:

$$\Phi = \phi - k_B T \ln B(\theta, x) \quad (2.46)$$

where θ denotes the surface coverage defined as $\theta \equiv S\Gamma$, where S is the characteristic cross section of a particle (in the case of spheres $S = \pi r^2$) [67]. Considering Eq. (2.46), Eq. (2.45) is integrated within the subsurface layer and under quasistationary conditions one obtains [67]:

$$-j = k_a C_s \bar{B}(\theta) - \frac{k_d \theta}{S} \frac{\bar{B}(\theta)}{B_0(\theta)} \quad (2.47)$$

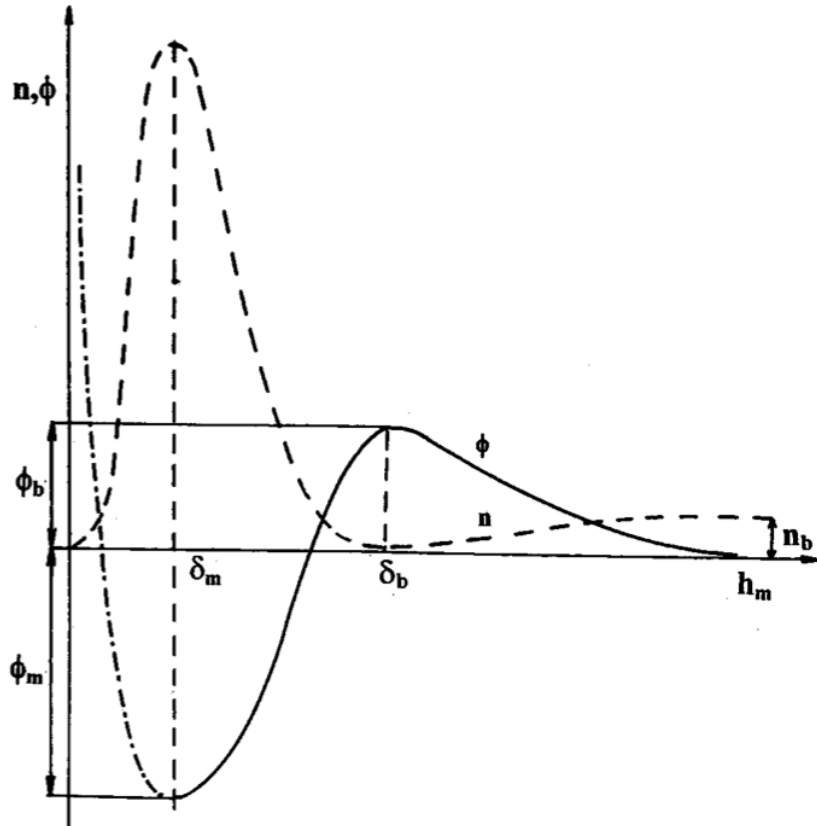


Figure 2.12: The energy profile (ϕ) of likely charged particle and the interface [7]. ϕ_b and ϕ_m represent the energy barrier (at the distance of δ_b from the interface) and the adsorption energy (at the distance of δ_m from the interface), respectively. n and n_b denote the particle number concentration near the interface and in the bulk, and h_m is the minimum separation distance.

where B_0 is the blocking function, and \bar{B} is the generalized blocking function (transport resistance of the adsorbed layer) [67], analogous to the function $g(\Gamma)$ in the mixed diffusion-kinetic controlled model. If one compares Eq. (2.47) to Eq. (2.13), one further observes that the function $f(\Gamma)$ in the mixed diffusion-kinetic model corresponds with $\bar{B}(\theta)/B_0(\theta)$ in the generalized RSA model. It must be noted that the number concentration of the particles in solution must be large enough so that at anytime $C_s \cong C_0$. Applying the definition of θ for an irreversible adsorption process ($k_d = 0$) on Eq. (2.47), the adsorption flux can be written as [67]:

$$\frac{1}{S} \frac{\partial \theta}{\partial t} = k_a C_0 \bar{B}(\theta) \quad (2.48)$$

Similar to the asymptotic solutions developed for the Ward and Tordai's equation, the generalized RSA model of irreversible adsorption is simplified at the two extremes of early-stage and late-stage adsorption.

Early in the adsorption process the interface is clean and the blocking effect has no impact ($\bar{B}(\theta) \rightarrow 1$ as $t \rightarrow 0$), such that the adsorption process is controlled exclusively by diffusion. Moreover, for a planar interface, the adsorption “constant” is given by $k_a = (D/\pi t)^{0.5}$ [67]. Consequently, Eq. (2.48) is solved to give the dynamics of surface coverage for a planar interface during the early stages of adsorption as follows [67]:

$$\theta = 2\pi r^2 C_0 \left(\frac{Dt}{\pi} \right)^{0.5} \quad (2.49)$$

According to Eq. (2.49), the surface coverage at the beginning of the adsorption process is proportional to $t^{0.5}$.

Late in the adsorption process, when the interface is approaching full coverage, the blocking effect is significant and the blocking function may no longer be assumed to be equal to unity. It has been shown that at high surface coverage (long time of adsorption), the generalized blocking function can be approximated by [7, 67]:

$$\bar{B}(\theta) \cong B_0(\theta) \cong \left(1 - \frac{\theta}{\theta_{\max}} \right)^m \quad (2.50)$$

where θ_{\max} denotes the maximum surface coverage and m is the fitting parameter. m can have values of 3, 4, or 5, depending on the shape of particles (for spheres $m = 3$). Comparing $\bar{B}(\theta)$ from Eq. (2.50) to what the Langmuir isotherm proposes for function $g(\Gamma)$ (i.e., $g(\Gamma) = (1 - \theta/\theta_{\max})$), it becomes clear that the RSA model predicts a stronger blocking effect. Numerical calculations have shown [1, 67] that if the condition

$$\theta > \theta_{\max} \left[1 - \left(\frac{1}{10(m-1)\bar{k}_a} \right)^{\frac{1}{m}} \right] \quad (2.51)$$

is met, then the approximate Eq. (2.50) can be safely employed to describe the blocking function in Eq. (2.48). Integrating Eq. (2.48) then results in the following expression for the surface coverage during the late stages of adsorption [1, 67]:

$$\theta = \theta_{\max} - \frac{K_l}{\pi r^2 C_0} \left(\frac{1}{Dt} \right)^{0.5} \quad (2.52)$$

The parameter K_l is the so-called “long-time expansion coefficient” [67], itself a function of the dimensionless adsorption rate constant, \bar{k}_a , is defined as [1, 67]:

$$K_l \equiv \theta_{\max} \left(\frac{\theta_{\max}}{(m-1)\bar{k}_a} \right)^{\frac{1}{m-1}} \quad (2.53)$$

The latter quantity is defined for spherical particles as follows:

$$\bar{k}_a = \frac{k_a}{\pi r^2 C_0 D} \quad (2.54)$$

where C_0 is the bulk particle number concentration. To apply the generalized RSA model, one must be able to measure the surface coverage, usually by direct methods (e.g. [43, 51]) – a notoriously difficult task for adsorbed nanoparticles. It is a key objective of this work to establish the connection between dynamic surface tension and dynamic surface coverage – a connection that would potentially expand the range of applicability of the RSA model to irreversible adsorption of nanoparticles at fluid-fluid interfaces.

Chapter 3

Theoretical Investigations

3.1 Adsorption Energy and Surface Tension

The Gibbs free energy of an interface is a function of the temperature, the pressures of the phases on either side of the interface, the number of moles of adsorbed species, and the interfacial area [25]. At constant temperature and phase pressures, the Gibbs free energy for a solution containing surface-active nanoparticles is expressed as:

$$dG = \left(\frac{\partial G}{\partial A} \right)_{T, P^I, P^{II}, n} dA + \left(\frac{\partial G}{\partial n} \right)_{T, P^I, P^{II}, A} dn \quad (3.1)$$

where A denotes the interfacial area and n is the number of moles of adsorbed nanoparticles. By definition, the surface (or interfacial) tension is:

$$\gamma \equiv \left(\frac{dG}{dA} \right)_{T, P^I, P^{II}, n} \quad (3.2)$$

For $n=0$ Eq. (3.2) defines the surface (or interfacial) tension γ_0 of a clean interface. Furthermore, the energy change associated with the adsorption of a single nanoparticle at the interface is defined as:

$$\Delta E \equiv \left(\frac{dG}{dn} \right)_{T, P^I, P^{II}, A} \quad (3.3)$$

The above considerations allow the total differential of the Gibbs free energy of an interface to be written as follows:

$$dG = \gamma_0 dA + \Delta E dn \quad (3.4)$$

The latter term in Eq. (3.4) accounts for changes in the Gibbs free energy due to the adsorption of nanoparticles. ΔE is the energy change associated with the adsorption of a single nanoparticle, which as discussed earlier (see Eq. (2.3)) is negative. Dividing Eq. (3.4) by dA one obtains:

$$\frac{dG}{dA} = \gamma_0 + \Delta E \frac{dn}{dA} \quad (3.5)$$

The left hand-side of Eq. (3.5) may be identified equal to γ as expressed in Eq. (3.2). The term dn/dA in the right-hand side of Eq. (3.5) represents the surface concentration, Γ . As noted in the previous chapter the surface coverage is defined as $\theta \equiv \Gamma S$, where S is πr^2 for spheres. On the basis of these considerations, Eq. (3.5) is restated as:

$$\gamma = \gamma_0 + \frac{\theta}{\pi r^2} \Delta E \quad (3.6)$$

Rearranging Eq. (3.6) to solve for ΔE results in the following:

$$\Delta E = \frac{\gamma - \gamma_0}{\theta} \pi r^2 \quad (3.7)$$

Similar to Pieranski's equation (Eq. (2.3)), Eq. (3.7) also shows that the adsorption energy is proportional to the square of particle radius. Pieranski's equation, however, involves the contact angle, which is extremely difficult to determine for nanoparticles [48, 68], whereas Eq. (3.7) relates ΔE to the readily measurable surface (or interfacial) tension and to the surface coverage. As mentioned earlier, the latter quantity is not easy to determine experimentally, but can be estimated as will be shown below. During the process of nanoparticle adsorption, the surface tension, γ , the surface concentration, Γ , and the surface coverage, θ , are all varying with time. Strictly speaking, Eq. (3.7) applies to equilibrium (or steady-state in the case of irreversible adsorption) conditions and this is how it was first proposed by Du *et al.* [26]:

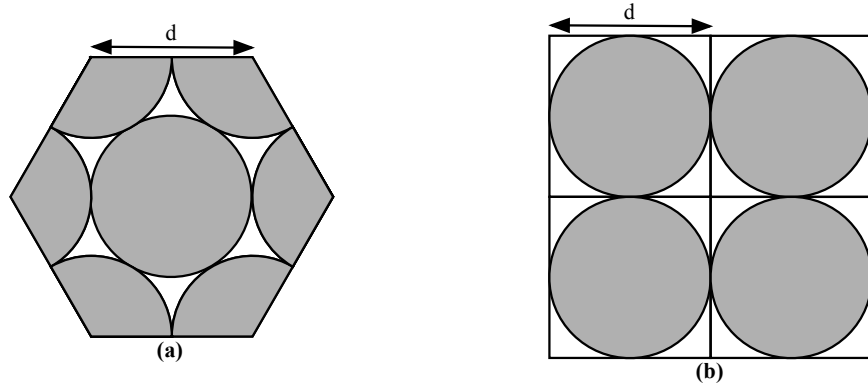
$$\Delta E = \frac{\gamma_{eq} - \gamma_0}{\theta_{\max}} \pi r^2 \quad (2.42)$$

where γ_{eq} is the equilibrium surface tension and θ_{\max} denotes the maximum surface coverage.

The value of θ_{\max} for use in the above equation depends on assumptions regarding the equilibrium (steady-state) arrangement of nanoparticles at the interface. As shown in Figure (3.1) geometric considerations suggest a maximum surface coverage of 91% or 78% for hexagonal (close packed) or square nanoparticle arrangements. The former value

is supported by numerical simulations of irreversible adsorption of nanoparticles at fluid-fluid interfaces conducted recently by Isa *et al.*[38] but, to the best of our knowledge, has not yet received experimental confirmation. Both Du *et al.* [26] and Isa *et al.*[38] have calculated the adsorption energy ΔE from equilibrium (steady-state) surface tension data assuming $\theta_{\max} \cong 0.91$.

The present work departs from published research in that it views Eq. (3.7) in the context of quasi-steady state approximation. Namely, it is assumed that Eq. (3.7) is valid *throughout* the adsorption process and used to determine surface coverage, θ , as a function of time from knowledge of DST. Importantly, Eq. (3.7) is *not* used to determine ΔE . Rather, a completely new equation for the determination of ΔE is developed, which makes no reference to surface coverage.



$$\theta_{\max} = \frac{\text{occupied area (grey region)}}{\text{total area}} \Rightarrow \left\{ \begin{array}{l} (a): \theta_{\max} = \frac{3\pi\left(\frac{d}{2}\right)^2}{\frac{3\sqrt{3}}{2}d^2} \cong 0.91 \\ (b): \theta_{\max} = \frac{\pi\left(\frac{d}{2}\right)^2}{d^2} \cong 0.78 \end{array} \right.$$

Figure 3.1: Geometrical patterns for nanoparticles in covering the interface (a) hexagonal close packed (b) square pattern.

3.2 Irreversible Adsorption Analysis

As discussed earlier, the generalized RSA model can be employed to explore the dynamics of an irreversible adsorption process. The following equation holds true during the late stages of adsorption:

$$\theta = \theta_{\max} - \frac{K_l}{\pi r^2 N_A C_0} \left(\frac{1}{Dt} \right)^{0.5} \quad (2.52)$$

where C_0 represents the bulk molar concentration of nanoparticles, D is the nanoparticle diffusion coefficient, r is the particle radius, t is time, and K_l is a constant the value of which depends on the adsorption rate constant. Substituting expressions for θ and θ_{\max} obtained from Eq. (3.7) and Eq. (2.42), respectively, into Eq. (2.52) results in the following:

$$\gamma = \gamma_{eq} - \frac{K_l \Delta E}{(\pi r^2)^2 N_A C_0} \left(\frac{1}{Dt} \right)^{0.5} \quad (3.8)$$

where N_A is Avogadro's number. As shown in Eq. (3.8), surface tension varies linearly with $t^{-0.5}$ during the later stages of an irreversible adsorption process, which is a trend identical to what the asymptotic solution of Ward and Tordai's equation predicts for reversible adsorption, namely Eq. (2.37) [70, 30]:

$$\gamma = \gamma_{eq} + \frac{nRT\Gamma_{eq}^2}{C} \left(\frac{\pi}{4Dt} \right)^{0.5} \quad (2.37)$$

Thus, the equilibrium surface tension can be obtained as the intercept of plots of late-time DST data against $t^{-0.5}$. As discussed previously, Eq. (2.37) has been used to analyze the dynamic interfacial tension data of small nanoparticles, which adsorb reversibly on fluid-fluid interfaces [38, 44, 31].

In regards to the early stages of irreversible adsorption, Eq. (3.7) is rearranged to obtain the surface coverage as follows:

$$\theta(t) = \frac{-(\gamma_0 - \gamma(t))\pi r^2}{\Delta E} \quad (3.9)$$

where $\gamma(t)$ is obtained directly from DST measurements. As discussed previously, the RSA theory provides the following asymptotic result for the surface coverage during the early stages of adsorption (i.e., for small values of θ):

$$\theta = 2\pi r^2 N_A C_0 \left(\frac{Dt}{\pi} \right)^{0.5} \quad (2.49)$$

where C_0 is the molar bulk concentration of EC nanoparticles. Eliminating θ between Eq. (3.9) and Eq. (2.49), we obtain:

$$\gamma(t) = \gamma_0 + 2N_A \Delta E C_0 \left(\frac{Dt}{\pi} \right)^{0.5} \quad (3.10)$$

The above result, Eq. (3.10), is completely novel. It should enable one to determine the adsorption energy, ΔE , by knowing the particle size, the bulk concentration of particles, physical properties of the liquid phase, and more importantly, dynamic surface (interfacial) tension. Unlike Eq. (2.42), knowledge of θ_{\max} is not required. In fact, Eq. (3.9) can be used to check the predictions of (2.42), which are based on the assumption that $\theta_{\max} \cong 0.91$.

Recall that the adsorption energy of surfactants and very small nanoparticles ($< 5\text{nm}$) is of the order of a few $k_B T$. In fact, for $\Delta E \cong -k_B T$, Eq. (3.10) is reduced (as it should) to the result reported by Ward and Tordai [70, 30] for reversible adsorption:

$$\gamma = \gamma_0 - 2RT C_0 \left(\frac{Dt}{\pi} \right)^{0.5} \quad (2.40)$$

Chapter 4

Experimental Methods and Materials

4.1 Nanoparticle Synthesis and Characterization

Jin *et al.* [41] have developed a facile recipe to synthesize EC nanoparticles. In this project, minor modifications on their method are made to synthesize EC nanoparticles in an aqueous phase, as shown in Figure 4.1. To start, a solution (10.7 g/L) of EC (Sigma-

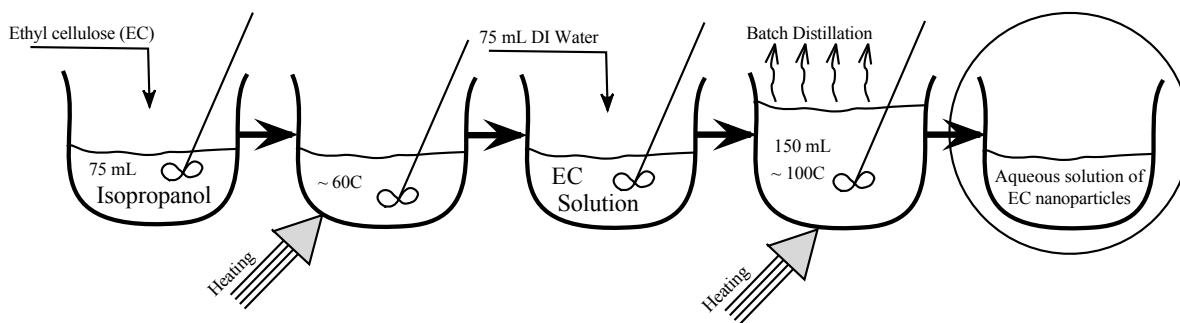


Figure 4.1: Steps of EC nanoparticle synthesis.

Aldrich, product code: 247499-100G) in isopropyl alcohol HPLC grade (Caledon, product code: 8601-7) is prepared. This transparent but milky solution is obtained by adding EC to isopropyl alcohol under stirring and heating to $\sim 75^{\circ}\text{C}$ for approximately 30 min on a hot plate with a magnetic stirrer. Subsequently, an equal volume of deionized (DI) water is added to the solution, which causes the solution to become turbid due to an anti-solvent effect. This anti-solvent step results in the formation of EC nanoparticles. Stirring is

maintained and the temperature is raised to the boiling point of the water - isopropyl alcohol mixture. Note that water and isopropyl alcohol make a non-ideal solution having an azeotropic point at an alcohol mole fraction of 0.6813 [20]. The mole fraction of alcohol in a 50 vol. % solution of water - isopropyl alcohol mixture is 0.1905 (see Appendix A for more details), ensuring continuous enrichment of the liquid phase in water during batch distillation. As shown in Figure 4.1, heating continues until at least 50% of the initial volume has evaporated. The amount of alcohol remaining in the final solution is found from batch distillation calculations (see Appendix A) to be less than 0.3 mol%. The mass concentration of EC in the final solution is calculated to be ~ 15 g/L. The final solution is diluted by DI water to the desired concentrations. Of interest is the molar concentration of EC *nanoparticles* which may be obtained from the following:

$$C = \frac{\rho}{\frac{4}{3}\pi r^3 \rho_p N_A} \quad (4.1)$$

where ρ is the mass concentration of EC, ρ_p is the density of EC (reported 1140 g/L by the manufacturer), and $\frac{4}{3}\pi r^3$ is the volume of a EC nanoparticle of radius r .

A modification of the synthesis method, in which the initial EC concentration in the alcohol is adjusted to one tenth (i.e., 1.07 g/L) of the original value, influences the effectiveness of the anti-solvent step and results in the preparation of smaller nanoparticles. In both cases, highly stable aqueous colloidal solutions of EC nanoparticles were obtained. The stability of EC nanoparticles at neutral pH is due to the electrostatic repulsive force induced by negative charges at the particle surface [41].

The size of the nanoparticles in the solution was determined using dynamic light scattering (DLS). DLS is an optical method in which the evolution with time of the intensity of light scattered by the particles, $\langle I(t) \rangle$ is measured and analyzed [55]. The scattered light intensity shows fluctuations which are correlated over delay times, τ , due to the diffusive motion of the nanoparticles (the scattering objects) within the colloidal solution. Light intensity correlations persist over longer delay times for larger particles because their diffusion coefficient is smaller. Specifically, the time series $\langle I(t) \rangle$ is used to compute the normalized autocorrelation function defined as follows [55]:

$$g(\tau) = \frac{\langle I(t)I(t+\tau) \rangle}{\langle I(t) \rangle^2} \quad (4.2)$$

The normalized autocorrelation function for a monodisperse colloidal solution is related to the particle diffusion coefficient as follows:

$$g(\tau) = 1 + \beta \exp(-2D\mu^2\tau) \quad (4.3)$$

where β is the signal amplitude of the autocorrelation function, D is the translational diffusion coefficient, $\mu = 4\pi\sin(\theta/2)/\lambda$ in which θ is the detection angle with respect to the direction of the incident beam and λ is the wavelength of light in a given solvent [55].

Analyzing the time series $\langle I(t) \rangle$ in terms of Eq. (4.2) and Eq. (4.3) allows determination of the diffusion coefficient of particles in the colloidal solution. By assuming a spherical shape and using the calculated diffusion coefficient, the hydrodynamic radius of particles is then calculated from the Stokes-Einstein theory of diffusion (see section 2.2) [55]. For a polydisperse colloidal solution, the decay of autocorrelation function is more complex (multi-exponential) and its deconvolution to produce the distribution of particle hydrodynamic radii requires numerical inversion methods (see [55] and references therein). In this work, the hydrodynamic diameter of nanoparticles was measured using Brookhaven Ins. Corp. 90 Plus Particle Size Analyzer. One drop of the colloidal solution of EC nanoparticles was diluted by DI water in a 10 mL cuvette and a value of the refractive index of EC equal 1.59 [41] was used. The particle size distribution determined by the instrument was recorded in terms of %number of particles.

The morphology of EC nanoparticles can be detected using electron microscopy techniques. Transmission electron microscopy (TEM), scanning electron microscopy (SEM), and atomic force microscopy (AFM) are all suitable for nano-scale observation. The size of EC nanoparticles prepared in this work is ~ 100 nm or smaller and the TEM approach was chosen. A TEM works exactly similar to conventional light microscopes except that the light source in a TEM is an electron gun instead of visible light in conventional microscopes. A Philips CM12 TEM at the Canadian Centre for Electron Microscopy at McMaster University was used in this project to investigate the morphology of synthesized EC nanoparticles. One drop of the colloidal solution of EC nanoparticles with concentration of 0.1 wt.% was trickled on a 200 mesh copper grid and left to dry under air. After complete drying of the liquid phase, the TEM images are obtained.

4.2 Measurement of Surface Tension

As shown in previous chapters, DST data can be used to probe the dynamics of adsorption of surface active species on fluid-fluid interfaces. Axisymmetric drop shape analysis (ADSA) of the profile of a pendant drop was employed in this project to measure the dynamic surface tension (DST). This is one of many techniques that have been developed for measuring surface tension [9], and has been used extensively for measuring the DST of either surfactant or colloidal solutions [12, 24, 26, 31, 38, 42, 56, 57, 62, 71].

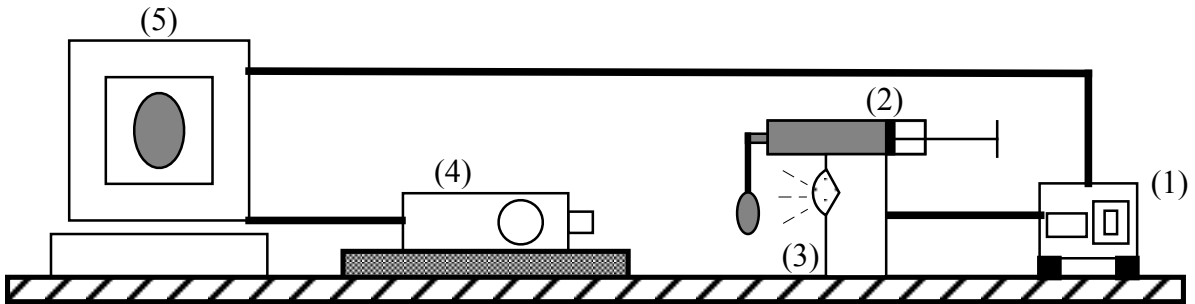


Figure 4.2: The pendant drop tensiometer setup: (1) syringe controller, (2) micro syringe containing the colloidal solution, (3) light source, (4) high-speed CCD camera, and (5) PC.

A schematic of a computerized pendant drop instrument is shown in Figure 4.2. Using the syringe controller, a preset sample volume ($\sim 10\mu\text{L}$ for dilute solutions) is dispensed to create a pendant drop using a steel needle. Testing of colloidal solutions containing increasing concentration of EC nanoparticles requires dispensing smaller sample volumes because these colloidal solutions are characterized by lower surface tension values which cause large drops to detach. A high-speed CCD camera is programmed to capture images of the pendant drop at a specified rate. For fast scanning (needed to probe the earlier stages of adsorption), a frame rate of 10 images per second is used over a time period of 10 to 90 seconds, depending on the EC nanoparticle concentration (the shortest image capture time used for the most concentrated colloidal solutions). Lower frame rates were used to probe the later stages of the adsorption process. Specifically, a frame rate of 6 images per minute was used for the smallest EC concentration and a frame rate of 24 images per minute for the most concentrated one. Accordingly, the period of image capture varied from a couple of hours (~ 8000 seconds) for the least concentrated colloidal solutions to a couple of minutes (~ 2000 seconds) for the most concentrated ones.

A pendant drop is subjected to the forces of gravity and surface tension: the gravity force tends to elongate the droplet, whereas surface tension tends to minimize the interfacial area by keeping the shape of the droplet close to spherical. The shape of the droplet is the result of a balance between these two forces. The ADSA approach determines surface tension by numerically fitting the Laplace equation [9] to the entire profile of a pendant drop, as shown in Figure 4.3.

$$\Delta P = \gamma \left(\frac{1}{R_1} + \frac{1}{R_2} \right) \quad (4.4)$$

where γ is the surface (or interfacial) tension, R_1 and R_2 are the principal radii of the curvature of the interface, and ΔP is the hydrostatic pressure difference.

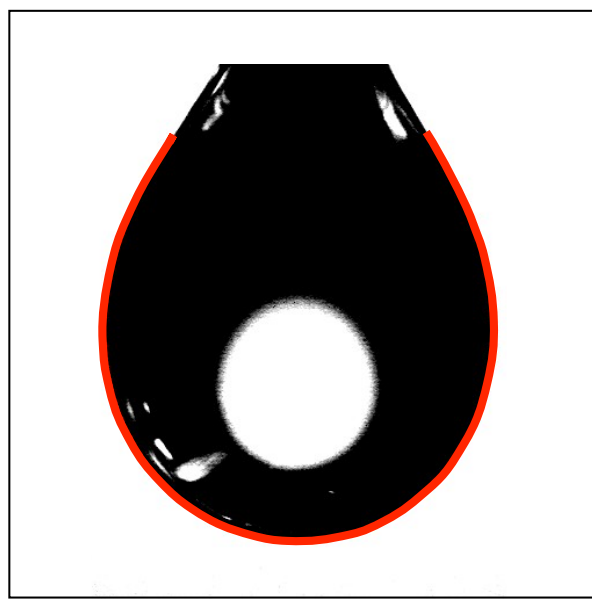


Figure 4.3: Fitting Laplace equation on the entire profile of an aqueous droplet containing EC nanoparticles.

The DST of aqueous solutions of EC nanoparticles in the range 0.05 to 1.0 g/L was measured in this work using a VCA 2500 XE equipment and associated software (AST Products, Billerica, MA). As mentioned earlier, a droplet of volume $\sim 10\mu\text{L}$, depending on the concentration, was suspended from a stainless steel needle attached to a $500\mu\text{L}$ syringe. To minimize evaporation, the pendant drop was created inside a plastic cuvette covered with Parafilm. The DST of at least three droplets at each concentration was measured in order to assess the reproducibility of experimental data.

It was imperative in this study to establish the extent to which surface tension decreases as a result of nanoparticle adsorption at the interface. Since the colloidal solutions contain a small amount of isopropyl alcohol in water, the DST of water-isopropyl alcohol mixtures (0.3 mol% alcohol or less, corresponding to the concentration of isopropyl alcohol in the various colloidal solutions) in the absence of EC nanoparticles was also measured. Furthermore, although EC is completely insoluble in water, the possibility exists for water-soluble impurities initially present in the EC powder to contaminate the colloidal solution. This eventuality was investigated by contacting EC with Milli-Q water for at least three days and then measuring the DST of the supernatant.

Chapter 5

Results

5.1 EC Nanoparticle Characterization

Highly stable aqueous colloidal solutions of EC nanoparticles, shown in Figure 5.1, were successfully obtained following the synthesis route described in Section 4.1. Figure 5.2



Figure 5.1: EC colloidal solution of ~ 15 g/L (1.5 wt.%) more than 9 months after the synthesis.

shows DLS and TEM results for EC nanoparticles synthesized from a starting solution containing 10.7 g/L of EC in isopropyl alcohol. These data support the conclusion that the EC nanoparticles are spherical in shape with diameters narrowly distributed around a mean value of 89.1 nm.

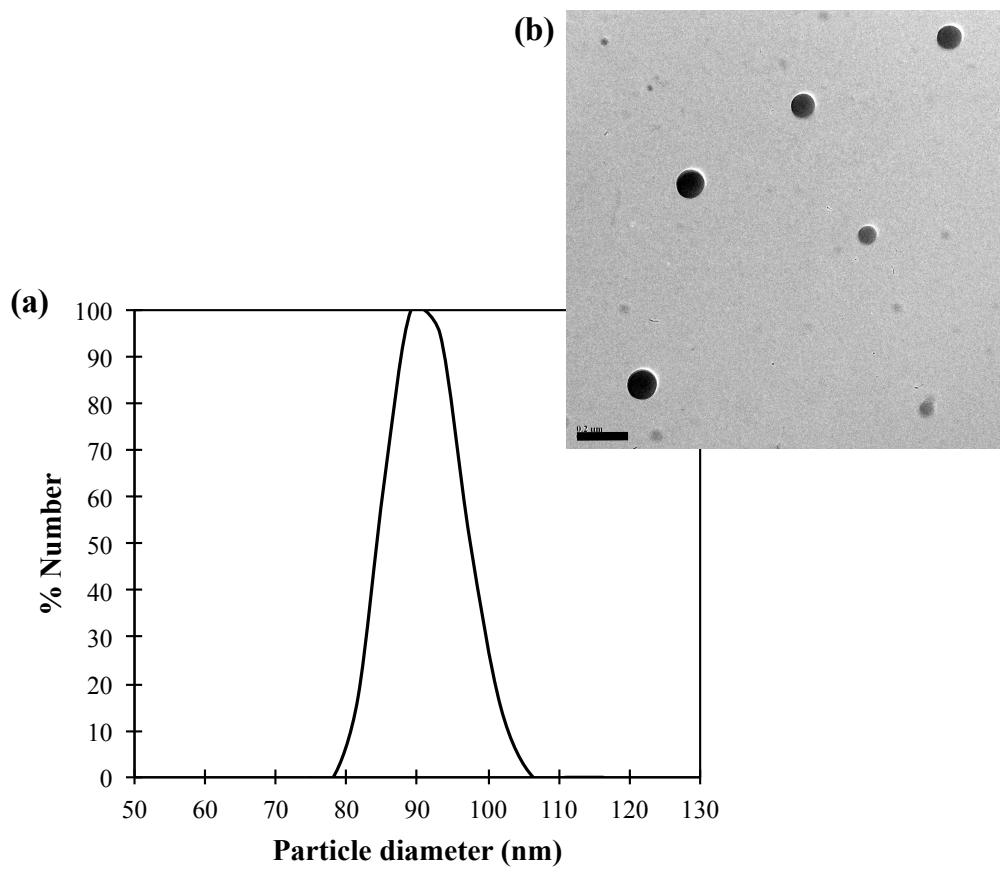


Figure 5.2: (a) DLS and (b) TEM results of large (89.1 nm) EC nanoparticles synthesis. The scale bar is 200 nm.

Figure 5.3 shows DLS and TEM results for EC nanoparticles synthesized from a starting solution containing 1.07 g/L of EC in isopropyl alcohol (one tenth of the concentration of the solution used to prepare 89.1 nm nanoparticles). Comparison of Figure 5.3 to Figure 5.2 shows that a more dilute starting solution leads to the formation of smaller EC nanoparticles during the anti-solvent step. Again, the EC nanoparticles are spherical in shape and not aggregated and essentially monodisperse, but their mean diameter is now 42 nm. These observations are in agreement with Jin *et al.* [41]. Using acetone

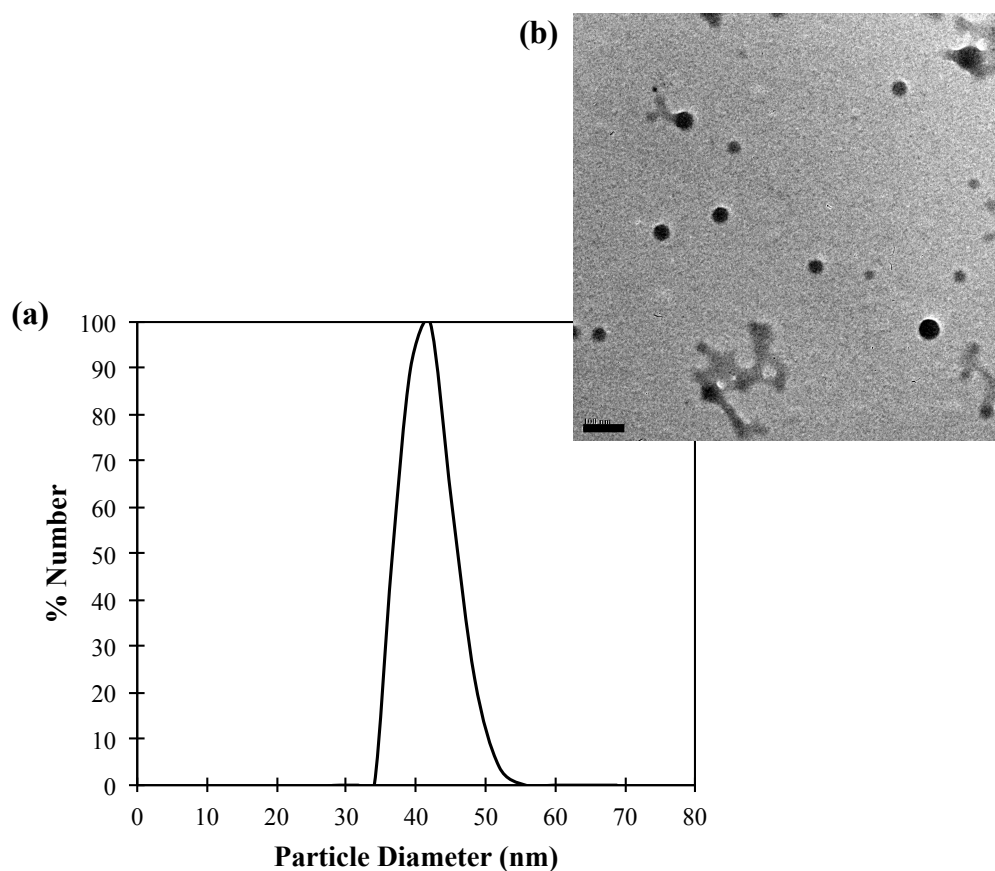


Figure 5.3: (a) DLS and (b) TEM results of small (42 nm) EC nanoparticles synthesis. The scale bar is 100 nm.

instead of iso-propyl alcohol as the solvent, these authors found that larger nanoparticles can be synthesized from EC solutions of higher initial concentration. At neutral pH, an electrostatic repulsive force was found to inhibit aggregation of EC nanoparticles, resulting

in a highly stable colloidal solution [41].

5.2 Dynamic Surface Tension (DST) Results

Experimental DST data for colloidal solutions containing varying concentrations of 89.1 nm EC nanoparticles are shown in Figure 5.4. The DST of nanoparticle-free solutions of isopropyl alcohol-water mixtures having the same alcohol content as the colloidal solutions tested are also plotted on the same figure. The greatest amount of isopropyl alcohol is found in the most concentrated EC nanoparticle solution: colloidal solutions containing 1.0 g/L of EC nanoparticles contain ~ 0.02 mol% isopropyl alcohol (see Appendix A). Such a concentration of isopropyl alcohol causes the surface tension to decrease from 72.06 ± 0.18 mN/m for pure Milli-Q water to 66 mN/m in 1800 seconds (see Figure 5.4 (h)) in agreement with water-isopropyl alcohol surface tension data reported in [65]. It is clear from Figure 5.4 (h) that the large surface tension reduction observed for the most concentrated solution of EC nanoparticles is due to nanoparticle adsorption at the air-liquid interface and not due to the presence of ~ 0.02 mol% isopropyl alcohol in the colloidal solution. Colloidal solutions of EC nanoparticle concentration less than 1.0 g/L were prepared by dilution and, for this reason, contain less than ~ 0.02 mol% isopropyl alcohol. The data shown in Figure 5.4 (a)-(g) rule out the presence of isopropyl alcohol as the reason for surface tension reduction in colloidal solutions of EC nanoparticles.

Jin *et al.* [41] have observed a similar surface tension reduction for colloidal solutions of EC nanoparticles as shown in Figure 5.4. They argued, however, that at neutral pH, electrostatic repulsion between the negatively-charged EC nanoparticles and the negatively-charged air-water interface prevents adsorption of the nanoparticles at the air-water interface. They suggested (but showed no direct evidence of it) that the surface tension of colloidal solutions of EC nanoparticles decreases as a result of adsorption of water-soluble impurities. In order to address this claim, 0.2 g EC was kept in contact with 10 mL milli-Q water for four days to extract any water soluble impurities that might affect the surface tension of colloidal solutions. The quantities of EC and water chosen for this test are such that any surface-active impurities would be present in the supernatant at a concentration equivalent to their concentration in a 2 wt.% EC solution. That is, at a concentration 20 times greater than their concentration in the most concentrated colloidal solution tested. Measurement of the surface tension of this supernatant yielded a value of ~ 65 mN/m at equilibrium, which is much greater than the equilibrium surface tensions realized in the presence of EC nanoparticles. This demonstrates that the surface tension reduction for colloidal solutions of EC nanoparticles shown in Figure 5.4 is not due to the

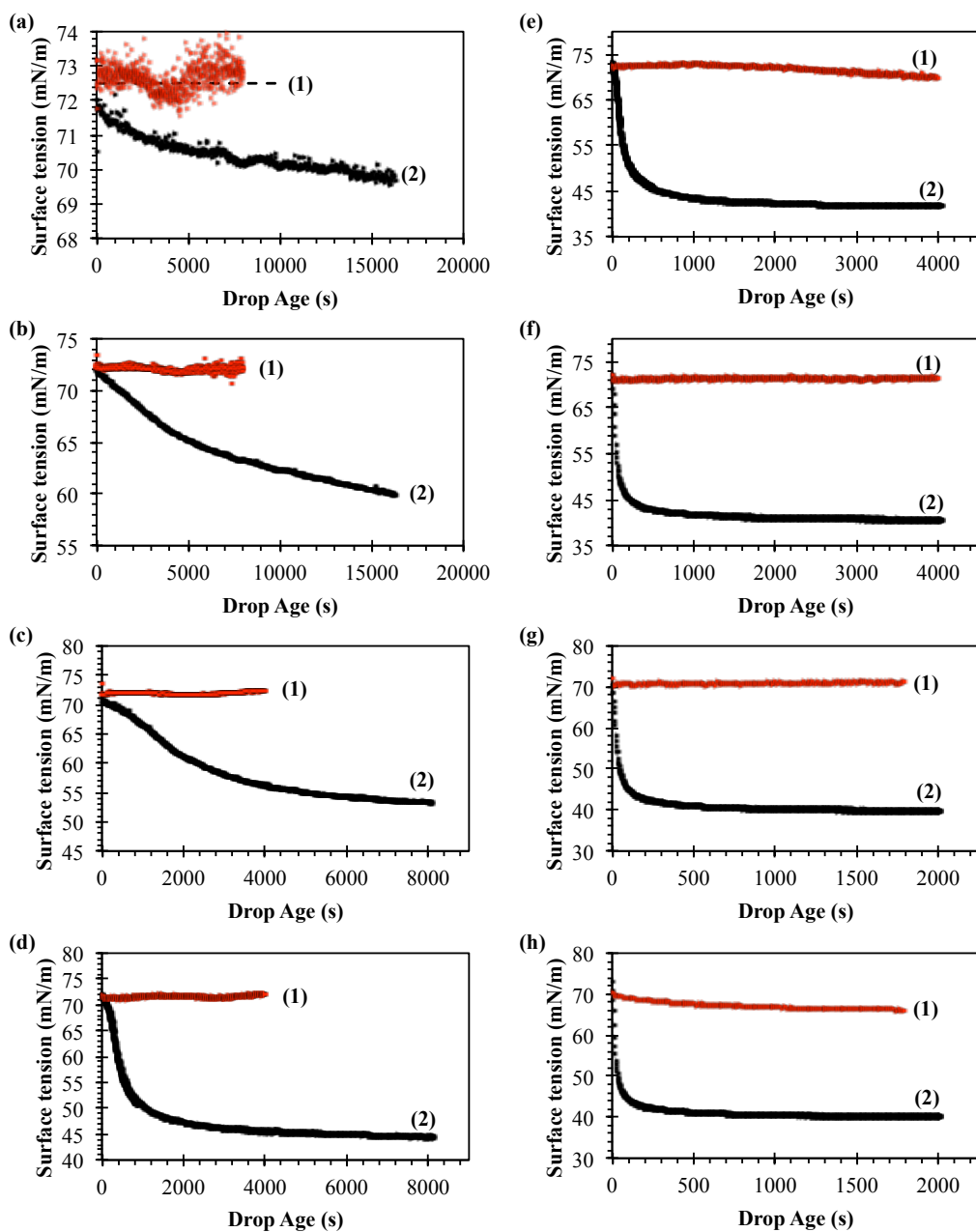


Figure 5.4: Dynamic surface tension (DST) of solutions containing (1) no nanoparticle and (2) 89.1 nm EC nanoparticles with concentration of (a) 0.05 g/L, (b) 0.075 g/L, (c) 0.1 g/L, (d) 0.2 g/L, (e) 0.4 g/L, (f) 0.6 g/L, (g) 0.8 g/L, and (h) 1.0 g/L.

presence of water-soluble impurities, but due to the adsorption of EC nanoparticles at the air-water interface. The fact that EC nanoparticle adsorption takes place at neutral pH, where electrostatic repulsion between the particles and the interface is well-established by zeta potential measurements [41], invites interesting hypotheses concerning the possible parallel action of long-range attractive hydrophobic forces [39].

DST data for all colloidal solutions of 89.1 nm EC nanoparticles are collected in Figure 5.5. A more rapid reduction of surface tension is observed with increasing bulk concentration of nanoparticles. For the lowest nanoparticle concentration of 0.05 g/L, the surface tension decreases only by 2 mN/m in almost ~ 4.5 hours, whereas the surface tension is reduced by ~ 32 mN/m in about 15 minutes when the nanoparticle concentration is 1.0 g/L. Use of a logarithmic time scale in Figure 5.5 enables the qualitative identification of three periods of time in the adsorption process, as suggested by Hua and Rosen [36]. Early in the adsorption process, the surface tension changes very gradually. This phase is called *induction phase* (phase *I*) [36]. During this period of time, which can be considered as a lag time, the surface properties are hardly affected by the presence of nanoparticles. As the number of adsorbed nanoparticles at the interface increases, the surface tension decreases dramatically until a plateau is first reached. This second phase is known as the *rapid fall phase* (phase *II*) [36]. DST data after the initial formation of the plateau correspond to the so-called *meso-equilibrium phase* (phase *III*) [36]. The extent of each of these regions in a DST graph depends on the bulk concentration of nanoparticles. At a bulk nanoparticle concentration of 0.2 g/L, for instance, phase *II* sets in after about one hundred seconds elapsed from the time the drop was formed. On the contrary, phase *II* sets in much earlier when the EC nanoparticle concentration is 0.6 g/L.

Hua and Rosen [36] have proposed the following empirical equation to fit the DST data:

$$\gamma - \gamma_m = \frac{\gamma_0 - \gamma_m}{1 + (t/t^*)^n} \quad (5.1)$$

where γ_0 and γ_m are the surface tension of pure solvent and the meso-equilibrium surface tension, respectively, and t^* and n are constants. Fitting of this equation to the DST data of 89.1 nm particles is shown in Figure 5.6. The best-fit values of the parameters; γ_m , t^* , and n ; are collected in Table 5.1.

As shown in this table, the meso-equilibrium surface tension decreases with increasing bulk concentration of EC nanoparticles, but levels off at ~ 40 mN/m for EC nanoparticle concentrations greater than ~ 0.5 g/L. It must be kept in mind that the empirical model of Hua and Rosen [36] can be used to summarize, compare and correlate DST data, but cannot explain the observed behavior. For example, the meso-equilibrium surface tension

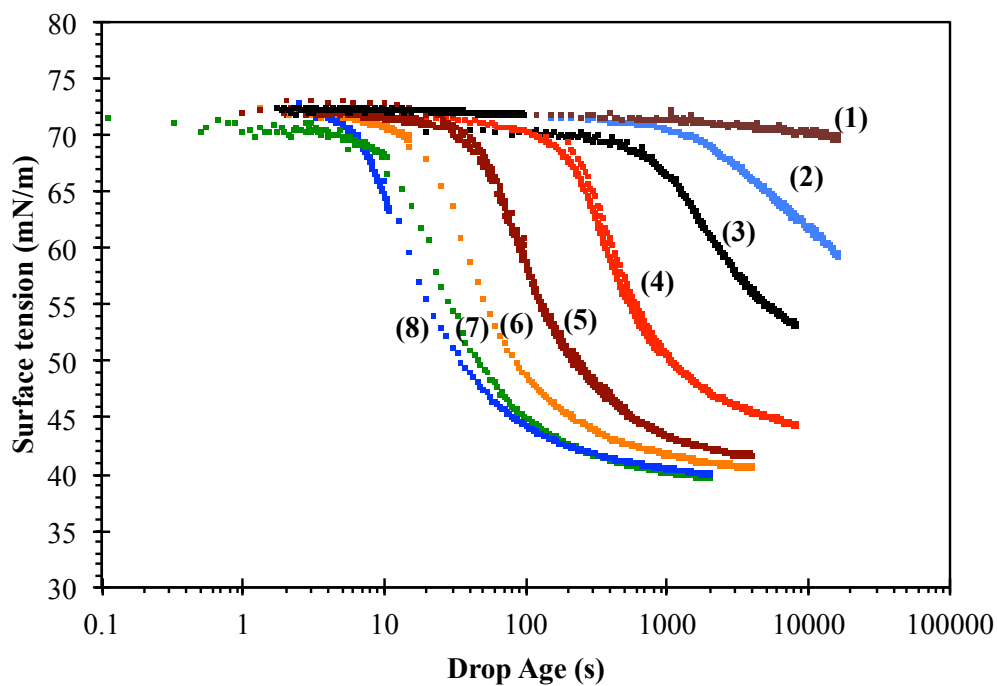


Figure 5.5: Dynamic surface tension (DST) measurements of 89.1 nm EC nanoparticles solutions on a log scale plot at concentrations (1) 0.05 g/L, (2) 0.075 g/L, (3) 0.1 g/L, (4) 0.2 g/L, (5) 0.4 g/L, (6) 0.6 g/L, (7) 0.8 g/L, and (8) 1.0 g/L.

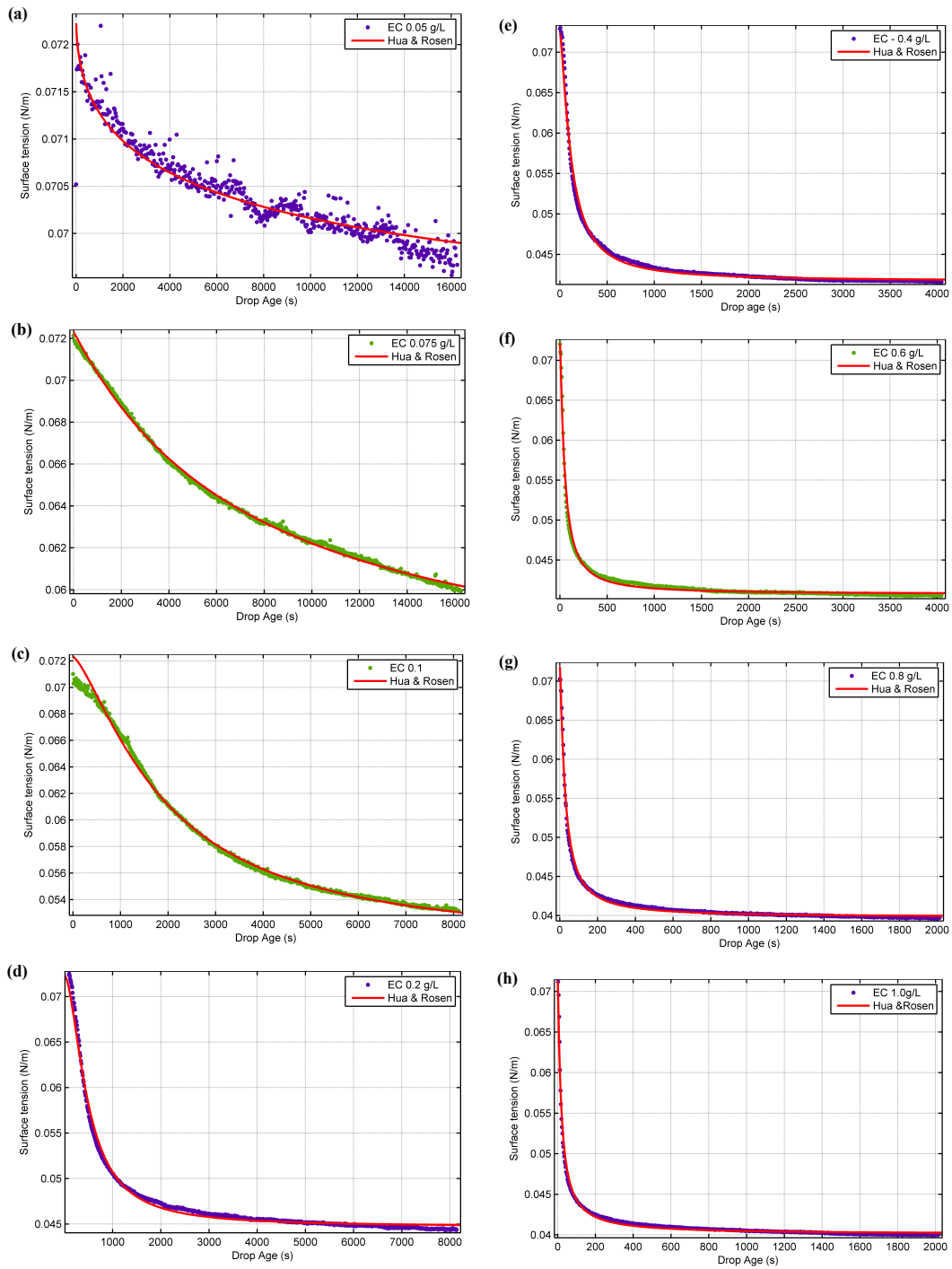


Figure 5.6: Fitting Hua and Rosen's empirical equation (Eq. (5.1)) on the DST data of colloidal solution of 89.1 nm EC nanoparticles at different concentrations.

Table 5.1: Fitting parameters of Hua and Rosen’s empirical equation (Eq. (5.1)) at different concentrations of 89.1 nm EC nanoparticle colloidal solutions.

Mass con. (g/L)	Large EC nanoparticles				
	$C \times 10^7$ (mol/m ³)	$\gamma_{meso-eq.}$ (mN/m)	t^* (s)	n	R^2
0.05	1.91	68.02	10030	0.500	0.9124
0.075	2.86	54.77	7445	1.033	0.9981
0.1	3.82	50.35	1950	1.382	0.9949
0.2	7.63	44.71	484.3	1.77	0.9917
0.4	15.26	41.70	118.4	1.431	0.9916
0.6	22.90	40.72	48.88	1.244	0.9871
0.8	30.53	39.79	27.45	1.23	0.9917
1.0	38.16	40.09	18.26	1.11	0.9859

is a useful indicator but does not represent the equilibrium surface tension (i.e., when $t \rightarrow \infty$).

DST data for all colloidal solutions of 42-nm EC nanoparticles are collected in Figure 5.7. As shown in this figure, the dependence of surface tension on bulk nanoparticle concentration is similar to the one observed for 89.1 nm particles. The empirical description of Hua and Rosen applies to the DST data of colloidal solutions containing the smaller EC nanoparticles (i.e., 42 nm) as well and a similar value of the meso-equilibrium surface tension (i.e., ~ 40 mN/m) is found (see Figure 5.7 (b)).

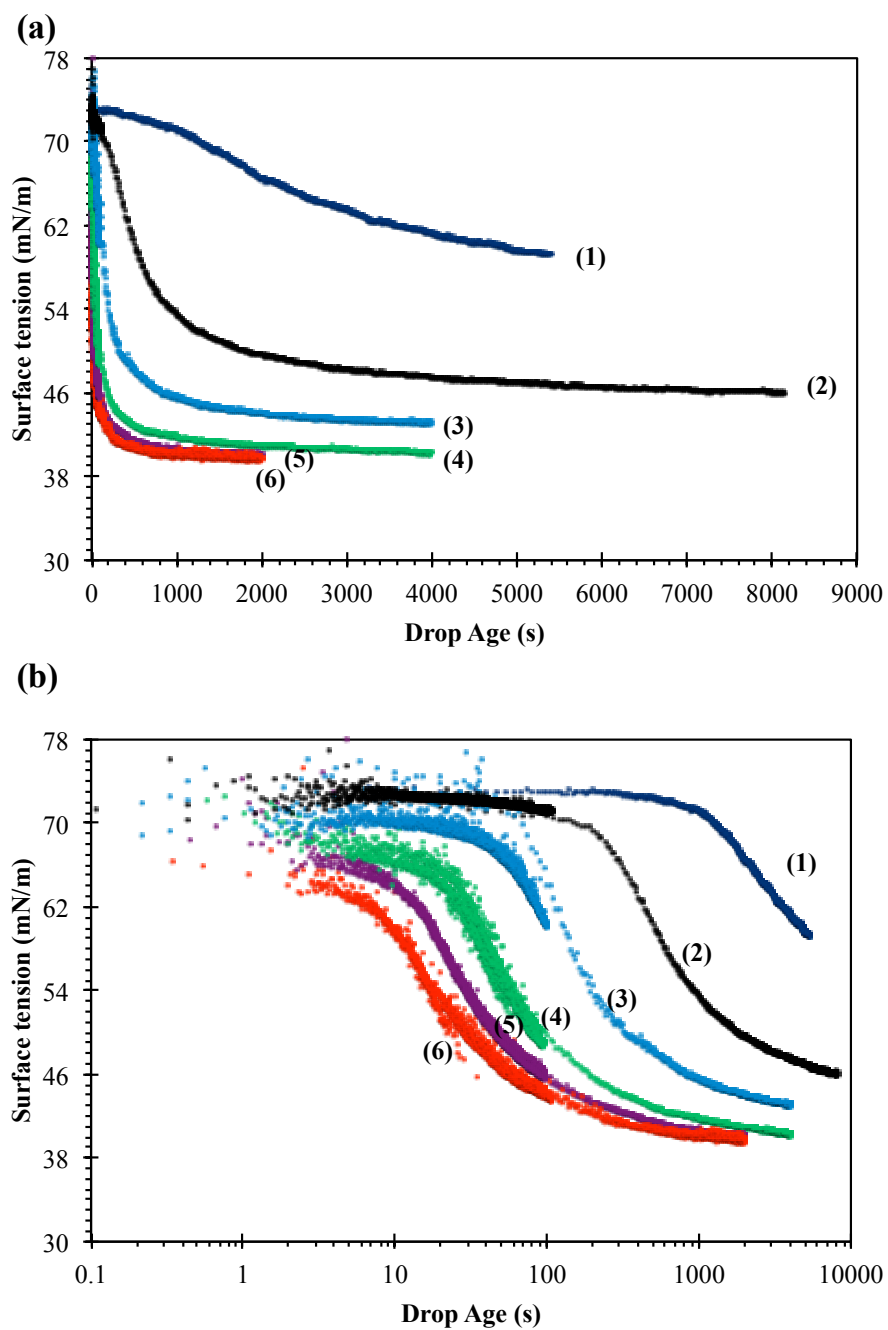


Figure 5.7: Dynamic surface tension (DST) measurements of 42 nm EC nanoparticles solutions on a (a) linear (b) log scale plot at concentrations (1) 0.1 g/L, (2) 0.2 g/L, (3) 0.4 g/L, (4) 0.6 g/L, (5) 0.8 g/L, and (6) 1.0 g/L.

Chapter 6

Discussion

6.1 Failure of Reversible Adsorption Model

An attempt to analyze DST data from colloidal solutions of EC nanoparticles in the context of the Ward and Tordai model [70] is not successful. According to that model, one expects Eq. (2.40) to apply during the early stages of adsorption. An estimate of the nanoparticle diffusion coefficient - hereafter denoted as D_0 - may be readily obtained from the slope of a plot of early-time DST data against $t^{0.5}$, given by:

$$\left. \frac{d\gamma}{dt^{0.5}} \right|_{t \rightarrow 0} = -2RTC_0 \left(\frac{D_0}{\pi} \right)^{0.5} \quad (6.1)$$

As many D_0 estimates as colloidal solutions of different bulk nanoparticle concentration may be obtained. One expects all estimates of D_0 for nanoparticles of the same size to be equal to the value predicted by the Stokes-Einstein equation. Fits of Eq. (2.40) to early-time DST data of colloidal solutions of both 89.1 nm and 42 nm EC nanoparticles are shown in Appendix B and the computed D_0 values are summarized in Table 6.1. The failure of the Ward and Tordai model is clearly reflected in Table 6.1, which shows D_0 values at odds with expectation in more than one ways. Firstly, D_0 values are many orders of magnitude greater than the value predicted by the Stokes-Einstein equation and of the same order of magnitude as gas phase diffusivities [18] - a physically unrealistic result that contradicts fluorescent microscopy observations of the diffusive motion of nanoparticles in a liquid environment [27]. Secondly, D_0 values for larger nanoparticles are greater than D_0 values for smaller nanoparticles - a result contrary to theoretical expectation (e.g., Stokes-Einstein equation).

The long-time asymptotic result, Eq. (2.37), may also be used to analyze long-time DST data in the context of the Ward and Tordai theory. Recall that this approach was followed by Kutuzov *et al.* [44] and Ferdous *et al.* [31] in recent DST-based investigations of the adsorption of nanoparticles at liquid-liquid interfaces. To use Eq. (2.37), Γ_{eq} is calculated by assuming a dense hexagonal packing of the particles at the interface (i.e., $\theta_{\max}=0.91$):

$$\left. \begin{aligned} \theta_{\max} &= \frac{\text{area covered by adsorbed particles}}{\text{total area of interface}} \\ \Gamma_{eq} &= \frac{\text{moles of particles}}{\text{total area of interface}} \end{aligned} \right\} \Rightarrow \frac{\Gamma_{eq}}{\theta_{\max}} = \frac{1}{N_A \pi r^2} \quad (6.2)$$

According to Eq. (2.37), an estimate of the nanoparticle diffusion coefficient – hereafter denoted as D_∞ – may be readily obtained from the slope $d\gamma/dt^{-0.5}$ of a plot of long-time DST data against $t^{-0.5}$. D_∞ estimates are also given in Table 6.1.

Table 6.1: Estimates of the diffusion coefficient obtained from early- and long-time DST data via Eq. (2.40) and Eq. (2.37), respectively, for large (89.1 nm) and small (42 nm) EC nanoparticles. Values in brackets are estimates from Eq. (2.7).

Large EC nanoparticles		$(D=4.76 \times 10^{-12} \text{ m}^2/\text{s})$		Small EC nanoparticles		$(D=1.02 \times 10^{-11} \text{ m}^2/\text{s})$	
$C \times 10^7 \text{ (mol/m}^3)$	$D_0 \times 10^3 \text{ (m}^2/\text{s)}$	$D_\infty \times 10^{19} \text{ (m}^2/\text{s)}$	$C \times 10^6 \text{ (mol/m}^3)$	$D_0 \times 10^4 \text{ (m}^2/\text{s)}$	$D_\infty \times 10^{18} \text{ (m}^2/\text{s)}$		
1.91	0.98	531					
2.86	10.1	2.48					
3.82	3.79	2.94	3.75	1.20	0.89		
7.63	9.37	6.33	7.51	0.94	1.80		
15.26	9.96	8.75	15.02	1.47	1.39		
22.90	16.2	7.60	22.53	8.51	2.46		
30.53	15.5	7.50	30.04	10.6	2.00		
38.16	17.4	5.84	37.55	15.1	1.77		

In previous DST-based studies of nanoparticle adsorption at liquid-liquid interfaces ([44, 31]), D_∞ estimates were shown to decrease with increasing bulk concentration of nanoparticles, a trend not present in the data of Table 6.1. As in previous studies [44, 31], $D_\infty < D$ for all bulk nanoparticle concentrations. In the context of reversible adsorption models of the kinds reviewed in Section 2.3.1, $D_\infty < D$ is interpreted as evidence of an energy barrier to adsorption (see Figure 2.8), the magnitude of which could be calculated as [44]:

$$\Delta E_p = -\ln\left(\frac{D_{eff}}{D}\right) \quad (6.3)$$

where D is the diffusion coefficient predicted by the Stokes-Einstein theory and D_{eff} is the calculated adsorption energy from long-time DST data analysis (i.e., D_∞). Using the values for D_∞ , reported in Table 6.1, the energy barrier to adsorption of 89.1 nm and 42 nm EC nanoparticles is estimated as $15.45 \pm 1.7k_B T$ and $15.64 \pm 0.36k_B T$, respectively. Kutuzov *et al.* [44] and Ferdous *et al.* [31] have reported estimates of an energy barrier to adsorption $\sim 10k_B T$ for ligand-stabilized Au and CdSe nanoparticles in the size range 2 to 6 nm. Kutuzov *et al.* [44] have asserted that “...at the late stage of adsorption, the most probable mechanism to create a free space at the oil/water interface is by desorption of a particle rather than lateral diffusion and reordering of the nanoparticle interfacial self-assembly”. Considering that the desorption energy is proportional to the square of particle radius, the assertion of Kutuzov *et al.* [44] seems inconsistent with the above estimates of the adsorption barrier for nanoparticles of different size (including the ones studied here). In fact, a re-examination of their DST data, as well as those of Ferdous *et al.* [31], in light of Eq. (2.42) shows that the adsorption energy of some of the nanoparticles studied is $\sim 40k_B T$. Such particles would be expected to adsorb irreversibly [26, 38], casting further doubt on the assertion of Kutuzov *et al.* [44] regarding the physical origin of kinetic limitations.

An explicit allowance for a barrier to adsorption is not made in the theory of Ward and Tordai – the presence of a barrier to adsorption is *inferred* via Eq. (6.3). Nevertheless, due to the presence of adsorbed particles, an energy barrier should be expected to emerge as the coverage of the interface increases [44]. RSA models account explicitly for a steric barrier to adsorption in terms of the blocking function. Such a barrier is a standard feature of RSA models, even for the case of non-interacting, hard-sphere particles [5, 67]. Repulsive interactions due to this barrier are exactly accounted for in the particle continuity equation. Particle-particle and particle-surface DLVO interactions (see Figure 2.12) are *additional* to repulsive interactions due to the steric barrier, as shown in Figure 6.1 [1].

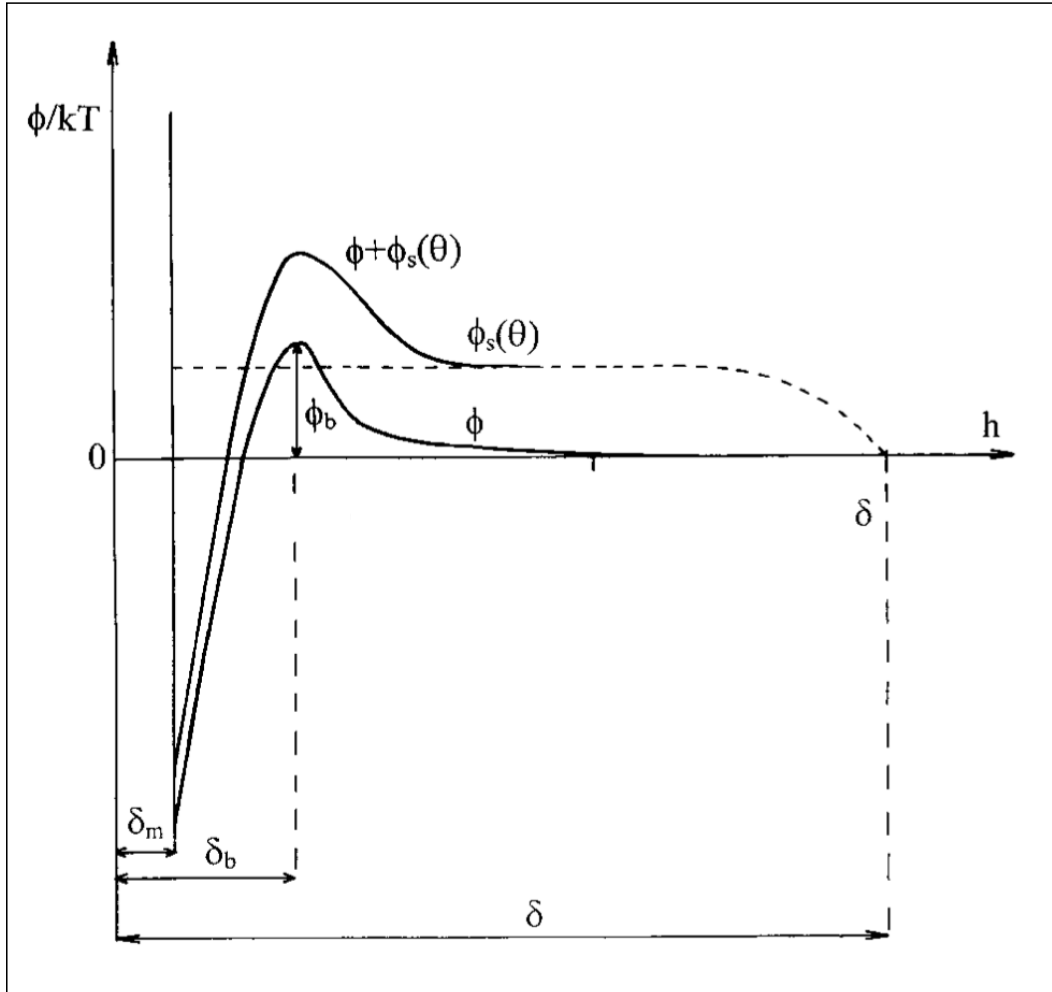


Figure 6.1: The effect of steric barrier on a schematic energy profile (ϕ) in the subsurface (along direction h) [1]. ϕ_b and ϕ_s represent the energy barrier (at the distance of δ_b from the interface) and the steric energy barrier, respectively. Also, δ_m and δ denote the primary minimum distance from the interface and the adsorption layer thickness, respectively.

6.2 Adsorption Energy Calculation

During the early stages of adsorption surface coverage is low and the rate of nanoparticle attachment at the interface is controlled by the rate of diffusion of nanoparticles from the bulk. For irreversible adsorption, Eq. (3.10), was derived in this work. Similar to Eq. (2.40), Eq. (3.10) also shows that surface tension is linear with $t^{0.5}$, as would be expected for any process governed by Fickian diffusion. Unlike Eq. (2.40); however, the novel Eq. (3.10) explicitly accounts for the energy of adsorption of a single particle. Since the nanoparticle diffusion coefficient can be reliably estimated using Eq. (2.7) and DLS measurements, the validity of Eq. (2.40) can be tested using DST data. The test consists of comparing ΔE , calculated from the slope of linear regressions of early-time DST data against $t^{0.5}$ (see Appendix B) and hereafter referred to as ΔE_{dyn} , to ΔE computed from Eq. (2.42) and hereafter referred to as ΔE_{eq} .

As noted earlier, use of Eq. (2.42) requires knowledge of (i) the equilibrium (steady-state) surface tension, γ_{eq} , and (ii) the equilibrium (steady-state) coverage θ_{max} . For irreversible adsorption, and only if it can be assumed that the bulk has an infinite supply of nanoparticles, such that the bulk concentration is not significantly affected by the attachment of nanoparticles at the interface, one expects (a) γ_{eq} to be obtained from the intercept of plots of long-time DST data against $t^{-0.5}$ (see Appendix B), as per Eq. (3.8), and (b) γ_{eq} and θ_{max} to be independent of bulk concentration. Values of γ_{eq} are plotted against bulk concentration in Figure 6.2. It is immediately noted that for sufficiently high values of the bulk concentration, adsorption of EC nanoparticles of either size results in the same equilibrium (steady-state) value of surface tension ($\sim 39.00 \pm 0.5$ mN/m), in good agreement with a previous study [41]. This is consistent with expectation for irreversible adsorption from a bulk liquid phase of constant concentration. Maximum (jamming) coverage of the interface ($\theta_{max} \cong 0.91$) may be expected under these conditions, as assumed by Du *et al.* [26] and predicted by the simulations of Isa *et al.* [38]. At the same time, analysis of DST data for colloidal solutions containing less than 0.4 g/L of EC nanoparticles leads to γ_{eq} lower than $\sim 39.00 \pm 0.5$ mN/m (see Figure 6.2). Given the size of pendant drops used in this research, the bulk nanoparticle concentration that is *just enough* to completely cover ($\theta_{max} \cong 0.91$) the interface is of the order of 0.1 g/L (see Appendix D). It may thus be concluded that the bulk of pendant drops formed from colloidal solutions containing less than 0.4 g/L of EC nanoparticles is significantly depleted of nanoparticles as a result of adsorption.

Values of ΔE_{dyn} and ΔE_{eq} from colloidal solutions of 89.1 nm and 42 nm EC nanoparticles are collected in Table 6.2 and Table 6.3, respectively. All values of ΔE_{eq} were computed according to Eq. (2.42) using the values of γ_{eq} plotted in Figure 6.2 and ($\theta_{max} = 0.91$)

Table 6.2: Adsorption energy of 89.1 nm EC nanoparticles at the air-water interface.

C (g/L)	C × 10 ⁷ (mol/m ³)	$\Delta E_{eq}(k_B T)$	$\Delta E_{dyn}(k_B T)$
0.05	1.91	0.56×10^4	1.4×10^4
0.075	2.86	3.6×10^4	4.5×10^4
0.1	3.82	4.8×10^4	2.7×10^4
0.2	7.63	5.2×10^4	4.3×10^4
0.4	15.26	5.5×10^4	4.4×10^4
0.6	22.90	5.6×10^4	5.6×10^4
0.8	30.53	5.7×10^4	5.5×10^4
1.0	38.16	5.7×10^4	5.8×10^4
		Ave.: $5.6 \pm 0.1 \times 10^4$	Ave.: $5.3 \pm 0.6 \times 10^4$

Table 6.3: Adsorption energy of 42 nm EC nanoparticles at the air-water interface.

C (g/L)	C × 10 ⁶ (mol/m ³)	$\Delta E_{eq}(k_B T)$	$\Delta E_{dyn}(k_B T)$
0.1	3.75	0.94×10^4	0.34×10^4
0.2	7.51	1.1×10^4	0.30×10^4
0.4	15.0	1.2×10^4	0.38×10^4
0.6	22.5	1.3×10^4	0.91×10^4
0.8	30.0	1.3×10^4	1.02×10^4
1.0	37.5	1.3×10^4	1.2×10^4
		Ave.: $1.3 \pm 0.01 \times 10^4$	Ave.: $1.1 \pm 0.2 \times 10^4$

regardless of concentration. Average values of ΔE_{dyn} and ΔE_{eq} are compared, where averaging is limited to the results from colloidal solutions resulting in identical equilibrium surface tension for the reasons stated above. ΔE_{dyn} is found to agree remarkably well with ΔE_{eq} . It should be noted that the estimate ΔE_{dyn} is obtained with no reference to θ_{max} and for this reason it can be used to test the assumption $\theta_{max} \cong 0.91$ against experimental data. This test is discussed next.

6.3 Dynamics of Surface Coverage

Knowledge of the adsorption energy, ΔE , makes possible the calculation of *transient* surface coverage, $\theta(t)$, directly from DST data, $\gamma(t)$, by means of Eq. (3.9). The values obtained for $\theta(t)$ are used in Eq. (2.52) to calculate the maximum surface coverage θ_{max} as the intercept of a linear regression of $\theta(t)$ against $t^{-0.5}$ (see Appendix C). The results of this

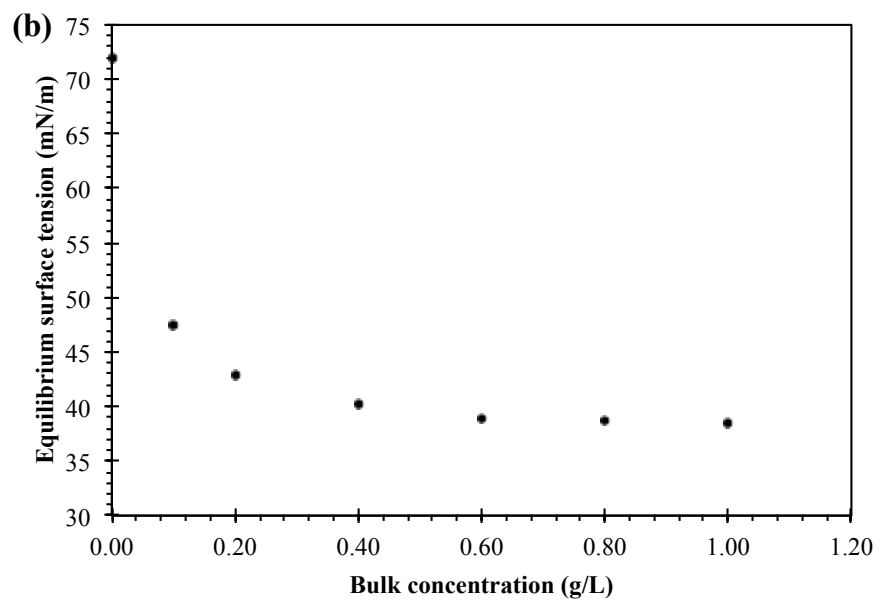
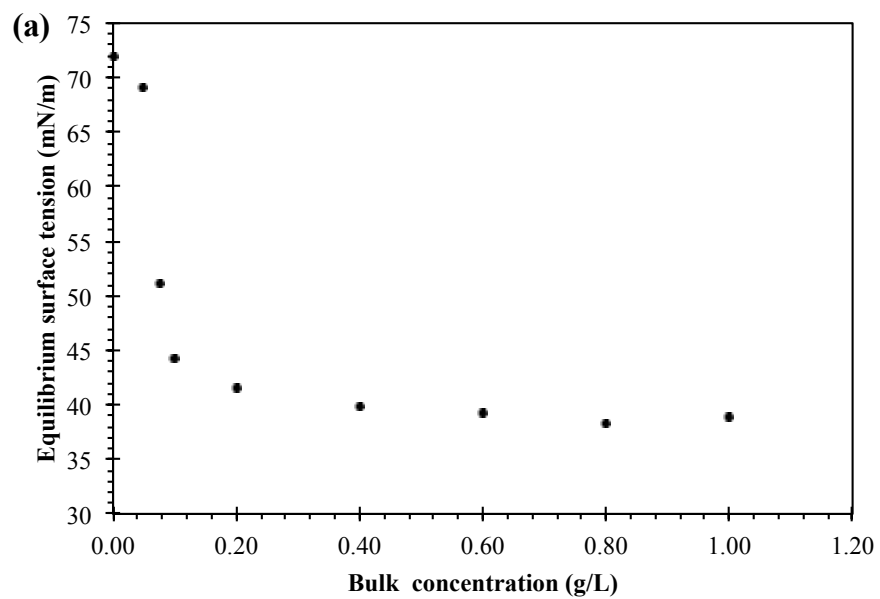


Figure 6.2: Equilibrium surface tension as a function of the bulk concentration of colloidal solutions of (a) 89.1 nm and (b) 42 nm EC nanoparticles.

analysis for DST data from different colloidal solutions of 89.1 nm and 42 nm EC nanoparticles are shown in Figure 6.3. The results shown in Figure 6.3 support the conclusion that adsorption-mediated self-assembly of EC nanoparticles at the air-water interface results in the formation of a dense liquid-like layer corresponding to $\theta_{\max} \cong 0.91$, the coverage predicted for a hexagonal arrangement (see Figure 3.1). The result $\theta_{\max} \cong 0.91$ agrees with the prediction of Isa *et al.*'s [38] from atomistic simulations (see Figure 2.11). It must be noted that the maximum surface coverage predicted by RSA under the assumption of *localized irreversible adsorption* – an assumption valid for adsorption on solid-fluid interfaces – is ~ 0.5 [67]. The much higher coverage observed and predicted for fluid interfaces implies that adsorbed nanoparticle layers are liquid-like, in the sense that adsorbed particle mobility is not lost at high coverage. In fact, fluorescence recovery after photo-bleaching (FRAP) measurements [47] show that adsorbed nanoparticles in a densely covered liquid-liquid interface diffuse with a diffusion coefficient which has a value four orders of magnitude smaller than its value in bulk. Values of θ_{\max} smaller than ~ 0.91 (see Figure 6.3) are associated with the less concentrated colloidal solutions, for which the assumption of constant bulk concentration throughout the adsorption process is likely violated. Indeed, the deviation from $\theta_{\max} \cong 0.91$ increases with decreasing bulk concentration. For instance, the maximum of coverage is only ~ 0.61 when the bulk concentration of 89.1 nm EC nanoparticles is 0.075 g/L.

6.4 Adsorption Kinetics

In the context of generalized RSA theory, irreversible adsorption kinetics is unequivocally characterized in terms of the adsorption constant and maximum (jamming) coverage. As discussed in Chapter 2, the adsorption rate is controlled entirely by the rate of diffusion of species from the bulk phase to the interface during the early stages of adsorption when interface coverage is low. As the interface coverage increases, the adsorbed particles hinder adsorbing particles to an ever increasing extent. This blocking effect is tantamount to a steric barrier to adsorption. As a result, the rate of adsorption ceases to be controlled by the rate of particle diffusion from the bulk to the interface. Instead, the adsorption constant, k_a (see Eq. (2.48)) becomes a complicated function of diffusion and the interaction energy of particles. In order to calculate the adsorption constant, long-time DST data are analyzed in terms of Eq. (3.8). From knowledge of adsorption energy, particle radius, and bulk concentration one can calculate K_l from the slope $d\gamma/dt^{-0.5}$ (see Appendix C). This enables the calculation of dimensionless adsorption constant, \bar{k}_a , from Eq. (2.53) and adsorption constant, k_a , from Eq. (2.54). These calculations are summarized in Table 6.4. Average

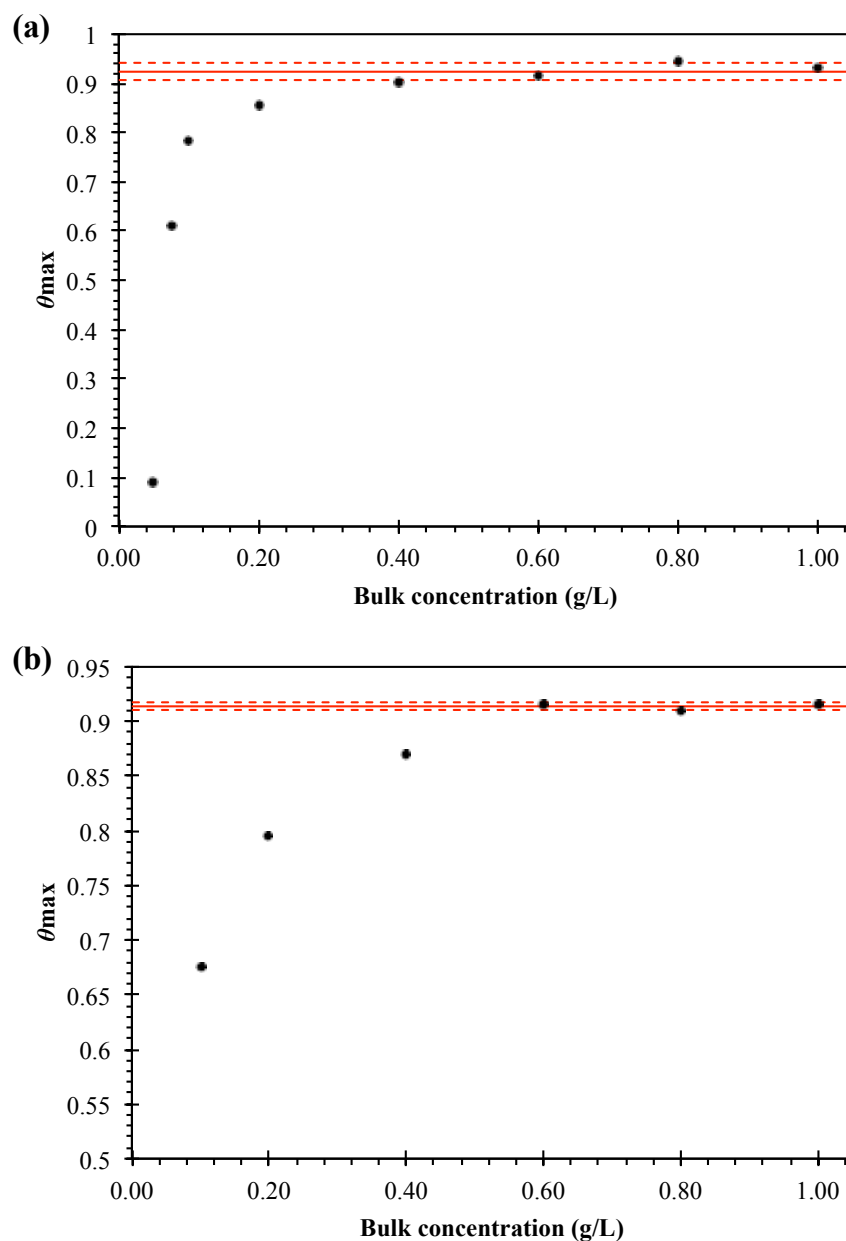


Figure 6.3: Maximum air-water interface coverage by EC nanoparticles at different bulk concentrations: (a) 89.1 nm EC nanoparticles (lines indicate $\theta_{\max} = 0.92 \pm 0.02$) and (b) 42 nm EC nanoparticles (lines indicate $\theta_{\max} = 0.91 \pm 0.003$). The average values for θ_{\max} are obtained from the most concentrated solutions (i.e, the last four concentrations for the large and the last three concentrations for the small EC nanoparticles).

Table 6.4: Calculated dimensionless adsorption constant, \bar{k}_a , and adsorption constant, k_a from Eq. (2.53) and Eq. (2.54), respectively.

C (g/L)	89.1 nm EC nanoparticles		42 nm EC nanoparticles	
	\bar{k}_a	k_a (m/s)	\bar{k}_a	k_a (m/s)
0.05	15.9	5.42×10^{-8}		
0.075	17.0	8.69×10^{-8}		
0.1	53.9	3.67×10^{-7}	2.67	1.79×10^{-7}
0.2	152	2.07×10^{-6}	8.77	1.18×10^{-6}
0.4	246	6.72×10^{-6}	8.90	2.39×10^{-6}
0.6	224	9.17×10^{-6}	17.5	7.06×10^{-6}
0.8	242	1.32×10^{-5}	18.5	9.93×10^{-6}
1.0	181	1.23×10^{-5}	13.3	8.94×10^{-6}
Ave.:	230 ± 30	$1.03 \pm 0.3 \times 10^{-5}$	17 ± 3	$8.64 \pm 1.4 \times 10^{-6}$

values of \bar{k}_a and k_a reported in Table 6.4 are based on the DST data corresponding to $\theta_{\max} \cong 0.91$ (i.e., excluding the more dilute colloidal solutions).

It has been shown [67] that as $\bar{k}_a \rightarrow \infty$, the surface coverage over the entire time can be approximated as:

$$\begin{aligned}
 \theta &= 2\sqrt{\pi} \left(\frac{t}{t_c} \right)^{0.5} && \text{for } \frac{t}{t_c} \leq \left(\frac{\theta_{\max}}{4\pi} \right) \\
 \theta &= \theta_{\max} && \text{for } \frac{t}{t_c} > \left(\frac{\theta_{\max}}{4\pi} \right)
 \end{aligned} \tag{6.4}$$

where t_c is a characteristic adsorption time defined as $1/(\pi r^2 C_0)^2 D$ and C_0 is the particle number concentration. Eq. (6.4) states that the entire adsorption process is controlled by the diffusion of nanoparticles from the bulk to the interface and that blocking effects are negligible except for $\theta = \theta_{\max}$ [67]. As shown in Figure 6.4, Eq. (6.4) is a reasonable approximation when $\bar{k}_a > 100$. Data from experiments yielding $\theta_{\max} \cong 0.91$ are plotted in the manner suggested by Eq. (6.4) in Figure 6.5. Data from colloidal solutions of different bulk concentrations are collapsed onto a single curve, as suggested by theory. Eq. (6.4) is a better approximation of the behavior of 89.2 nm EC nanoparticles, as expected from the higher value of \bar{k}_a . Notwithstanding, significant deviations from Eq. (6.4) even in the

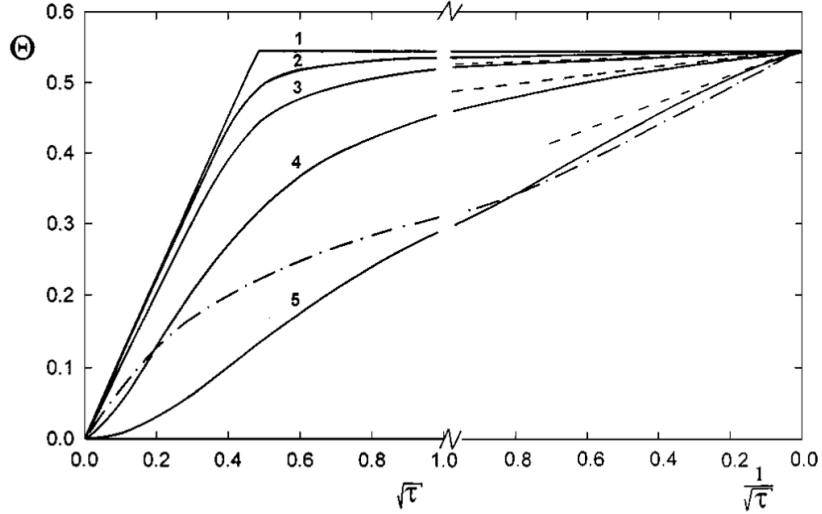


Figure 6.4: Surface coverage over entire time obtained from numerical modelling characterizing irreversible adsorption with $\theta_{\max} = 0.547$, corresponding to the maximum coverage for solid-fluid interfaces at (1) $\bar{k} = \infty$, (2) $\bar{k} = 1000$, (3) $\bar{k} = 100$, (4) $\bar{k} = 10$, and (5) $\bar{k} = 1$. The dashed lines represent the results of applying Eq. (2.52) and $\tau \equiv t/t_c$ [1].

case of 89.2 nm EC nanoparticles affirm the role played by a steric barrier during the later stages of adsorption.

Insight into the magnitude of a barrier to adsorption attributable to particle-interface interactions (see Figure 2.12), ϕ_b , is afforded by further analysis of the values of the adsorption constant, k_a . Assuming a parabolic energy distribution one has [67]:

$$k_a \cong \frac{D}{r} \left(\frac{\phi_b}{\pi k_B T} \right)^{0.5} \exp\left(- \frac{\phi_b}{k_B T} \right) \quad (6.5)$$

Whereas for a strongly asymmetric barrier the following result is derived [67]:

$$k_a = \frac{D}{r} \left(\frac{\phi_b}{k_B T} \right) \exp\left(- \frac{\phi_b}{k_B T} \right) \quad (6.6)$$

One obtains $\phi_b = 2.3 k_B T$ from Eq. (6.5) and $\phi_b = 3.62 k_B T$ from Eq. (6.6) for 89.1 nm EC nanoparticles using the data of Table 6.4. Similarly, $\phi_b = 4.3 k_B T$ from Eq. (6.5) and $\phi_b = 5.78 k_B T$ from Eq. (6.6) for 42 nm EC nanoparticles. All of these estimates are of the order of few $k_B T$ and hence, several orders of magnitude smaller than the adsorption

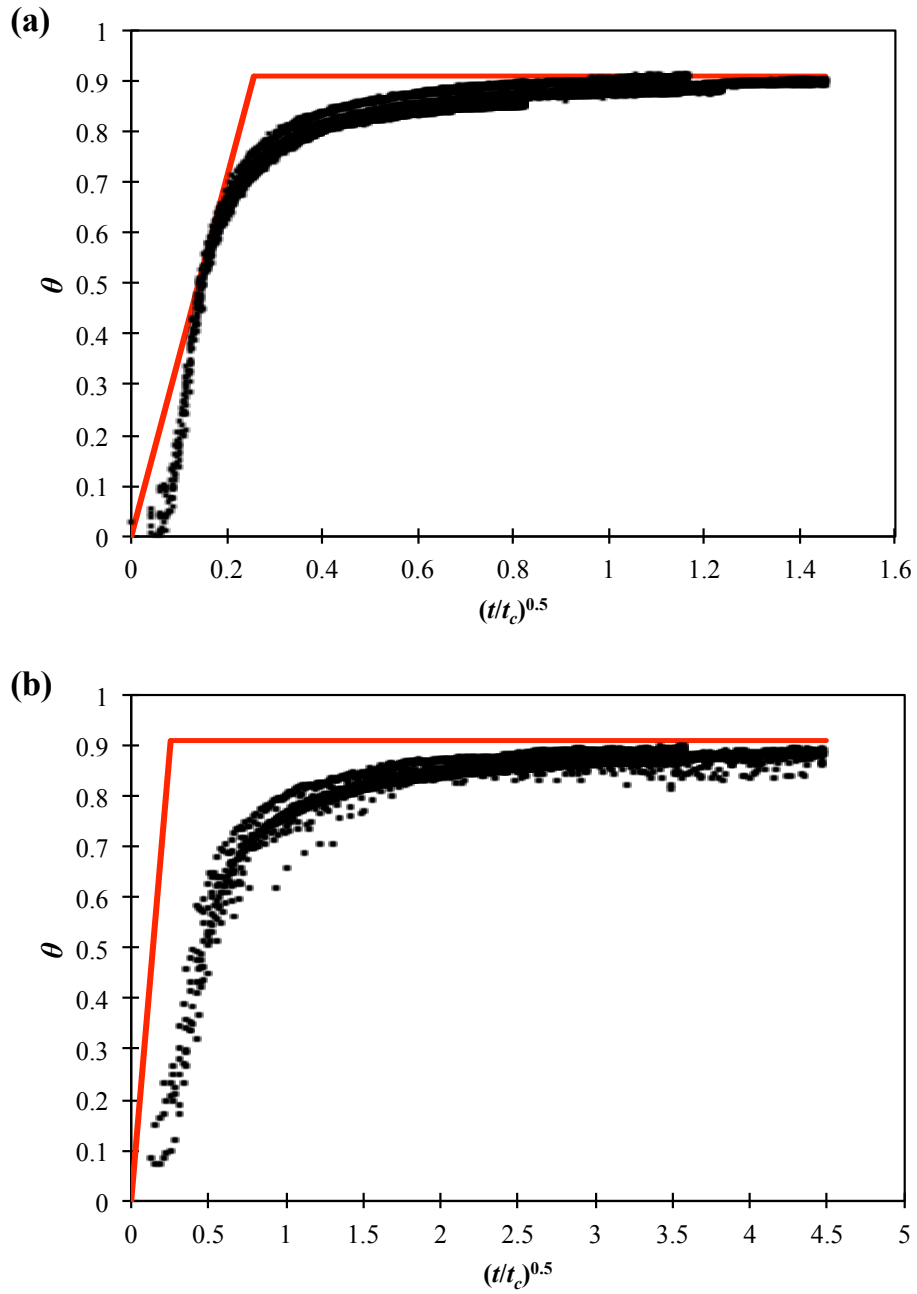


Figure 6.5: Surface coverage dynamics (a) $\bar{k}_a \cong 200$ (the case of 89.1 nm EC nanoparticles) (b) $\bar{k}_a \cong 10$ (the case of 42 nm EC nanoparticles). Markers are experimental data for large (a) and small (b) EC nanoparticles, respectively, and lines correspond to Eq. (6.4)

energy (i.e., ϕ_m in Figure 2.12). The fact that DLVO particle-interface interactions do not result in a significant barrier to adsorption considering that, at neutral pH, the air-water interface and EC nanoparticles are both negatively charged, is worthy of further study.

Chapter 7

Conclusions and Recommendations

7.1 Conclusions

This work examined the potential of dynamic surface tension (DST) measurements to characterize quantitatively adsorption-mediated self-assembly of nanoparticles at fluid interfaces. To this end, this work (i) critically assessed the applicability of adsorption models extensively used to interpret DST data of surfactant solutions, (ii) extended and validated RSA model with thermodynamics arguments suitable for nanoparticles, and (iii) applied the models and experimental techniques to ethylcellulose (EC) nanoparticles, a material with remarkable ability to stabilize foams and emulsions. The results of this work advance the understanding of parameters that control the self-assembly, the structure of nanoparticles at the interface, the barrier properties of the assembly and the rate of particle attachment and exchange, all of which are essential to the use of these assemblies for the design and fabrication of novel materials and devices. More specifically, the work presented in this thesis supports the following conclusions:

- An equation relating thermodynamic quantities originally presented by Du *et al.* [26] is generalized and interpreted as a statement between DST and transient interface coverage. The result, Eq. (3.9), is a hitherto unknown connection between a readily measured macroscopic quantity (the DST) and a difficult to assess measure of adsorption-mediated nanoparticle self-assembly (interface coverage).
- When the energy released following the adsorption of nanoparticles is significantly larger than the mean energy of thermal fluctuations, adsorption is irreversible and

models suitable for the interpretation of DST data of surfactant solutions break down completely.

- The generalized RSA theory [67, 5] provides a sound basis on which to interpret irreversible adsorption of nanoparticles on fluid interfaces. Using Eq. (3.9), the generalized RSA theory is successfully applied to EC nanoparticle adsorption at the air-water interface for the first time.
- Contrary to claims by Jin *et al.* [41], adsorption of EC nanoparticles at the air-water interface takes place spontaneously and irreversibly at neutral pH. There appears to be no significant barrier to adsorption originating from DLVO particle-interface interactions.
- Coverage of the air-water interface by EC nanoparticles of either 89.1 nm or 42 nm reaches a maximum (jamming) coverage of 0.91, in agreement with the results of recent atomistic simulations by Isa *et al.* [38]. Novel estimates of the adsorption energy of both nanoparticles are in excellent agreement with literature results.

7.2 Recommendations

- As reported in [41] and verified by preliminary experiments in our laboratory, solution pH and ionic strength are important parameters controlling the stability of colloidal solutions of EC nanoparticles. By decreasing pH or increasing salinity, the magnitude of surface charge on the EC nanoparticles decreases causing the nanoparticles to settle (flocculate). In real applications of such nanoparticles, pH and salt concentration may vary. Therefore, investigation of the surface activity of EC nanoparticles at different pH and salt concentrations should be explored to establish the limits of applicability of these particles.
- Preliminary experiments in our laboratory showed that EC nanoparticles can effectively stabilize Pickering emulsions. Water-in-oil (W/O) emulsions using silicon oil, dodecane, tetradecane, FC-40, and FC-70 were all successfully stabilized by EC nanoparticles, but water-in-hexane emulsions were not. Characterization of such emulsions and investigation of the attachment of EC nanoparticles at oil-water interfaces should be pursued.
- The proposed model has been tested with two sizes of EC nanoparticles. Although the sizes of these nanoparticles were quite different, further validation using smaller nanoparticles near the limit of adsorption reversibility is desirable.

- A theoretical investigation based on extended DLVO calculations is also recommended to examine the strength of electrostatic repulsion between EC nanoparticles and the air-water interface and assess the possible role of hydrophobic forces.

APPENDICES

Appendix A

Batch Distillation Calculations

The last step in the synthesis of EC nanoparticles is boiling off the isopropyl alcohol (see Figure 4.1). This process is in fact a batch distillation of isopropyl alcohol-water mixture under atmospheric pressure. Knowing the vapor-liquid equilibria for alcohol-water mixture, the amount of alcohol remaining in the solution can be calculated from Rayleigh method for batch distillation processes [49]. Accordingly, the amount of isopropyl alcohol remaining in the solution can be calculated from [49]:

$$\int_{x_W}^z \frac{dx}{y-x} = \ln\left(\frac{F}{W}\right) \quad (\text{A.1})$$

where x and y are the mole fraction of alcohol in the liquid and in the vapor phase, respectively, at equilibrium conditions, and z and x_W denote the mole fraction of alcohol in the liquid phase before and after distillation, respectively. F and W are the amount of liquid phase, in terms of moles, before and after distillation, respectively. The left-hand side of Eq. (A.1) can be calculated from the area under the curve of $1/(y-x)$ plotted against x . However, the lower limit (i.e., x_W) is unknown. Calculating x_W , which represents the amount of alcohol remaining in the final solution, is the goal of this appendix.

The procedure shown in Figure A.1 is followed. Guessing a value for F/W would lead us to calculate the amount of W from two approaches: I. directly from F/W ratio knowing the quantity of F , and II. from mass balance for the final solution knowing x_W from Eq. (A.1) and the mass of final solution. The details of each approach are presented below.

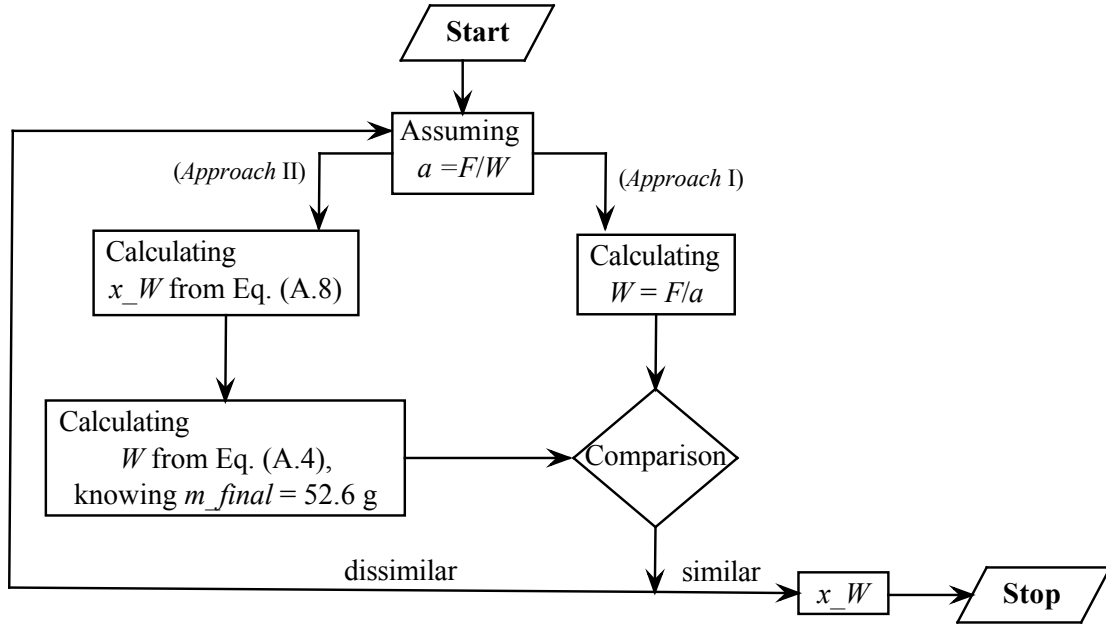


Figure A.1: A trial-and-error procedure for calculating the amount of alcohol remaining in the final solution.

Approach I:

The amount of liquid phase before distillation can be found from:

$$F = f_w + f_a \quad (\text{A.2})$$

where subscripts w and a denote *water* and *alcohol*, respectively. Knowing the volume of each component (i.e., 75 mL), Eq. (A.2) is written as:

$$F = \frac{\rho_w V_w}{(MW)_w} + \frac{\rho_a V_a}{(MW)_a} \quad (\text{A.3})$$

Substituting $\rho_w = 998.2$ g/L, $\rho_a = 786$ g/L (valid at 20°C), $(MW)_w = 18.01$ g/mol, and $(MW)_a = 60.1$ g/mol into Eq. (A.3) gives us $F = 5.137$ moles. Therefore, the amount of W can be easily found from the guessed value of F/W .

Approach II:

A mass balance for alcohol in the final solution can be written as:

$$\begin{aligned} m_{final} &= x_W (MW)_a W + (1 - x_W) (MW)_w W \\ \Rightarrow W &= \frac{m_{final}}{x_W (MW)_a + (1 - x_W) (MW)_w} \end{aligned} \quad (\text{A.4})$$

The values of molecular weight of water and alcohol are known and the amount of m_{final} is measured after the evaporation process is done (i.e., 52.6 g). The unknown parameter is x_W . Eq. (A.1) is employed to obtain the mole fraction of alcohol in the final solution (x_W).

To do so, first of all, the mole fraction of alcohol in the solution before distillation can be calculated from:

$$z = \frac{f_a}{F} = \frac{\rho_a V_a}{(MW)_a F} = \frac{786 \times 75 \times 10^{-3}}{60.1 \times 5.137} \Rightarrow z = 0.191 \quad (\text{A.5})$$

As mentioned earlier, the left-hand side of Eq. (A.1) can be calculated from the area under the curve of $1/(y-x)$ plotted against x . The vapor-liquid equilibria for isopropyl alcohol-water mixtures is found from [20] and $1/(y-x)$ data are plotted against x in Figure A.2 for the range of interest (i.e., mole fraction of alcohol < 0.2 , because $z=0.191$). A power equation is fitted to the data with an $R^2 = 0.9982$, expressed below:

$$Y = \frac{1}{y-x} = 0.02725x^{-1.069} + 2.199 \quad (\text{A.6})$$

Integrating Eq. (A.6) results in:

$$\int_{x_W}^z \frac{dx}{y-x} = -0.3949x^{-0.069} + 2.199x \Big|_{x_W}^{0.191} \quad (\text{A.7})$$

Substituting Eq. (A.7) into Eq. (A.1) results in

$$-0.0227 - \left(-0.3949x_W^{-0.069} + 2.199x_W \right) = \ln\left(\frac{F}{W}\right) \quad (\text{A.8})$$

Thus, x_W can be calculated from Eq. (A.8) at a guessed value for F/W .

Following the procedure shown in Figure A.1 results in:

$$\begin{aligned} x_W &= 0.29 \text{ \%mole} \\ \frac{F}{W} &= 1.754 \\ W_{\text{approach I}} &= 2.93 \\ W_{\text{approach II}} &= 2.90 \\ \%error &= \pm 0.9\% \end{aligned} \quad (\text{A.9})$$

The amount of alcohol (x_W) remaining in the final aqueous solution of EC nanoparticles (after the distillation) is thus found to be ~ 0.3 %mole.

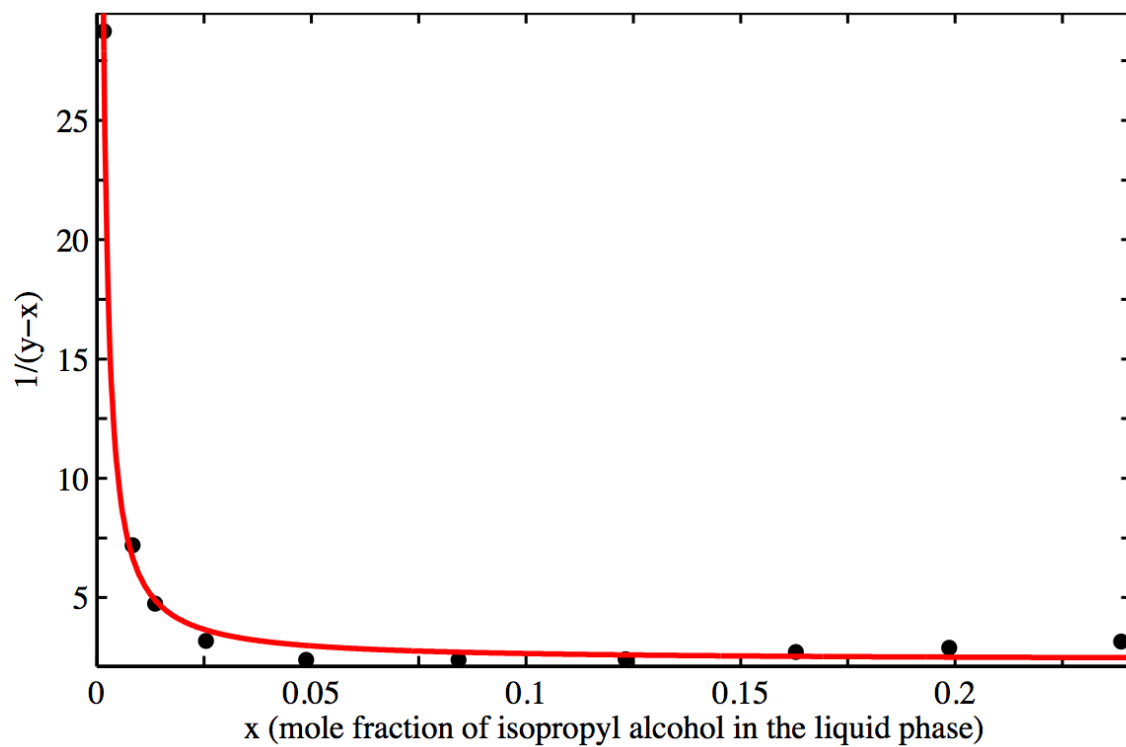


Figure A.2: The vapour-liquid equilibria for a binary mixture of isopropyl alcohol-water plotted in terms of $1/(y - x)$ against the mole fraction of alcohol in the liquid phase.

Appendix B

Late Time and Early Time DST Data Analysis

The late and early time DST data of large (89.1 nm) and small (42 nm) EC nanoparticles are analyzed employing Eq. (3.8) and Eq. (3.10), respectively. The results of these analyses and the fitted lines are shown in Figure B.1 and Figure B.2 for long and early time DST data of large EC nanoparticles, respectively, and in Figure B.3 and Figure B.4 for long and early time DST data of small EC nanoparticles.

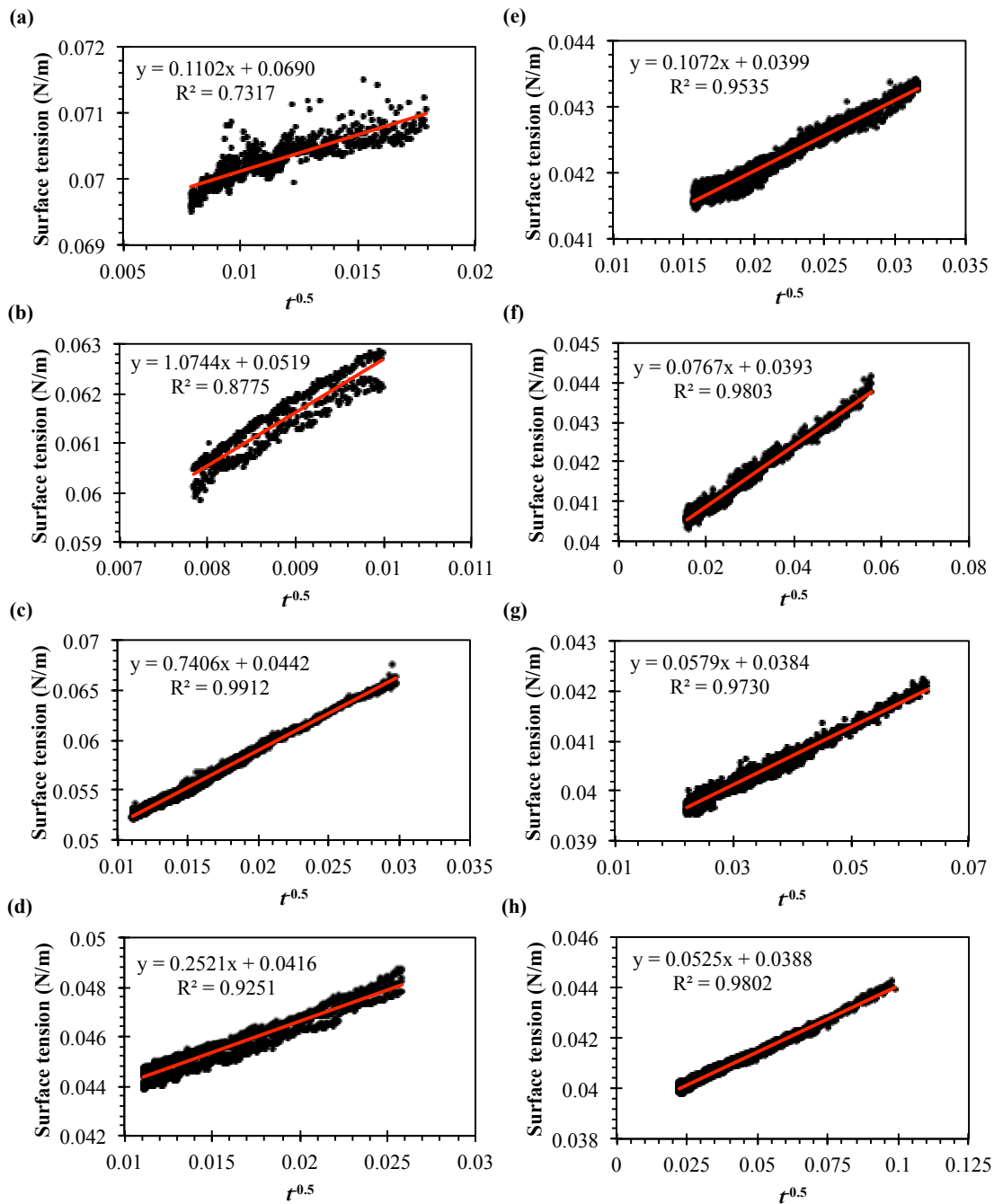


Figure B.1: Fitting Eq. (3.8) on the long time DST data of 89.1 nm EC nanoparticles at (a) 0.05 g/L, (b) 0.075 g/L, (c) 0.1 g/L, (d) 0.2 g/L, (e) 0.4 g/L, (f) 0.6 g/L, (g) 0.8 g/L, and (h) 1.0 g/L bulk concentrations of EC nanoparticles.

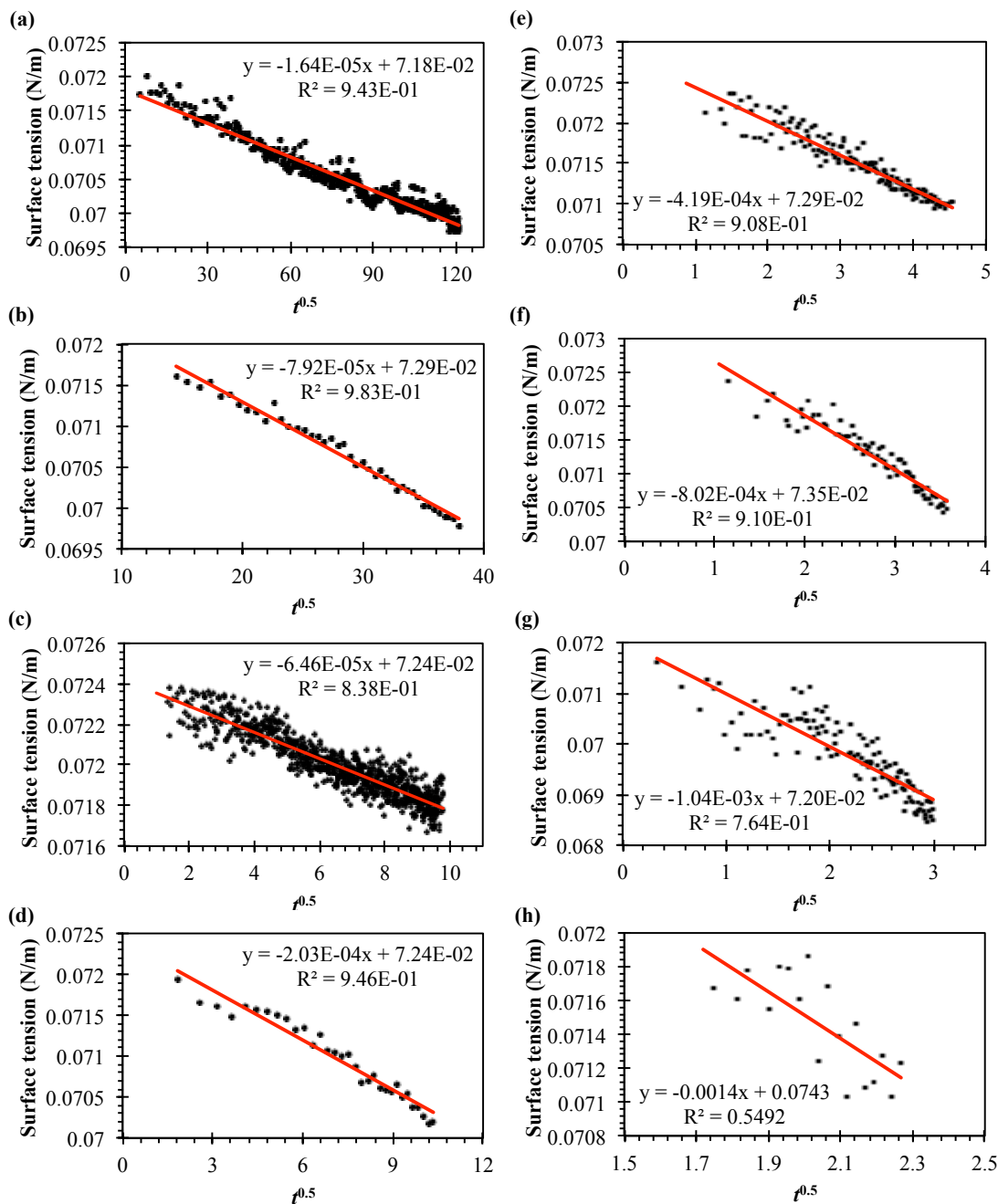


Figure B.2: Fitting Eq. (3.10) on the early time DST data of 89.1 nm EC nanoparticles at (a) 0.05 g/L, (b) 0.075 g/L, (c) 0.1 g/L, (d) 0.2 g/L, (e) 0.4 g/L, (f) 0.6 g/L, (g) 0.8 g/L, and (h) 1.0 g/L bulk concentrations of EC nanoparticles.

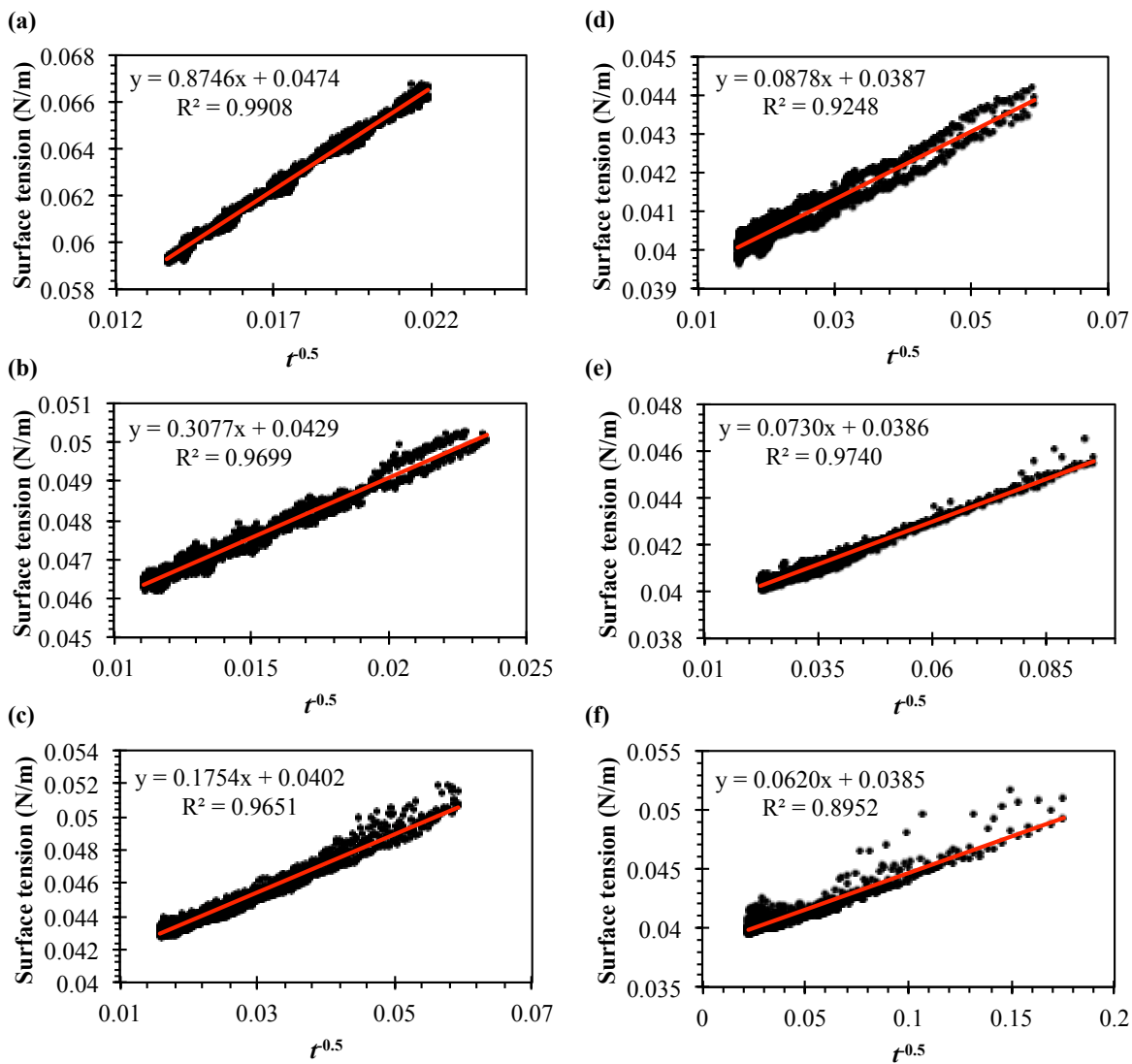


Figure B.3: Fitting Eq. (3.8) on the long time DST data of 42 nm EC nanoparticles at (a) 0.1 g/L, (b) 0.2 g/L, (c) 0.4 g/L, (d) 0.6 g/L, (e) 0.8 g/L, and (f) 1.0 g/L bulk concentrations of EC nanoparticles.

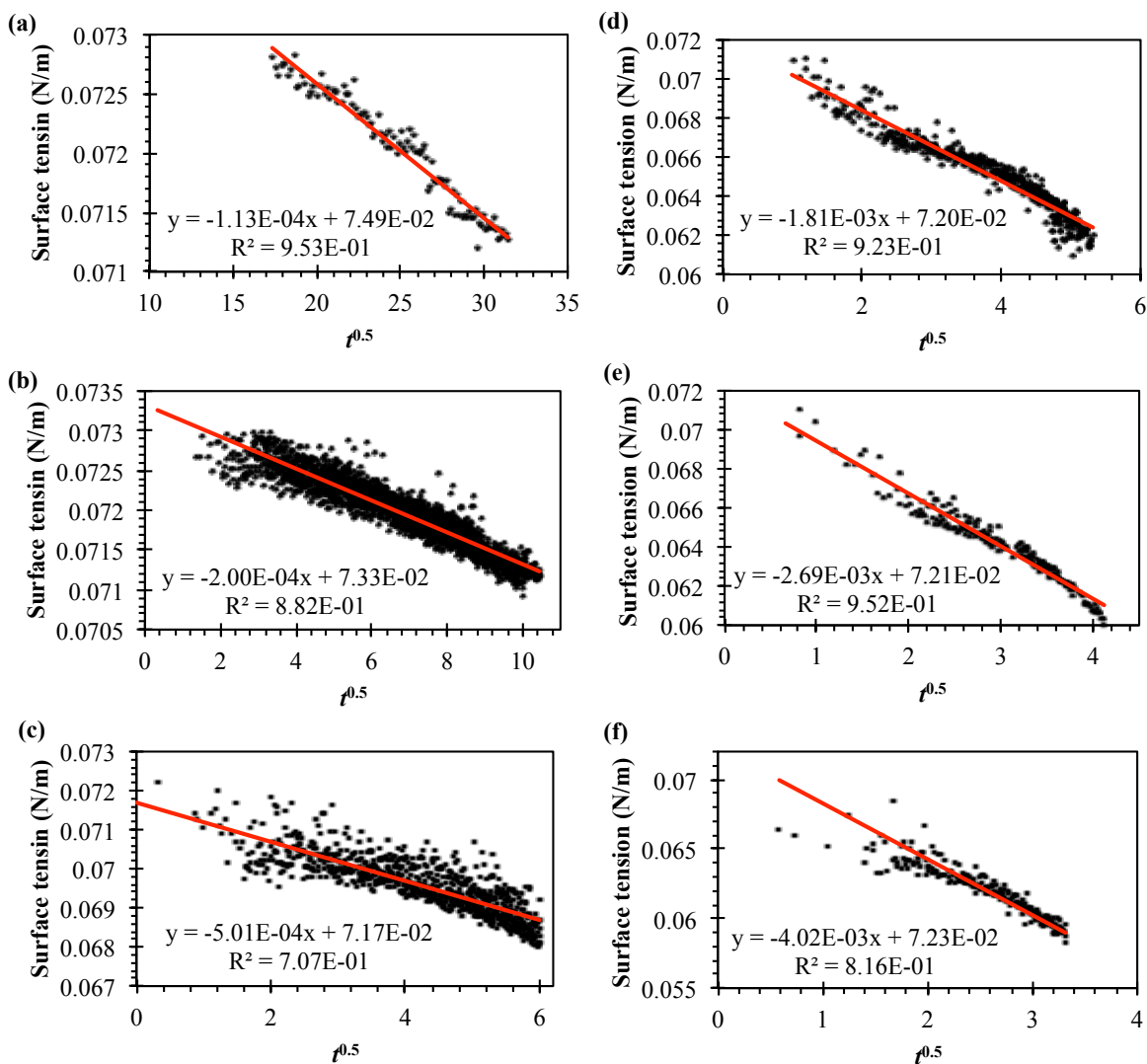


Figure B.4: Fitting Eq. (3.10) on the early time DST data of 42 nm EC nanoparticles at (a) 0.1 g/L, (b) 0.2 g/L, (c) 0.4 g/L, (d) 0.6 g/L, (e) 0.8 g/L, and (f) 1.0 g/L bulk concentrations of EC nanoparticles.

Appendix C

Calculating θ_{\max} and K_l

Considering the definition of t_c (i.e., $1/(\pi r^2 C_0)^2 D$), Eq. (2.52) can be written as

$$\theta = \theta_{\max} - K_l \left(\frac{t}{t_c} \right)^{-0.5} \quad (\text{C.1})$$

Therefore, θ_{\max} and K_l can be found from the intercept and the slope of the lines fitted to the surface coverage data plotted against $(t/t_c)^{-0.5}$. The fitted lines at different concentrations are shown in Figure C.1 and Figure C.2 for large (89.1 nm) and small (42 nm) EC nanoparticles, respectively. The plots are sketched for concentrations greater than 0.1 g/L which “real” long-time data have been measured. The values of θ_{\max} and K_l , obtained from this analysis, are reported in Table C.1 for both of larger and small EC nanoparticles.

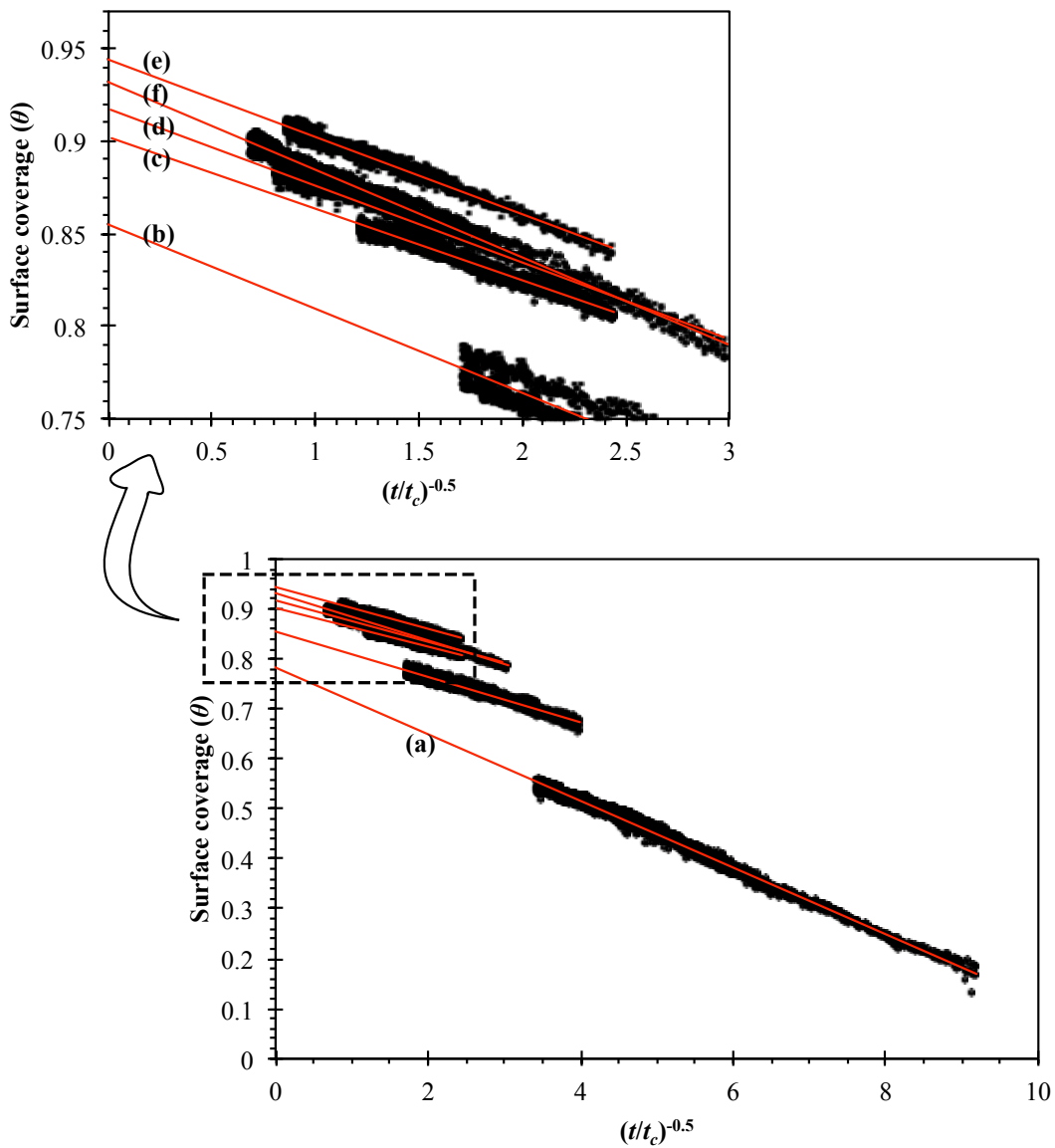


Figure C.1: Fitting Eq. (C.1) to the experimental data of 89.1 nm EC nanoparticle surface coverage at different bulk concentrations: (a) 0.1 g/L, (b) 0.2 g/L, (c) 0.4 g/L, (d) 0.6 g/L, (e) 0.8 g/L, and (f) 1.0 g/L.

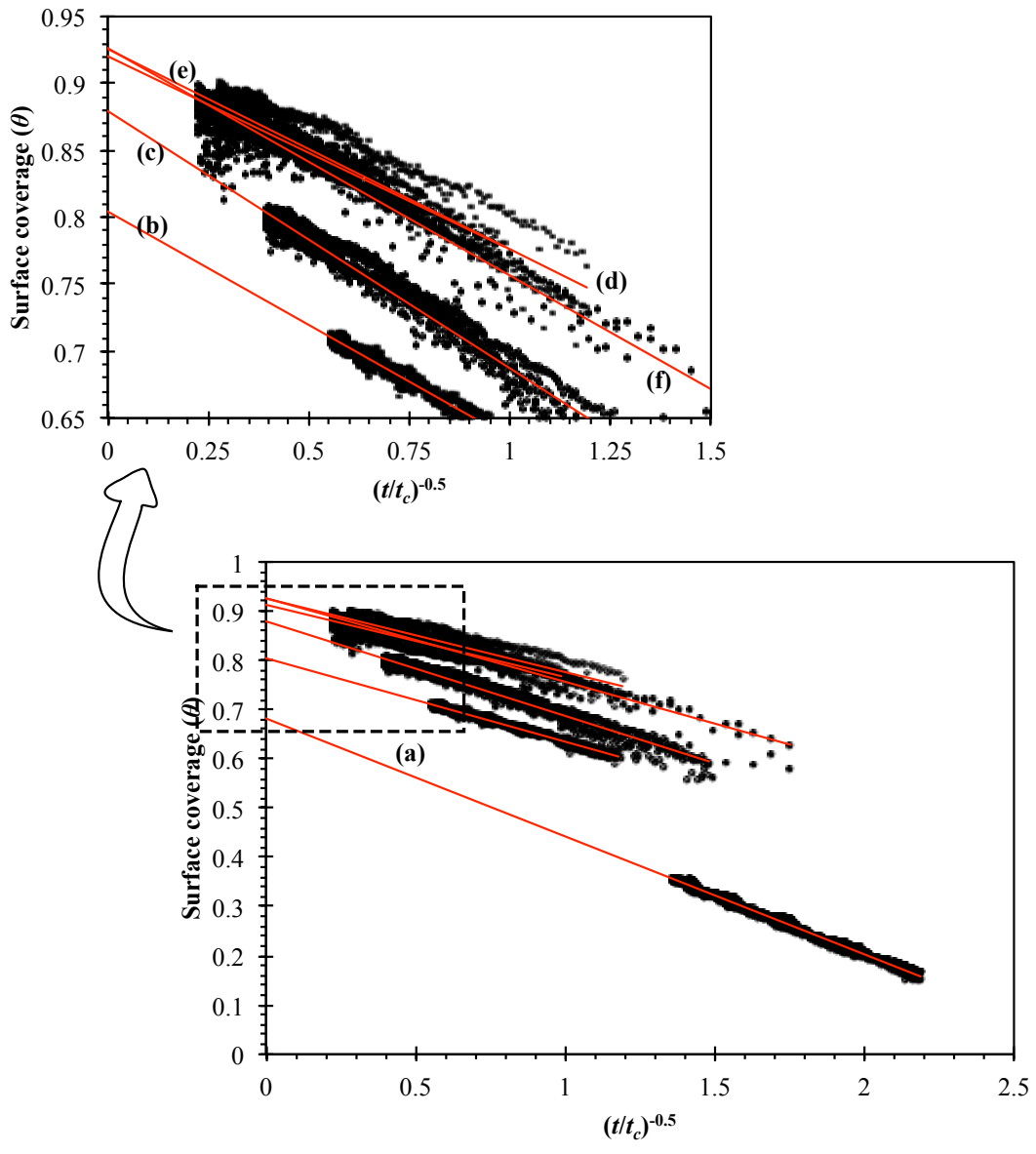


Figure C.2: Fitting Eq. (C.1) to the experimental data of 42 nm EC nanoparticle surface coverage at different bulk concentrations: (a) 0.1 g/L, (b) 0.2 g/L, (c) 0.4 g/L, (d) 0.6 g/L, (e) 0.8 g/L, and (f) 1.0 g/L.

Table C.1: The values of the intercept (θ_{\max}) and the slope (K_l) of fitted lines shown in Figure C.1 and Figure C.2 for large and small EC nanoparticles, respectively.

C (g/L)	89.1 nm EC nanoparticles			42 nm EC nanoparticles		
	θ_{\max}	K_l	R^2	θ_{\max}	K_l	R^2
0.1	0.7827	0.0667	0.991	0.6745	0.2395	0.991
0.2	0.8549	0.0454	0.925	0.7954	0.1694	0.971
0.4	0.9021	0.0386	0.954	0.8697	0.1922	0.965
0.6	0.9173	0.0415	0.980	0.9155	0.1479	0.924
0.8	0.9439	0.0417	0.973	0.9101	0.1427	0.824
1.0	0.9318	0.0473	0.980	0.9161	0.1698	0.895
Ave.:	0.924 ± 0.02	0.042 ± 0.004	-	0.914 ± 0.003	0.153 ± 0.014	-

Appendix D

The Minimum Concentration for Full Coverage

The minimum “theoretical” bulk concentration required for full coverage of the interface is calculated as follows:

Starting from Eq. (6.2), the surface concentration is calculated:

$$\Gamma_{eq} = \frac{\theta_{\max}}{N_A \pi r^2} \quad (6.2)$$

where $\theta_{\max} \cong 0.91$, N_A is Avogadro’s number, and r is the particle radius. Using Eq. (6.2), Γ_{eq} is calculated in terms of mol/m². Multiplying Γ_{eq} by the pendant droplet surface area, $S_{droplet}$, the minimum moles of particles required for full interfacial coverage is obtained. Accordingly,

$$N_{\min} = \Gamma_{eq} \times S_{droplet} \quad (D.1)$$

The minimum bulk concentration required for full coverage of the interface can be obtained from:

$$C_{\min} = \frac{N_{\min}}{V_{droplet}} \quad (D.2)$$

Assuming a spherical shape for the pendant droplet, and substituting Eq. (6.2) and Eq. (D.1) into Eq. (D.2), one would get:

$$C_{\min} = \frac{\theta_{\max}}{N_A \pi r^2} \frac{4\pi R^2}{\frac{4}{3}\pi R^3} \Rightarrow C_{\min} = \frac{3\theta_{\max}}{N_A \pi r^2 R} \quad (D.3)$$

where R is the pendant droplet radius. Considering the typical value for the droplet volume (i.e., $\sim 10\mu\text{L}$), preset by the syringe controller of the pendant drop tensiometer (see Figure 4.2), a radius of 1.34×10^{-3} m is calculated for the pendant droplet. In order to express the minimum concentration in terms of g/L, Eq. (4.1) has been rearranged to solve for ρ as follows:

$$\rho_{\min} = \frac{4}{3}\pi r^3 \rho_p N_A C_{\min} \quad (4.1)$$

where the particle density, ρ_p , is 1140 g/L. Substituting this equation into Eq. (D.3), one gets:

$$\begin{aligned} \rho_{\min} &= \left(\frac{4}{3}\pi r^3 \rho_p N_A \right) \frac{3\theta_{\max}}{N_A \pi r^2 R} \\ \Rightarrow \rho_{\min} &= \frac{4\rho_p r \theta_{\max}}{R} \end{aligned} \quad (D.4)$$

Therefore, the minimum bulk concentration required for full coverage of the interface for large ($d=89.1$ nm) and small ($d=42$ nm) EC nanoparticles are calculated as:

Large EC nanoparticle:

$$\begin{aligned} \rho_{\min} &= \frac{4 \times 1140 \times 44.55 \times 10^{-9} \times 0.91}{1.34 \times 10^{-3}} \\ \Rightarrow \rho_{\min} &= 0.14 \frac{\text{g}}{\text{L}} \end{aligned} \quad (D.5)$$

Small EC nanoparticle:

$$\begin{aligned} \rho_{\min} &= \frac{4 \times 1140 \times 21 \times 10^{-9} \times 0.91}{1.34 \times 10^{-3}} \\ \Rightarrow \rho_{\min} &= 0.07 \frac{\text{g}}{\text{L}} \end{aligned} \quad (D.6)$$

References

- [1] Z. Adamczyk. Kinetics of diffusion-controlled adsorption of colloid particles and proteins. *Journal of Colloid and Interface Science*, 229(2):477 – 489, 2000.
- [2] Z. Adamczyk, K. Jaszczólt, A. Michna, B. Siwek, L. Szyk-Warszyńska, and M. Zembala. Irreversible adsorption of particles on heterogeneous surfaces. *Advances in Colloid and Interface Science*, 118:25 – 42, 2005.
- [3] Z. Adamczyk, K. Jaszczólt, B. Siwek, and P. Weroński. Irreversible adsorption of particles at random-site surfaces. *The Journal of Chemical Physics*, 120(23):11155–11162, 2004.
- [4] Z. Adamczyk, M. Nattich, and J. Barbasz. Deposition of colloid particles at heterogeneous and patterned surfaces. *Advances in Colloid and Interface Science*, 147-148:2 – 17, 2009.
- [5] Z. Adamczyk, B. Siwek, M. Zembala, and P. Belouschek. Kinetics of localized adsorption of colloid particles. *Advances in Colloid and Interface Science*, 48(0):151 – 280, 1994.
- [6] Z. Adamczyk and L. Szyk. Kinetics of irreversible adsorption of latex particles under diffusion-controlled transport. *Langmuir*, 16(13):5730–5737, 2000.
- [7] Z. Adamczyk and P. Weroński. Application of the dlvo theory for particle deposition problems. *Advances in Colloid and Interface Science*, 83:137 – 226, 1999.
- [8] Z. Adamczyk, P. Weroński, and E. Musiał. Particle adsorption under irreversible conditions: kinetics and jamming coverage. *Colloids and Surfaces A: Physicochemical and Engineering Aspects*, 208:29 – 40, 2002.
- [9] A. W. Adamson and A. P. Gast. *Physical chemistry of surfaces*. John Wiley & Sons, Inc., New York, NY, 1997.

- [10] M. A. Ahmadi and S. R. Shadizadeh. Adsorption of novel nonionic surfactant and particles mixture in carbonates: Enhanced oil recovery implication. *Energy & Fuels*, 26(8):4655–4663, 2012.
- [11] R. Aveyard, B. P. Binks, and J. H. Clint. Emulsions stabilised solely by colloidal particles. *Advances in Colloid and Interface Science*, 100-102(0):503 – 546, 2003.
- [12] S. Azizian, H. Motani, K. Shibata, T. Matsuda, T. Takiue, H. Matsubara, and M. Aratono. Analysis of dynamic surface tension of tetraethyleneglycol monoethyl ether at air/water interface. *Colloid and Polymer Science*, 285:1699–1705, 2007.
- [13] J. F. Baret. Theoretical model for an interface allowing a kinetic study of adsorption. *Journal of Colloid and Interface Science*, 30(1):1 – 12, 1969.
- [14] B. P. Binks. Particles as surfactants - similarities and differences. *Current Opinion in Colloid & Interface Science*, 7:21 – 41, 2002.
- [15] B. P. Binks, B. Duncumb, and R. Murakami. Effect of pH and salt concentration on the phase inversion of particle-stabilized foams. *Langmuir*, 23(18):9143–9146, 2007.
- [16] B. P. Binks and S. O. Lumsdon. Influence of particle wettability on the type and stability of surfactant-free emulsions. *Langmuir*, 16(23):8622–8631, 2000.
- [17] K. S. Bird, editor. *Handbook of Surface and Colloid Chemistry*. CRC Press, Boca Raton, FL, 2008.
- [18] R. B. Bird, W. E. Stewart, and E. N. Lightfoot. *Transport Phenomena*. John Wiley & Sons, Inc., New York, NY, 1960.
- [19] A. Böker, J. He, T. Emrick, and T. P. Russell. Self-assembly of nanoparticles at interfaces. *Soft Matter*, 3:1231–1248, 2007.
- [20] A. S. Brunjes and M. J. P. Bogart. Vapor-liquid equilibria for commercially important systems of organic solvents: The binary systems ethanol-n-butanol, acetone-water and isopropanol-water. *Industrial & Engineering Chemistry*, 35(2):255–260, 1943.
- [21] E. Calvo, R. Bravo, A. Amigo, and J. Gracia-Fadrique. Dynamic surface tension, critical micelle concentration, and activity coefficients of aqueous solutions of nonyl phenol ethoxylates. *Fluid Phase Equilibria*, 282(1):14 – 19, 2009.

- [22] A. Cervantes Martinez, E. Rio, G. Delon, A. Saint-Jalmes, D. Langevin, and B. P. Binks. On the origin of the remarkable stability of aqueous foams stabilised by nanoparticles: link with microscopic surface properties. *Soft Matter*, 4:1531–1535, 2008.
- [23] J. Chai, X. Yang, Y. Gao, J. Chen, and Zh. Wang. Adsorption equilibrium and kinetics on *N*-lauroyl-*N*-methylglucamide at air/water interface. *Colloid Journal*, 70:221–226, 2008.
- [24] P. Chaverot, A. Cagna, S. Glita, and F. Rondelez. Interfacial tension of bitumenwater interfaces. part 1: Influence of endogenous surfactants at acidic ph. *Energy & Fuels*, 22(2):790–798, 2008.
- [25] R. Defay, I. Prigogine, and A. Bellemans. *Surface tension and adsorption*. Longmans, London, 1966.
- [26] K. Du, E. Glogowski, T. Emrick, T. P. Russell, and A. D. Dinsmore. Adsorption energy of nano- and microparticles at liquidliquid interfaces. *Langmuir*, 26(15):12518–12522, 2010.
- [27] K. Du, J. A. Liddle, and A. J. Berglund. Three-dimensional real-time tracking of nanoparticles at an oilwater interface. *Langmuir*, 28(25):9181–9188, 2012.
- [28] J. Eastoe and J. S. Dalton. Dynamic surface tension and adsorption mechanisms of surfactants at the air-water interface. *Advances in Colloid and Interface Science*, 85:103 – 144, 2000.
- [29] D. F. Evans and H. Wennerström. *The colloidal domain: where physics, chemistry, biology, and technology meet*. Wiley-VCH, New York, NY, 1999.
- [30] V. B. Fainerman, A. V. Makievski, and R. Miller. The analysis of dynamic surface tension of sodium alkyl sulphate solutions, based on asymptotic equations of adsorption kinetic theory. *Colloids and Surfaces A: Physicochemical and Engineering Aspects*, 87(1):61 – 75, 1994.
- [31] S. Ferdous, M. A. Ioannidis, and D. Henneke. Adsorption kinetics of alkanethiol-capped gold nanoparticles at the hexanewater interface. *Journal of Nanoparticle Research*, 13:6579–6589, 2011.
- [32] V. Garbin, J. C. Crocker, and K. J. Stebe. Nanoparticles at fluid interfaces: Exploiting capping ligands to control adsorption, stability and dynamics. *Journal of Colloid and Interface Science*, 387(1):1 – 11, 2012.

- [33] H. Ghojavand, F. Vahabzadeh, and A. Khodabandeh Shahraki. Enhanced oil recovery from low permeability dolomite cores using biosurfactant produced by a bacillus mojavensis (ptcc 1696) isolated from masjed-i soleyman field. *Journal of Petroleum Science and Engineering*, 81:24 – 30, 2012.
- [34] F. Giusti, J. L. Popot, and C. Tribet. Well-defined critical association concentration and rapid adsorption at the air/water interface of a short amphiphilic polymer, amphipol a8-35: A study by frster resonance energy transfer and dynamic surface tension measurements. *Langmuir*, 28(28):10372–10380, 2012.
- [35] U. T. Gonzenbach, A. R. Studart, E. Tervoort, and L. J. Gauckler. Ultrastable particle-stabilized foams. *Angewandte Chemie International Edition*, 45(21):3526–3530, 2006.
- [36] X. Y. Hua and M. J. Rosen. Dynamic surface tension of aqueous surfactant solutions: I. basic parameters. *Journal of Colloid and Interface Science*, 124(2):652 – 659, 1988.
- [37] S. Iglauer, Y. Wu, P. Shuler, Y. Tang, and W. A. Goddard III. New surfactant classes for enhanced oil recovery and their tertiary oil recovery potential. *Journal of Petroleum Science and Engineering*, 71:23 – 29, 2010.
- [38] L. Isa, E. Amstad, K. Schwenke, E. Del Gado, P. Ilg, M. Kroger, and E. Reimhult. Adsorption of core-shell nanoparticles at liquid-liquid interfaces. *Soft Matter*, 7:7663–7675, 2011.
- [39] J. Israelachvili and R. Pashley. The hydrophobic interaction is long range, decaying exponentially with distance. *Nature*, 300(5890):341–342, 1982.
- [40] J. N. Israelachvili. *Intermolecular and surface forces*. American Press Inc., San Diego, CA, 1992.
- [41] H. Jin, W. Zhou, J. Cao, S. D. Stoyanov, T. B. J. Blijdenstein, P. W. N. de Groot, L. N. Arnaudov, and E. G. Pelan. Super stable foams stabilized by colloidal ethyl cellulose particles. *Soft Matter*, 8:2194–2205, 2012.
- [42] M. Joshi, B. Adhikari, P. Aldred, J. F. Panozzo, S. Kasapis, and C. J. Barrow. Interfacial and emulsifying properties of lentil protein isolate. *Food Chemistry*, 134(3):1343 – 1353, 2012.
- [43] R. S. Krishnan, M. E. Mackay, P. M. Duxbury, C. J. Hawker, S. Asokan, M. S. Wong, R. Goyette, and P. Thiyagarajan. Improved polymer thin-film wetting behavior

- through nanoparticle segregation to interfaces. *Journal of Physics: Condensed Matter*, 19(35):356003, 2007.
- [44] S. Kutuzov, J. He, R. Tangirala, T. Emrick, T. P. Russell, and A. Böker. On the kinetics of nanoparticle self-assembly at liquid/liquid interfaces. *Physical Chemistry Chemical Physics*, 9:6351–6358, 2007.
- [45] X. Li, R. Shaw, G. M. Evans, and P. Stevenson. A simple numerical solution to the ward-tordai equation for the adsorption of non-ionic surfactants. *Computers & Chemical Engineering*, 34(2):146 – 153, 2010.
- [46] L. Liggieri, F. Ravera, and A. Passerone. A diffusion-based approach to mixed adsorption kinetics. *Colloids and Surfaces A: Physicochemical and Engineering Aspects*, 114:351 – 359, 1996.
- [47] Y. Lin, A. Böker, H. Skaff, D. Cookson, A. D. Dinsmore, T. Emrick, and T. P. Russell. Nanoparticle assembly at fluid interfaces: structure and dynamics. *Langmuir*, 21(1):191–194, 2005.
- [48] Y. Lin, H. Skaff, T. Emrick, A. D. Dinsmore, and T. P. Russell. Nanoparticle assembly and transport at liquid-liquid interfaces. *Science*, 299(5604):226–229, 2003.
- [49] W. L. McCabe, J. C. Smith, and P. Harriott. *Unit operations of chemical engineering*. McGraw-Hill, Inc., USA, 1993.
- [50] K. J. Mysels. *Introduction to colloid chemistry*. Interscience Publishers, New York, NY, 1959.
- [51] Y. K. Park, S. H. Yoo, and S. Park. Assembly of highly ordered nanoparticle monolayers at a water/hexane interface. *Langmuir*, 23(21):10505–10510, 2007.
- [52] X. Pei, Y. You, J. Zhao, Y. Deng, E. Li, and Z. Li. Adsorption and aggregation of 2-hydroxyl-propanediyl-,bis(dimethyldodecyl ammonium bromide) in aqueous solution: Effect of intermolecular hydrogen-bonding. *Journal of Colloid and Interface Science*, 351(2):457 – 465, 2010.
- [53] S. U. Pickering. Cxcvi.-emulsions. *Journal of the Chemical Society, Transactions*, 91:2001–2021, 1907.
- [54] P. Pieranski. Two-dimensional interfacial colloidal crystals. *Physical Review Letters*, 45:569–572, 1980.

- [55] S. Podzimek. *Light scattering, size exclusion chromatography, and asymmetric flow field flow fractionation: powerful tools for the characterization of polymers, proteins and nanoparticles*. John Wiley & Sons, Inc., Hoboken, NJ, 2011.
- [56] V. Pradines, J. Krägel, V. B. Fainerman, and R. Miller. Interfacial properties of mixed γ -lactoglobulins layers at the water/air and water/oil interface. *The Journal of Physical Chemistry B*, 113(3):745–751, 2009.
- [57] F. Ravera, E. Santini, G. Loglio, M. Ferrari, and L. Liggieri. Effect of nanoparticles on the interfacial properties of liquid/liquid and liquid/air surface layers. *The Journal of Physical Chemistry B*, 110(39):19543–19551, 2006.
- [58] Y. V. Rojas, C. M. Phan, and X. Lou. Dynamic surface tension studies on poly(*n*-vinylcaprolactam/*n*-vinylpyrrolidone/*n,n*-dimethylaminoethyl methacrylate) at the air/liquid interface. *Colloids and Surfaces A: Physicochemical and Engineering Aspects*, 355:99 – 103, 2010.
- [59] S. Ross and I. D. Morrison. *Colloidal systems and interfaces*. Wiley-Interscience publication, New York, Toronto, 1988.
- [60] S. Rudiuk, L. Cohen-Tannoudji, S. Huille, and C. Tribet. Importance of the dynamics of adsorption and of a transient interfacial stress on the formation of aggregates of IgG antibodies. *Soft Matter*, 8:2651–2661, 2012.
- [61] J. E. Shaw. Enhanced oil recovery using carboxylate surfactant systems. *Journal of the American Oil Chemists Society*, 61:1389–1394, 1984.
- [62] A. Stocco, W. Drenckhan, E. Rio, D. Langevin, and B. P. Binks. Particle-stabilised foams: an interfacial study. *Soft Matter*, 5:2215–2222, 2009.
- [63] R. J. Stokes and D. F. Evans. *Fundamentals of interfacial engineering*. Wiley-VCH Inc., New York, NY, 1997.
- [64] B. A. Suleimanov, F. S. Ismailov, and E. F. Veliyev. Nanofluid for enhanced oil recovery. *Journal of Petroleum Science and Engineering*, 78(2):431 – 437, 2011.
- [65] J. Sung, K. Park, and D. Kim. Surfaces of alcohol/water mixtures studied by sum-frequency generation vibrational spectroscopy. *The Journal of Physical Chemistry B*, 109(39):18507–18514, 2005.

- [66] Y. Takamatsu, N. Iwata, K. Tsubone, K. Torigoe, T. Endo, K. Sakai, H. Sakai, and M. Abe. Synthesis and aqueous solution properties of novel anionic heterogemini surfactants containing a phosphate headgroup. *Journal of Colloid and Interface Science*, 338(1):229 – 235, 2009.
- [67] J. Tóth, editor. *Adsorption: Theory, Modeling, and Analysis*. Marcel Dekker, 2002.
- [68] V. A. Turek, M. P. Cecchini, J. Paget, A. R. Kucernak, A. A. Kornyshev, and J. B. Edel. Plasmonic ruler at the liquidliquid interface. *ACS Nano*, 6(9):7789–7799, 2012.
- [69] S. Wang and J. Ma. Surface property of nonionic surfactant triton x-100 in an ionic liquid. *Journal of Dispersion Science and Technology*, 30(9):1395–1398, 2009.
- [70] A. F. H. Ward and L. Tordai. Time-dependence of boundary tensions of solutions i. the role of diffusion in time-effects. *The Journal of Chemical Physics*, 14(7):453–461, 1946.
- [71] H. S. Wi, S. Cingarapu, K. J. Klabunde, and B. M. Law. Nanoparticle adsorption at liquid-vapor surfaces: Influence of nanoparticle thermodynamics, wettability, and line tension. *Langmuir*, 27(16):9979–9984, 2011.
- [72] K. Wojciechowski and A. Brzozowska. From gibbs- to langmuir-type adsorbed layers: Alkylated azacrown ethers at liquidliquid interfaces. *The Journal of Physical Chemistry C*, 116(23):12584–12590, 2012.
- [73] K. Wojciechowski, M. Piotrowski, W. Popielarz, and T. R. Sosnowski. Short- and mid-term adsorption behaviour of quillaja bark saponin and its mixtures with lysozyme. *Food Hydrocolloids*, 25(4):687 – 693, 2011.
- [74] C. Yang and Y. Gu. Modeling of the adsorption kinetics of surfactants at the liquidfluid interface of a pendant drop. *Langmuir*, 20(6):2503–2511, 2004.
- [75] R. Zana, editor. *Dynamics of surfactant self-assemblies : micelles, microemulsions, vesicles, and lyotropic phases*. Taylor & Francis, 2005.
- [76] N. Zhihong, A. Petukhova, and E. Kumacheva. Properties and emerging applications of self-assembled structures made from inorganic nanoparticles. *Nature Nanotechnology*, 5:15–25, 2010.